In-situ investigation of the flux shadowing effect on polytypism and strain evolution in self-catalyzed core and core-shell nanowire systems

Dissertation
zur Erlangung des Grades eines Doktors der Naturwissenschaften

vorgelegt von
M. Sc. Mahmoud Al Humaidi

eingereicht bei der Naturwissenschaftlich-Technischen Fakultät
der Universität Siegen

21. Juli 2022

Supervised by: Prof. Dr. Ullrich Pietsch.

This thesis is dedicated to my beloved deeply-missed parents,,
Your memory beats inside me like a second heart

Zusammenfassung

Halbleiter-Nanodrähte mit quasi-eindimensionaler Geometrie haben in den letzten Jahrzehnten große Aufmerksamkeit erlangt. Die einzigartige Geometrie dieser Objekte trägt zu ihren unverwechselbaren optischen und elektrischen Eigenschaften mit vielversprechenden Möglichkeiten für neuartige Bauelemente bei. Die Bandlücke der Nanodrähte hängt von ihren Kristalleigenschaften wie den Kristallphasen und der Verspannung ab, die wiederum in hohem Maße modifizierbar sind. Daher ist die Herstellung und das Studium von Nanodrahtkristallen wesentlich für die Modifizierung und Kontrolle ihrer Eigenschaften. In dieser Arbeit wird eine Molekularstrahlepitaxie-Kammer zur Herstellung von GaAs-Nanodrähten verwendet und die Veränderungen der Nanodraht-Kristallstruktur während des Wachstums als Funktion des Abstands zwischen den benachbarten Nanodrähten untersucht. Die Untersuchung der Nanodrähte während des Wachstums in Arrays mit unterschiedlichen Drahtdichten mittels zeitaufgelöste Röntgenbeugung zeigt eine starke Abhängigkeit der Kristallstruktur vom Nanodrahtabstand. Diese Abhängigkeit wird zum Teil auf den Abschattungseffekt der Materialflüsse zurückgeführt, auf den sich der erste Teil dieser Studie konzentriert. Weiterhin wird die Entwicklung der Gitterverspannung in den Nanodrähten während des asymmetrischen Wachstums einer gitterfehlangepassten $In_xGa_{1-x}As$-Schale untersucht. Das asymmetrische Wachstum der Schale auf den Nanodrahtfacetten führt zu einer asymmetrischen Variation der Gitterverspannung über den Nanodrahtquerschnitt, die eine Biegung des Nanodrahtes hervorruft. Die über den Nanodrahtquerschnitt variierende Gitterverspannung kann für die Modifikation der Bandlücke sowie der optischen Eigenschaften des Nanodrahtes genutzt werden. Aus diesem Grund wird eine detaillierte Untersuchung der Gitterverspannung und der Nanodrahtbiegung durchgeführt. Die Entwicklung der Gitterverspannung und der Nanodrahtbiegung während des Schalenwachstums wird mit Hilfe von zeitaufgelöste *in-situ* Röntgenbeugung an einem einzelnen Nanodraht sowie an einem Nanodraht-Ensemble beobachtet. Diese Untersuchung offenbart eine nicht-lineare Abhängigkeit der Gitterverspannung und der Nanodrahtbiegung von der Dauer des Schalenwachstums, was auf Veränderungen der Wachstumsdynamik hinweist. Zuletzt wird der Abschattungseffekt der Materialflüsse durch die benachbarten Nanodrähte genutzt um die Verteilung des Schalenmaterials entlang der Wachstumsachse der Nanodrähte zu steuern, was zu einem variierenden Verspannungsfeld entlang der Wachstumsachse der Nanodrähte führt. Diese Methode kann für die Modifikation von Verspannungsgradienten und für Bauteile auf Nanodraht-Basis mit neuartigen Geometrien eingesetzt werden.

Abstract

Semiconductor nanowires with a quasi-one-dimensional geometry have gained great attention during the past decades. The unique geometry of these objects contributes to their distinctive optical and electrical properties that are promising for novel devices. The configuration of the band gap of the nanowires depends on their crystal properties such as the crystal phase and the strain which in turn are highly controllable. Therefore, the realization and the study of the nanowire crystal are essential for tuning and controlling their properties. In this work we use a molecular beam epitaxy chamber for fabricating GaAs nanowires and we investigate the changes of the nanowire crystal structure during growth as a function of the interspacing between the neighboring nanowires. By means of time-resolved X-ray diffraction technique, monitoring the nanowires during growth at arrays with different densities shows a high dependency of the crystal structure on the nanowire interspacing. This dependency is partially attributed to the shadowing effect of the growth material fluxes which we focus on in the first part of this study. Further, we investigate the strain evolution in the nanowires during an asymmetric growth of a lattice- mismatched $In_xGa_{1-x}As$ shell. The asymmetric growth of the shell materials on the nanowire facets results in an asymmetric strain variation across the nanowire cross-section, which induces nanowire bending. The varying strain across the nanowire cross-section can be utilized for engineering the band gap and the optical properties of the nanowire. Therefore, we perform a detailed study of the strain and nanowire bending. The evolution of the strain and nanowire bending during shell growth is observed by means of time-resolved *in-situ* X-ray diffraction technique on a single nanowire as well as on a nanowire ensemble. This investigation revealed a non-linear dependency of the strain and nanowire bending to the shell growth time, indicating changes of the growth dynamics. Lastly, we exploit the shadowing effect of material fluxes by the neighboring nanowires to control the distribution of the shell material along the nanowire growth axis, which results in a varying strain field along the nanowire growth axis. This method can be employed for strain gradient engineering and nanowire-based devices with novel geometries.

Contents

List of Figures

Chapter 1

Introduction

"I don't know how to do this on a small scale in a practical way, but I do know that computing machines are very large; they fill rooms. Why can't we make them very small, make them of little wires, little elements, and by little, I mean little?" - Richard Feynman

During the past decades, semiconductor nanowires (NWs) have been studied intensively because of their wide range of potential applications in modern and future electronics and optoelectronic devices [1–4]. Due to their small lateral dimensions and high surface-to-volume ratio, the nanowire geometry helps to efficiently collect the charge carriers, enhance light absorption and minimize material consumption [5–10]. In addition to that, nanowires can sustain strain more efficiently compared to their planar counterparts [11]. This strain can be utilized to modify the nanowire band-gap, and thus, the optical properties of the device [12]. To fully benefit their potentials, nanowires properties such as number density, volume, crystal structure and the strain must be controlled. To realize the first three properties, selective area growth (SAG) of nanowire patterns has always played a central role [13–27]. Regular arrays of nanowires have been realized by various methods ranging from top-down lithography to bottom-up epitaxy approaches [28]. Whereas the former approach is limited to homo-epitaxial or lattice-matched hetero-epitaxial structures, the latter allows the epitaxial integration of nanowires onto dissimilar substrates opening a way for epitaxial

integration of III-V nanostructures onto the cost-efficient Si platform [29–31]. The SAG enables control over nanowire position, number density, size and shape which is beneficial, if not prerequisite, for nanowire device integration and efficiency optimization [32–35]. So far, a high degree of control over the nanowire vertical yield, and nanowire size and shape has been demonstrated [14, 22, 26, 36–41]. In concert with experimental studies, substantial efforts have been dedicated to the modeling of the growth process of regular nanowire arrays, since it has become evident that a high nanowire area density affects the local availability of precursor species [16, 21, 26, 42–46].
This availability may vary locally as a consequence of several phenomena that are influenced by the nanowire interspacing (array pitch). In particular the competition between neighboring nanowires for adatoms feeding growth by surface diffusion and the shadowing of the material flux in case of molecular beam epitaxy (MBE) growth. The later phenomenon may result in a local change of the impinging material flux with growth time as the nanowires elongate [26].
The above effects can limit both axial and radial nanowire growth rate and eventually the nanowire volume and its elastic properties. Especially in self-catalyzed vapor-liquid-solid VLS growth, the local availability of growth species is even more crucial since it influences the chemical composition and the shape of the liquid catalyst droplet. The profile of the liquid droplet, in particular its volume, plays a key role in the VLS growth [47]. It is responsible for the evolution of crystal shape (tapering) [40, 41, 48], and its wetting angle determines the crystal structure (polytypism) [49–51].
Previously, the effect of nanowire area density on the local growth conditions was investigated for self-catalyzed nanowires [44, 51]. So-far, the effect of shadowing in ordered arrays of nanowires on their crystal structure as well as the shell growth and strain along the nanowire in core-shell system is not known. In this context, time-resolved *in-situ* X-ray diffraction (XRD) investigation of nanowires grown in arrays with different densities would grant valuable insights into the effect of material-flux shadowing on the evolution of crystal structure and strain distribution of core-shell nanowire. For the realization of the strain in the nanowires, a conventional way is the combination

of materials with different lattice parameters in the form of radial heterostructures [52–54]. In the radial heterostructure (*i.e.* core-shell nanowires), the non-uniform distribution of a lattice-mismatched shell around the nanowire results in inhomogeneous radial strain. In case of the growth of a shell with larger unit cell, the tensile strain at the shell interface releases gradually across the nanowire cross-section. As a consequence of the elastic release of interface strain, thin nanowires bend if the heteroepitaxial shell is grown inhomogeneously on their perimeter [55, 56]. The spatially varying strain field by means of nanowire bending opens up new possibilities for band-gap engineering, whereas, due to the continues changes of the inter-atomic spacing, charge carriers drift to the tensile strained regions of the nanowires [57]. Additionally, nanowires that bend fully backwards to contact either neighboring nanowires or the substrate, serve as a new way to form nanowire electrical and optical interconnects [55]. The strain and the consequent bending can be manipulated by controlling the volume ratio of the core and shell or by controlling the composition of the ternary alloys. Furthermore, the strain distribution along the nanowire can be controlled by the layout of the patterned nanowire arrays and the layout of the MBE effusion cells. The well-defined nanowire pattern with respect to the incident angle of the material fluxes allows to exploit the shadowing of these fluxes by neighboring nanowires to control the distribution of the shell material along the nanowire and the resulting strain and the bending profile of the nanowire. Due to its high sensitivity to the changes in the crystal structure, $in-situ$ XRD measurements of nanowire ensembles during the asymmetric growth of a lattice mismatched shell give deep insight into the strain evolution as well as the resulting nanowire bending.

This thesis is devoted to the understanding of the influence of the geometrical alignment of the MBE cells and the shadowing effect of the material fluxes on the axial distribution of the polytypism and the strain along the nanowire in case of core and core-shell nanowires, respectively.
Following this introduction, in chapter 2, we introduce the experimental methods that have been used in this work. At first, a brief introduction to the the Ga-assisted MBE growth of GaAs nanowires by VLS growth tech-

nique is given. Following this, we extend the discussion to the vapor-solid (VS) growth mode of the $In_xGa_{1-x}As$ shell. Next, we discuss the crystal structure of GaAs nanowires where we focus on the wurtzite (WZ) and zinc-blende (ZB) polytype. Finally, we introduce the *in-situ* XRD method of characterizing the nanowire crystal structure and the strain. At the end of this chapter, the used portable MBE system is introduced.

In chapter 3, we investigate nanowires grown in arrays with pitches ranging from $p = 100\,\text{nm}$ up to $p = 1000\,\text{nm}$ located on the same wafer, thus ensuring identical global parameters for nanowire growth, to observe the correlation of nanowire crystal structure and the array pitch p. By the time-resolved *in-situ* XRD experiment, we identify the influence of the onset of Ga-flux shadowing on the crystal structure at different arrays with different pitch p. The impact of Ga-flux shadowing on the crystal structure is explained by Ga-flux modeling considering specular reflection of Ga atoms and Ga-flux shadowing that causes a deflation of the liquid Ga-droplet, emphasizing the important role of the secondary reflected Ga-flux for patterned nanowire growth.

In chapter 4, we study nanowire bending in case of growing an $In_xGa_{1-x}As$ shell with x nominal indium content onto GaAs cores without substrate rotation. In this part we use GaAs nanowire templates grown on two types of Si(111) substrates coated with naturally grown SiO_x on one hand and thermally grown SiO_x on the other hand where the later is patterned by electron beam lithography. Following this, statistical information extracted from *in-situ* XRD measurements on nanowire arrays demonstrates that the nanowire curvature as function of the shell thickness has nonlinear dependency at the early stages of shell growth. We then extend our study with *in-situ* XRD investigation of a single nanowire during asymmetric shell deposition. This experiment allowed us to access and measure the strain and the small nanowire bending induced by early stages of the shell growth.

In chapter 5, we report on GaAs nanowire growth on pre-patterned Si(111) substrates followed by a lattice mismatched $In_xGa_{1-x}As$ shell growth without substrate rotation. Benefiting from the prior knowledge of the nanowire bending direction we exploit the shadowing of the material fluxes by neighboring nanowires and consequently a varying strain distribution along the

nanowire and different bending profiles are obtained. Our findings are observed by *in-situ* XRD measurements performed at nanowire arrays with different pitch size (*i.e.* different number density of the nanowires) during shell growth.

Chapter 2

Background

2.1 Fundamentals of MBE growth

Nanowires which are quasi one-dimensional crystals can be grown out of many different materials, by means of different techniques. The growth of nanowires was first introduced by Wagner and Ellis in 1964 [58] by using chemical vapor deposition (CVD) to grow silicon nanowires. Since then, several synthesis methods have been developed such as Molecular Beam Epitaxy, Metal Organic Chemical Vapor Deposition (MOCVD), Chemical Beam Epitaxy. In general, epitaxy is the process of depositing a crystalline over-layer onto a crystalline substrate where the deposited over-layer is in registry with the substrate crystal. MBE is the technique of our choice to grow core and core-shell nanowires under ultra-high-vacuum condition by mean of vapor-liquid-solid (VLS) and vapor-solid growth mechanisms, respectively. The VLS mechanism of epitaxial nanowire growth is one of the leading methods for generating single crystalline nanowires with large numbers. However, the growth process of GaAs-$In_xGa_{1-x}As$ core-shell nanowires via VLS and VS mechanisms passes, mainly, through four steps :

- The deposition of Ga on the heated substrate leads to the nucleation of Ga liquid droplets (figure 2.1(a) and 2.1(b)) that are the seeds of the epitaxial growth of the nanowires.
- The simultaneous supply of As and Ga with a determined ratio (V/III

ratio) leads to a super saturation of the droplet and a crystallization of GaAs at the droplet-substrate interface which initiate the axial growth of the nanowire (figure 2.1(c)).

- The termination of the axial growth can be done by droplet consumption (figure 2.1(d)) by continues supply of As while the Ga source is closed till the complete crystallization of the droplet.
- The radial growth of $In_xGa_{1-x}As$ thin film (shell) around the nanowire core can be done with the absence of the liquid droplet via vapor-solid (VS) growth mechanism (figure 2.1(e))

2.1.1 Self-assisted VLS growth of nanowire

Under ultra-high vacuum conditions in the MBE chamber, the self-catalyzed growth was first introduced by Fontcuberta i Morral [59]. This process has always been linked to the existence of a plain or patterned oxide surface such as SiO_x [60–62].
In all steps of nanowire growth, the leading parameters are beam fluxes (*i.e.* the amount of material supplied to the system) and the substrate temperature.

The deposition and the formation of Ga-droplets

For the synthesis of III–V semiconductor nanowires which is based on the VLS mechanism, the catalyst droplets formed from group-III elements with a quasi-uniform size act as seeds for the growth of the nanowires. A preferable single crystalline substrate covered by a layer with a negligible sticking coefficient of both group-III and group-V adatoms, such as an amorphous oxide layer, is used. To form the catalyst droplets, the substrate surface is first covered with a group-III metal element, (*i.e.* Ga in our case) that has low melting point (figure 2.1(a)). The adsorbed adatoms incorporate into liquid droplet where the formation of these droplets follows the classical Volmer–Weber growth mode [63]. In our research, Si substrate with an oxide layer (SiO_x) is used for self-catalyzed single crystalline GaAs nanowires growth. However, the thin oxide layer may have inhomogeneities and de-

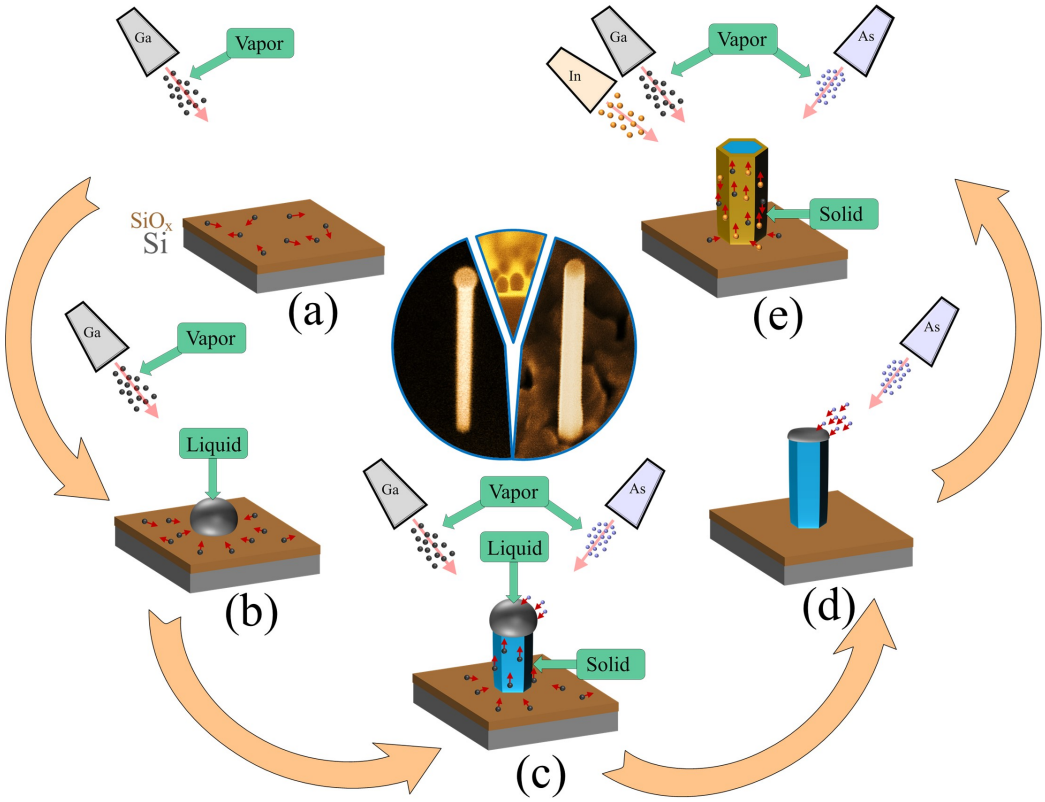

Figure 2.1: Core and core-shell nanowire growth steps. (a) Ga diffusion on the substrate surface. (b) The nucleation of Ga droplet on the substrate surface. (c) The axial VLS growth of the GaAs nanowire. (d) The consumption of Ga-droplet on the nanowire tip. (e) Radial VS growth of the $In_xGa_{1-x}As$ shell.

fects [64] that allow the condensed droplets to establish a contact with the substrate surface. These defects are the key to droplet collection where the density of nucleated Ga droplets on SiO_x was observed to be correlated with surface defects by orders of magnitude [65, 66]. The size of these droplets depends on the amount of the supplied Ga to the substrate surface and the substrate temperature. The influence of the substrate temperature on the droplet size is double sided, it can cause inflation or deflation of the droplets. High substrate temperature increases the diffusivity of the Ga adatoms on the substrate surface which, eventually, increases the collection rate of the Ga adatoms by the droplets. On the other hand, at high substrate temper-

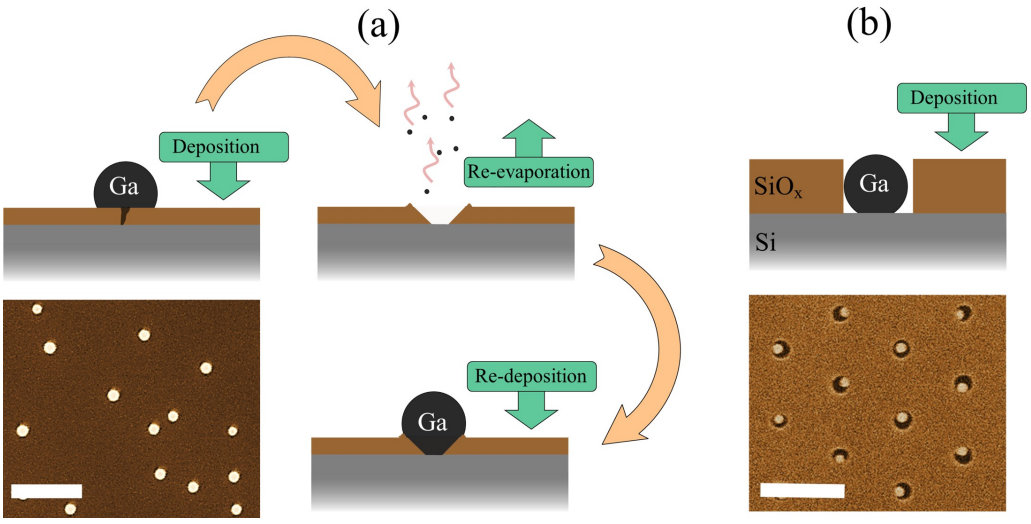

Figure 2.2: Droplet formation on substrates with (a) native oxide and (b) patterned thermal oxide with exemplary top-view SEM images of Ga droplets deposited on the corresponding substrate type. (Scale bars are 500 nm)

ature, the desorption rate of the Ga atoms increases which leads to droplets deflation [67]. In addition to this, the substrate morphology influences the droplet density. Therefore, the Ga flux and substrate temperature and morphology must be considered to control the droplet size and density which in turn plays an essential role in defining the number density, crystal phase and the morphology of the nanowires. To facilitate the collection of Ga droplet on the substrate surface and establish a contact with the Si crystals underneath the oxide layer, therefore enhance the yield of the epitaxial growth, nanoholes can be drilled in the oxide layer by the following two methods:

- In case of thin oxide layer that can be natively grown, nanoholes can be drilled by the desorption of Ga droplets by pre-growth annealing. The droplets at high temperature re-evaporate while etching the thin oxide layer performing self-organized nanoholes into Si surfaces. This method was established by Tauchnitz *et al.* [68], where the nanoholes which extend through the oxide layer down to the substrate crystal are the key to the collection of a second deposition of the droplets with facilitated contact with the single crystalline substrate (figure 2.2(a)).

- Alternatively, advanced lithographic techniques can be used to pattern the oxide layer with typical thickness of tens of nanometers (figure 2.2(b)). These techniques such as electron beam lithography (EBL) allow drilling of nanoholes with well defined positions and diameters. This method is advantageous for controlling the droplet size and density, which facilitate uniform growth of nanowire arrays with well define positions [19, 69–71].

GaAs nucleation and nanowire growth

By continues supply of group-V precursor, such as Arsine As with a constant pressure, these species dissolve into the liquid Ga droplet that assembles on top of a heated substrate (typically 500-600°C which is below the temperature required to thermally deoxidize silicon). The droplet then exceeds the equilibrium and becomes supersaturated and transforms to (Ga,As) liquid phase. At critical supersaturation level, 2D island driven by the thermodynamic forces start to form beneath the droplet and a crystalline mono-layer islands nucleates epitaxially to the substrate at the liquid-solid interface [72]. However, the dynamical evolution of these islands which are wetted by the droplet is complicated. But the kinetics of the crystallization by VLS growth is generally understood to proceed via the expansion of the 2D islands at the liquid-solid interface forming a thin mono-layer film. These mono-layers fundamentally accumulate vertically where each new mono-layer forms an upper facet of a growing nanowire. The formation of the epitaxial islands limits the growth of each new mono-layer. That means the liquid droplet must reach the critical supersaturation level, which in turn depends on the flux of the supplied materials, before a new mono-layer growth. Therefore, the rate of the axial growth depends on the wetting time of the successive crystallized mono-layer [72–74]. Since the whole procedure occurs beneath the liquid droplet, the morphology and the crystal structure of the nanowire depends on the droplet shape, as demonstrated by Krogstrup *et al.* [72]. In another words, the stability of the growth depends on the stability of the chemical potentials of the droplet at the top facet which is determined by

the supply of the growth species which are partially temperature-dependent. The influence of vapor fluxes of the growth precursors and the substrate temperature as growth parameters on the droplet shape and chemical stability can be realized as following

- **Ga-flux:** Under a constant As pressure and substrate temperature, increasing or decreasing Ga flux can progressively increase or decrease the diameter of the liquid droplet which eventually increases or decreases the diameter of the nucleated 2D mono-layers and the final nanowire diameter [72, 75]. Additional to the direct impingement of Ga atoms from the vapor flux to the droplet, Ga atoms adsorbed at the nanowire side-facets and substrate surfaces effectively diffuse to the droplet as adatoms that feed the liquid droplet [19,76–78]. The diffused Ga atoms on the nanowire side facets, however, may also form bonds with the incident As atoms and nucleate on the nanowire side-walls forming layers via vapor-solid mechanism that contribute to the evolution of the nanowire diameter during the VLS growth. However, this growth on side facets is rather slow and the main contributor to the nanowire diameter during the VLS growth is the droplet size.

- **As-flux:** At a constant Ga flux and substrate temperature, higher As supply to the liquid droplet (*i.e.* higher V/III ratio) leads to faster saturation of the droplet and consequently faster nucleation rate of the 2D mono-layers, and thus, faster nanowire axial growth. However, since it has lower vapor pressure than Ga, As is rather volatile and can be easily desorbed from the substrate surface at high temperature. Which means the collection of the As atoms from the surface is a secondary source of As supply to the liquid droplet while the major supply is by the direct impingement from the As vapor flux [79]. Continuous increasing or decreasing of As flux may decrease or increase the droplet size which in turn contributes to the changes in supersaturation rate as well as the top-layer nucleus crystal phase, respectively.

- **Substrate temperature:** As explained previously, the diffusion and desorption of Ga and As on the substrate surface and the nanowire

side-facets are temperature dependent. The changes in the substrate temperature during the growth leads to varying the mentioned behavior of both growth species thus, a variation of the adatoms ratio (V/III ratio) of both materials. For instance, higher substrate temperature leads to higher evaporation rate of As and higher diffusivity of Ga atoms on the substrate surface and the nanowire side facets which increase the supply rate of Ga adatoms to the liquid droplet [72].

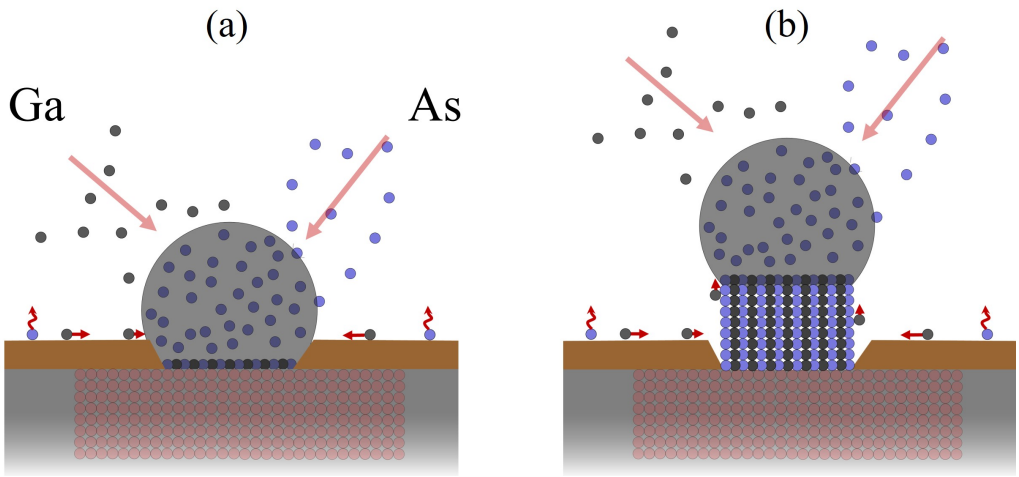

Figure 2.3: Illustration of the nanowire growth mechanism of GaAs nanowire. (a) The saturation of the catalyst droplet and the nucleation of an epitaxial mono-layer at the droplet-substrate interface. (b) The axial growth of the nanowire and the possible dynamics of the incident growth materials (desorption, surface diffusion and direct impingement).

The physical and chemical issues involved in the nucleation and growth of nanowire such as direct impingement of Ga and As adatoms, surface diffusion and desorption can be tuned by these three parameters. The precise consideration of these parameters determine the nanowire characteristics such as the size, shape, composition and crystalline structure. The nanowires resume growing as long as the liquid droplet is presented while continues fed of the growth materials vapor fluxes. The termination of the axial growth can be done by crystallizing the liquid droplet, which allows the radial growth on the nanowire facets by vapor-solid mechanism.

2.1.2 Vapor-solid mechanism of (shell) growth

The radial growth of the nanowires can be done via the vapor-solid growth mechanism, which is widely used for the MBE overgrowth of a shell around the nanowire core. This growth mode can be used by providing the same materials as the core nanowire (homoepitaxy) to increase the core diameter, or different material than the core nanowire (heteroepitaxy) for fabricating heterostructured nanowires [62,80]. However, this technique is different from the VLS growth mechanism by the absence of the liquid phase while supplying the growth species. In this technique, nanowire facets act as a substrate where mono-layer films are deposited. The adatoms of the vapor flux that land on the nanowire facets, are free to move on in all directions passing a distance λ (referred as a diffusion in figure 2.4(a)) until colliding with another adatom forming a stable nucleus and the formed nucleus is the seed of a new island [81]. Another fate of the adatoms is to meet and stick to an existing island that spreads accordingly to meet another island (figures 2.4(a) and 2.4(b)). The stability of the nucleus is determined by the energy of the diffused adatoms and the surface energy of the nanowire facets [81–83].
The diffusion coefficient D_{III} of group-III elements (Ga and In) which depends on the temperature and defined by the number of jumps Γ in unit time and the jumping step size (*i.e.* the lattice spacing (a)) is given by

$$D_{III} = \Gamma a^2 \tag{2.1}$$

This coefficient determines the nucleation and the growth of the mono-layers via the vapor-solid mechanism [84,85]. Higher island density can be achieved by lowering the diffusion of the adatoms, since lower diffusion means higher probability of the adatoms to collide and form nucleus. On the other hand, a large diffusion coefficient means a high probability for an adatom to find an existing island before another adatom is deposited in its vicinity to provide chance for nucleation, leading to an overall lower island density. Therefore, the competition between nucleation and growth is determined by the adatom diffusion coefficient. However, the nucleated adatoms systematically build up mono-layers epitaxially to the crystals of the nanowire side facets.

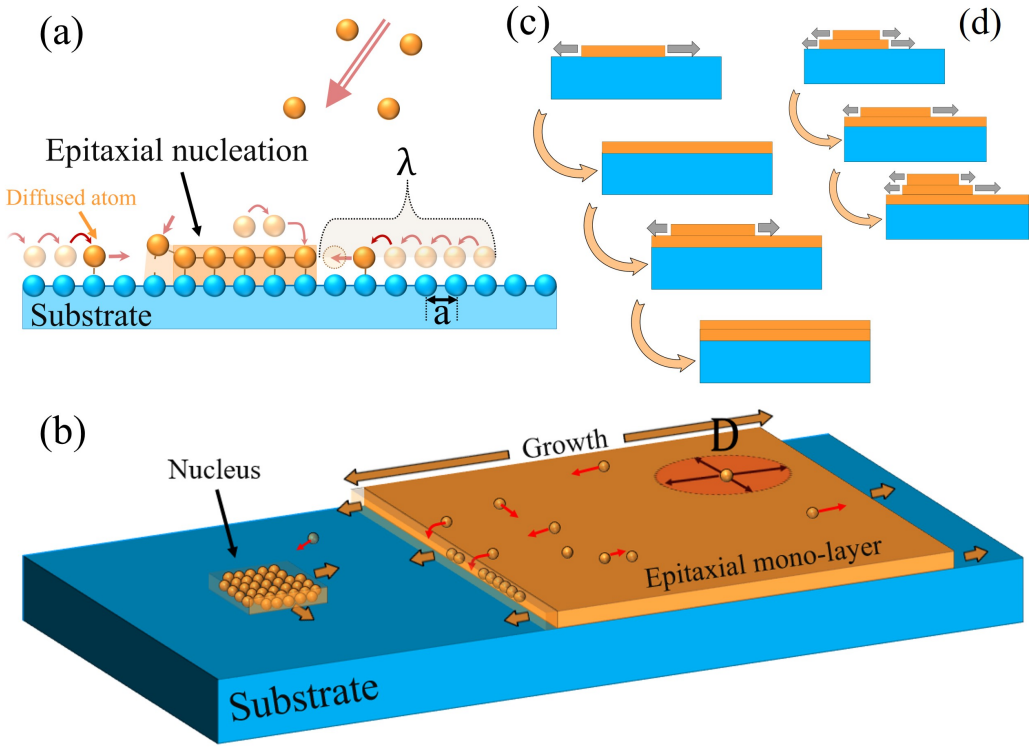

Figure 2.4: Vapor-solid growth mechanism, (a) Illustration of the diffusion of the incident atoms and the nucleation process. (b) The epitaxial growth of a mono-layer. (c) Layer-by-layer growth regime of a multi-layers film. (d) Step-flow growth regime.

This mode, (also known as Frank-van der Merwe mode [86]) requires lower energy of the substrate surface comparing to surface energy of the wetting mono-layer films. The wetting mono-layer reduces the surface energy of the substrate to an equilibrium, and consequently, smooth layer-by-layer growth regime occurs [82] (figure 2.4(c)). Therefore, for smooth layer-by-layer deposition of shell materials around the nanowire, a lower diffusion coefficient of group-III materials D_{III} is required which can be achieved by lowering the substrate temperature and increasing the vapor pressure of group-V materials. At higher substrate temperature a higher spreading rate of the nucleated islands leads to step-flow of a vertically stacked layers (also known as Stranski-Krastanov mode [87, 88])) that results in the formation of rough

surface (figure 2.4(d)). However, the formation of a rough surface can be resulted from changes in balance of forces due the strain in the growing layers typically due to the high lattice-mismatch in case of heteroepitaxial growth also known as Stranski–Krastanov growth. Surface roughness and the strain in the growing layers reduce the diffusivity of the material which in turn results in the formation of mono-layer islands with small surface area that stack on top of each-other forming quantum dots [89–92]. For the nanowires with hexagonal cross-section, in addition to the dependency on the temperature and fluxes ratios, the uniformity of the shell growth around the nanowire is influenced by the crystal orientation of the side facets and strain difference between the facets and the edges. Additional to this, in MBE systems the arrangement of the material sources plays a critical role in the shell growth mechanism [93] therefore, to compensate, a typical rotation of the nanowire with respect to the flux directions is required to obtain a homogeneous shell growth around the nanowire .

2.2 Crystallography of nanowires

2.2.1 Nanowire crystal structure and polytypism

GaAs along with all III-V semiconductors are featured with covalent bonds. Three electrons provided by the outer shell of the group-III atom (Gallium atom) are shared with five electrons provided by group-V atom (Arsenic atom) to form four covalent bonds. Therefore, in GaAs each Ga atom has four bonds to the nearest As atoms and vice versa, forming a tetrahedral local atomic geometry of each Ga-As_4 (or Ga_4-As) polyhedron. At ambient conditions, the favorable crystal structure of the stoichiometric GaAs is zincblende (ZB) that consists of two stacked face-centered cubic lattice system, with equal basis vectors (a,b and c) that determine the unit cell [94]. All these vectors are equal to the lattice parameter (a_{ZB}) as demonstrated in figure 2.5(a). However, during the self-assisted VLS growth, due to some kinetic reasons which will be discussed later, GaAs nanowires grown epitaxially on Si(111) substrate can adopt the hexagonal wurtzite (WZ) crystal

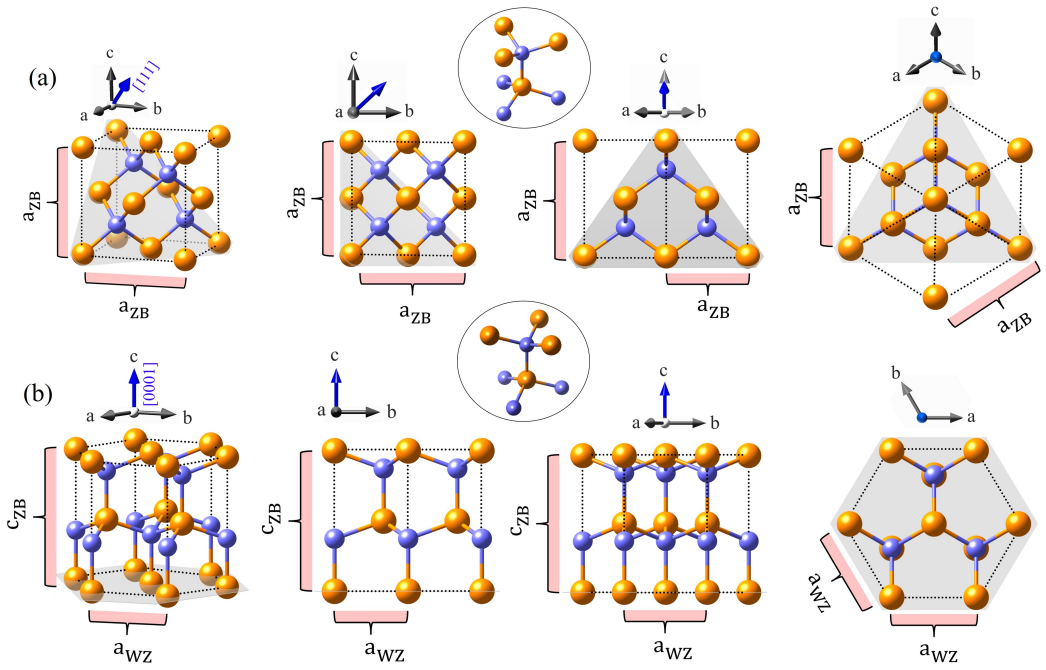

Figure 2.5: 3D schematic illustration of the nanowire crystal structure (ball and stick model) of (a) zincblende (ZB) and (b) wurtzite (WZ) structures with different rotations, the gray plane is the epitaxial growth plane of the ZB(111) and the equivalent WZ(0001), and the direction of the growth with respect to the lattice vectors is indicated by blue arrows at all rotations.

structure that can exist as segments with varied lengths along the nanowire. Both structures are closely related, but the local tetrahedral coordinate of the hexagonal WZ might have one Ga-As bond length that is slightly shorter than the other three Ga-As bonds [95, 96] while the ZB structure has ideal tetrahedral coordination. The slight variation of the bond length in the WZ tetrahedral coordinates leads to different configuration of the bonds compared to ZB structure and the cohesive binding energy of the WZ is higher than the one of ZB ($\delta E = E_{WZ} - E_{ZB} \approx 24meV/bond$) [94]. Thus, the unit cell of the WZ structure is determined by two lattice parameters (a_{WZ} and c_{WZ}). The coexistence of both structures is referred as polytypism in literature. The structure parameters of both crystals are listed in table 4.1. Since the axial growth of the nanowires occurs in layer-by-layer regime, both structures are characterized by their respective stacking sequence of planes

decomposed of atomic bi-layers of Ga and As (parallel to the gray planes in figure 2.5) on top of each other. For the ZB crystal, the stacked layers are perpendicular to the [111] direction and follow an ABCABC... type of stacking sequence while the WZ bi-layers that are perpendicular to [0001] direction follow the ABAB...type of stacking sequence as depicted in figures 2.6(a) and 2.6(c), respectively. However, stacking faults and rotational twin segments (corresponding to a 180° rotation of atomic positions of the non-twinned structure around a twin axis) cause an interruption or reversion of the ABCABC... stacking sequence of the ZB. Stacking faults occur at the twin boundaries, where the reversion of stacking sequence of the atomic layers take place, generating local layer sequence such as "ABC(A,B,C|C,A,B)CBA".

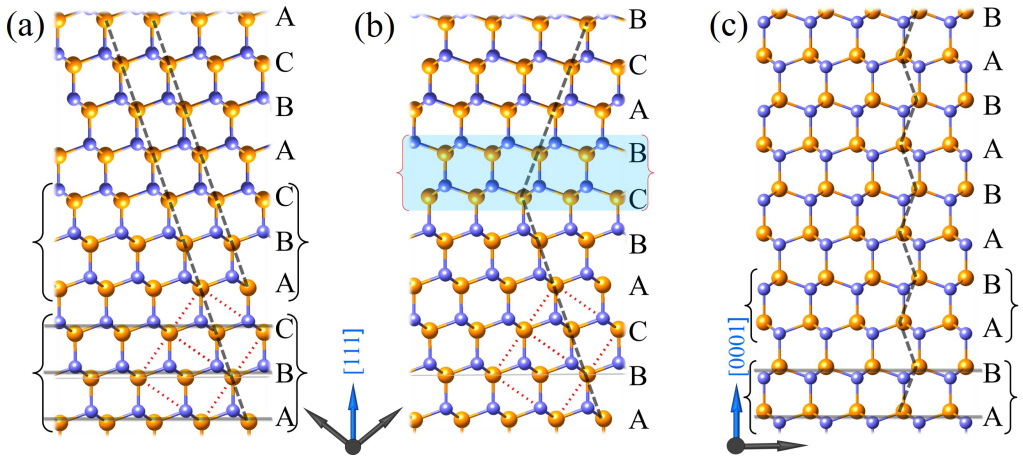

Figure 2.6: 2D schematic illustration of the nanowire crystal structure (Ball and stick model) of (a) Zincblende structure and the sequence ABCABC of its bilayers along [111] direction. (b) Zincblence and twin-Zincblende sequence of ABC-CBA and a stacking fault boundary at CB. (c) Wurtzite structures the bilayers sequence of ABABAB along [0001] direction.

These stacking faults were associated with the defects of the optical and electronic properties of the nanowires [97–99]. The valence and conduction bands of the ZB and WZ structures are misaligned, so the small section of one phase within the other results in charge carrier confinement and local quantum-size effect. Therefore, fundamental understanding and governing their formation is important for fabricating nanowires that are reliable for

technological applications.

Table 2.1: Structure parameters of zincblende and wurtzite GaAs [95, 96].

Structure	zincblende (ZB)	wurtzite (WZ)
Space group	F-43m (216)	P63mc (186)
Lattice	2 FCC sub-lattices	2 hexagonal sublattices
Basis	Ga(0,0,0) As($\frac{1}{4}, \frac{1}{4}, \frac{1}{4}$)	Ga($\frac{1}{3}, \frac{2}{3}, 0$) As($\frac{1}{3}, \frac{2}{3}, u = 0.373$)
Bond lengths [Å]	2.448 (4 bonds)	2.448 (1 bond) 2.449 (3 bonds)
Lattice parameters [Å]	a=5.65359 b=5.65359 c=5.65359	a=3.989 ±0.001 b=3.989 ±0.001 c=6.564 ±0.001
Lattice vector along growth direction	[111]	[0001]
Inter-planar spacing [Å] along growth direction	$d_{111} = 6.5282$	$d_{0001} = c$

2.2.2 Polytypism formation mechanism

Early explanation of the microscopic origin of the polytypism in III-V nanowires was given by Akiyama *et al.* [100] by considering an empirical inter-atomic potential, which incorporates electrostatic energy due to covalent-bond and ionic charges. Their model suggests that the existence of WZ structure is based on the minimized surface energies of the side-wall facets caused by the lower number of dangling bonds for certain diameters ranging from 1-22 nm. Furthermore, the existence of both polytypes was reported to occur for nanowires with diameters ranging from 12-32 nm. However, this model failed to explain the experimental observation of stacking faults, twinning as well as polytypism in nanowires with diameters of few hundred nanometers. As described previously, the growth of the top facet mono-layer at the liquid-solid interface is limited by the formation of a nucleus with a critical size that is defined by the energy cost of replacing the top facet surface with the nucleus top surface. The surface energy in turn depends on the chemical potential of the liquid droplet. The orientation of the new nucleus with respect to the preceding mono-layer will determine the orientation of the new mono-layer to form whether ZB or WZ phase structure [101–104]. These processes make it difficult to understand the formation of the polytypism based on purely thermodynamic consideration. The kinetic model of formation mechanism of the WZ phase in III-V semiconductor nanowires under ambient conditions was first provided by Glas *et al.* [103] considering the case of gold-catalyzed MBE growth of GaAs nanowires on GaAs substrate. This model suggests that the mono-layer nucleus is in contact with the vapor phase at the edge of the nanowire facet where the solid nanowire, liquid Au-droplet and the vapor of the growth materials meet (referred as triple-phase-line TPL) assuming that the top facet at the liquid-solid interface is perfectly flat. But the *in-situ* TEM experiments in [73,104–108] showed that in the steady-state VLS growth mode the top facet can be truncated. This truncation increases the stability of the droplet on the nanowire tip and the degree of the truncation depends on the droplet size [106] and the droplet supersaturation [73], that might change during the growth. The nucleation, according to Wen *et*

al. [73] at the point where the top facet meets the edge of the truncated facet is favorable because extending the facet would require lower energy than introducing a new step. The previously mentioned experimental and theoretical studies express the imperative influence of the liquid droplet profile on the crystal structure of the grown nanowires. Jacobsson *et al.* [107] endorsed this by the direct observation of the nucleation events of the top facet mono-layers during the MOVPE growth of Au-assisted GaAs nanowire by means of *in-situ* TEM measurement. The *in-situ* TEM monitoring of the crystal changes over a wide range of wetting angles (φ) of the droplet on the nanowire top facet showed that the wetting angle (refereed there as contact angle) is the sole parameter that determine the crystal structure of the growing top mono-layers. The size of the droplet in turn depends on material supply as explained in the first section of this chapter. While tuning the droplet size from large droplet (*i.e.* large wetting angle of $> 130°$ on the tip of a nanowire with ZB phase structure, Panciera *et. al.* [108] observed the first transition from ZB to WZ at a wetting angle of $\sim 125°$ and the second transition from WZ to ZB at wetting angle of $\sim 100°$. These transitions are accompanied by a modification of growth fronts where at large wetting angle of the droplet, the edges of the nanowire top facet get truncated and the side facets changes from vertical to tapered (as depicted in figure 2.7). The changes of these facets change the surface energy balance at the TPL, which in turn determines the preferred crystal structure. The model that was suggested in [108] to predict the morphology of the growth interface and the preferred crystal structure as function of the wetting angle is rationalized by presenting the difference of surface energies at the TPL. By considering that the solid-vapor surface energies are phase dependent (k=ZB or WZ), the difference of the top facet energy whether being tapered (t) or truncated (tr) and the surface energy of the side walls which is inclined by θ is given by the following equations

$$\Delta F_t^k(\theta, \varphi) = \frac{\gamma_{\theta V}^k}{\cos\theta} - \gamma_{0V}^k - (\gamma_{SL} + \gamma_{VL} \cos \varphi) \tan \theta \tag{2.2}$$

$$\Delta F_t^k(\alpha,\varphi) = \frac{\gamma_{\alpha L}}{\cos\alpha} - \gamma_{0V}^k - \gamma_{SL}\ \tan\ \alpha + \gamma_{LV}\ \sin\ \varphi \tag{2.3}$$

where γ_{SL} and γ_{LV} are the surface energies of the solid-liquid (top facet) and the liquid-vapor interfaces, respective; $\gamma_{\alpha L}$ is the solid-liquid interfaces of the truncated edge of the top facet is inclined at the angle α to the vertical; γ_{0V}^k is the surface energy of the vertical sidewall facets (ZB(110) and WZ(1-100)); and $\gamma_{\theta V}^k$ is the surface energy of the tapered sidewall facet, inclined by θ to the vertical (see figure 2.7(a)). This model provides three distinct regimes of the polytypism formation during the growth as depicted in figure 2.7 can be summarized as following:

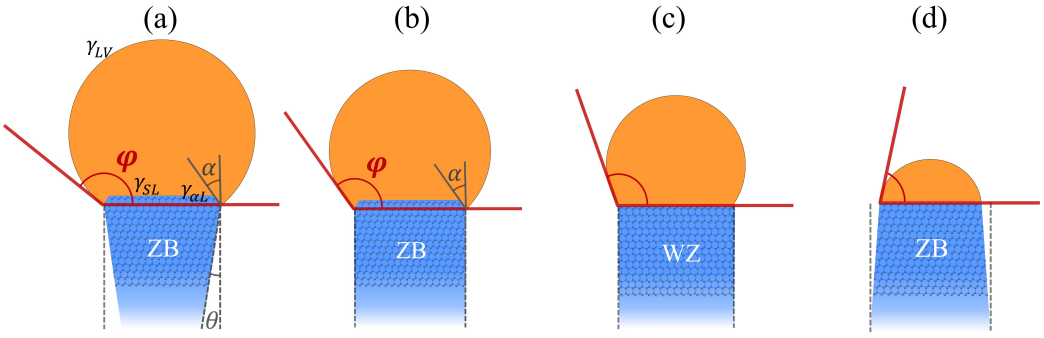

Figure 2.7: The configuration of the droplet wetting angle and nanowire morphology and crystal structure at different ranges. (a) Large droplet with large wetting angle $\varphi > 127°$ the top facet is truncated ZB and the sidewalls facets are tapered. (b) Smaller wetting angle close to the transition from ZB to WZ at $125° < \varphi < 127°$ the top facet is truncated ZB but the sidewalls facets are vertical (i.e no tapering) (c) at wetting angle of $100° < \varphi < 125°$ the top facet is flat WZ and the sidewalls facets are vertical and (d) at small wetting angles $\varphi < 100°$ the top facet is flat ZB and the sidewalls facets are inversely tapered.

- **Large wetting angle** ($\varphi > 127°$)
  The top-layer is truncated and the ZB phase occurs at these wetting angles and the formation of each new top mono-layer is quasi-instant. The truncated facet that oscillates within the growth cycles of the top mono-layers is in contact with the TPL and the edge of this facet serves

as an extra source of As for the rapid formation of the mono-layers. The ZB phase adjusts the nanowire diameter to the changes in the wetting angle and leads to outward tapering side facets (figure 2.7(a)). At the lower limit of the this range (close to the transition from ZB to WZ at $125° < \varphi < 127°$) the top facet truncation angle decreases and the nanowire has vertical ZB(110) sidewalls (figure 2.7(b)).

- **Intermediate wetting angle** ($100° < \varphi < 125°$)
  The top facet is flat and WZ phase forms at this range of wetting angles. The new mono-layer nucleates at the TPL and extends on the top facet in slow step-flow. Krogstrup *et al.* [72] suggest that the nucleation at the edge eliminate some of the liquid-vapor interface energy by the creation of nucleus-vapor interface. Therefore, the energy of the new nucleus that is partially in contact with the vapor is reduced and the metastable WZ phase is favorable to compensate the energy reduction and preserves the equilibrium at the liquid-solid interface and the nanowire maintains a constant diameter (figure 2.7(c)).

- **Small wetting angle** ($\varphi < 100°$)
  At smaller wetting angles, the ZB phase forms at the TPL and spread in slower manner. In this case, when the droplet changes in size, the system tends to maintain a larger wetting angle leading to changes of the top mono-layer diameter and resulting in inclined side facets, *i.e.* inverse tapering as depicted in figure 2.7(d)).

However, these angular ranges for the polytypism formation may differ for different growth conditions such as the temperature, the growth rate and the nanowire diameter. In these regimes (for flat or truncated top-facets) the contact of the nucleus with the vapor face is dictated by the surface energy of the droplet. As mentioned in the previous section, the ratio of the supplied materials (V/III ratio) governs the droplet profile and thus the crystal structure of the nanowire.

2.2.3 Heterostructured nanowire and strain

Nanowires can be formed by radial or axial growth of dissimilar materials. The quasi one-dimensional geometry of the nanowires and the high aspect ratio are the foundation of fascinating structure property of the nanowire which permit their high sustainability to the accommodated lattice mismatch strain. The interaction of the low-dimensional components and their interfaces can give rise to electronic and optoelectronic characteristics of the semiconductor nanowires that are superior to the two-dimensional counterparts. In the case of the 2D planar systems, the strain that is induced by the growth of lattice mismatched materials can relax through the introduction of lattice imperfection such as dislocation, stacking fault and twinning. Considering the growth of an epitaxial layer on lattice mismatched substrates as depicted in figure 2.8(a), misfit dislocation might be the leading form of strain relaxation as illustrated in figure 2.8(b). In this case, when the layer thickness increases and exceeds a critical value (critical thickness t_c) it costs too much energy to strain the additional grown layer to match the crystal system of the substrates, thus, the strain relives by introducing misfit dislocations [85, 109, 110]. However, the high elasticity of the thin nanowires allows maintaining the lattice coherency across the interface between two lattice mismatched structures during heteroepitaxial growth. In case of homogeneous radial heteroepitaxy (*i.e.* homogeneous shell growth) around the nanowire core, to maintain the same in-plane dimensions the two structures would share the same lattice parameter along the interface. In this case, the engineer-able strain can be used to tune the nanowire properties such as their band gap and charge-carriers mobility. Therefore, the pseudomorphically strained core-shell nanowires can be used to fabricate novel heterostructure-based semiconductor devices for optoelectronic applications [12, 57, 72, 111, 112].

In case of growing shell layers with larger unit-cell, on one hand the shell lattice is subjected to a compressive axial strain that is parallel to the growth direction. On the other hand, a tensile radial strain occurs perpendicular to the growth direction in attempt to maintain the total lattice energy following

Poisson's ratio. At the same time, the nanowire core is subjected to a strain with reversed configuration (*i.e.* a compressive radial strain and a tensile axial strain). In figure 2.8(c) the Poisson effect is demonstrated by the red and blue boxes for the shell and the core, respectively.

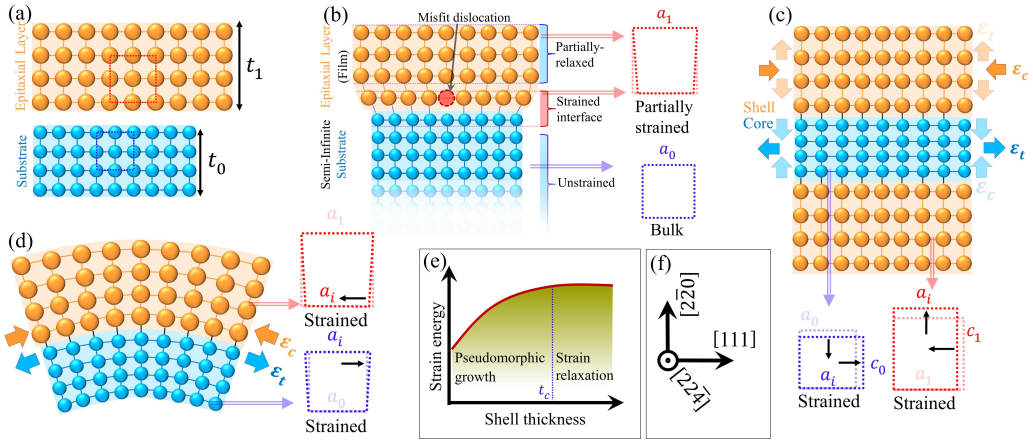

Figure 2.8: Fundamentals of heteroepitaxial strain. (a) Schematic of the planar model of a lattice mismatched substrate and an epitaxial layer with different unit cells. (b) Schematic of misfit dislocation that plastically relaxes the strain in case of quasi-infinite substrate thickness (bulk substrate). (c) Schematic of the tensile and compressive strain induced by the lattice mismatch between the nanowire core and shell with a demonstration of the changes of thier lattice parameters on two directions (Poisson's ratio). (d) Schematic of gradient strain relaxation by nanowire bending in case of asymmetric shell. (e) Typical changes in strain energy and epitaxial structure as function of shell thickness. (f) Crystal orientation in case of nanowire growth along [111] direction that is applicable to the nanowire schemes in (c) and (d).

In case of shell deposition on one side of a thin lattice mismatched nanowire core, the strain may partially relive by inducing nanowire bending (figure 2.8(d)). To maintain the same in-plane dimensions, the core-shell system will be stretched axially, resulting in curvature of the nanowire which in turn reduces the strain energy induced by the lattice mismatched shell. In the case of $In_xGa_{1-x}As$ shell growth on GaAs nanowire core, the axial strain relaxes gradually across the nanowire diameter from tensile at the interface to compressive or totally relaxed on the other side. The experimental study

of nanowire bending will be discussed in more details in chapter 4. The axial growth direction in this demonstration is the same direction [111] in figure 2.8(f). However, for a lattice constant a_1 of a thin epitaxial layer (shell) with thickness t_1 that grow on a substrate (nanowire core) with a lattice constant a_0 and thickness t_0, the misfit strain ϵ in the shell in planar model is equal to the misfit parameter f that is defined for a finite size by the equation [113]

$$\epsilon = f = \frac{a_1 - a_0}{a_1} \tag{2.4}$$

Due to the interactive stress at the core-shell interface, the lattice of the core also shares the misfit strain. Therefore, the misfit strain that is perpendicular to the growth direction (*i.e.* nanowire axial strain) in the core and the shell can be estimated by

$$\epsilon_{core} = \frac{a_0 - a_{||}}{a_0} \tag{2.5}$$

$$\epsilon_{shell} = \frac{a_1 - a_{||}}{a_1} \tag{2.6}$$

$$\epsilon_{||} = \frac{a_1\, G_1\, t_1 + a_0\, G_0\, t_0}{G_1\, t_1 + G_0\, t_0} \tag{2.7}$$

where $a_{||}$ is the shared lattice constant by the core and shell layers, and G_0 and G_1 are the shear moduli of the core and the shell materials. In equations 2.6 and 2.7, the negative or positive values of ϵ indicate compressive or tensile strain, respectively [113, 114].

In case of GaAs-$In_xGa_{1-x}As$ core-shell nanowires grown along [111] direction, the directional Poisson ratios of the crystals along the nanowire diameter on ($x \parallel$ [2-20]) and ($y \parallel$ [22-4]) and along the nanowire growth axis ($z \parallel$ [111]) are given by

$$\nu_{xy} = \frac{2(C_{11} + 5C_{12} - 2C_{44})}{3(C_{11} + C_{12} + 2C_{44})} = 0.61 \tag{2.8}$$

$$\nu_{xz} = \frac{4(C_{11} + 2C_{12} - 2C_{44})}{3(C_{11} + C_{12} + 2C_{44})} = 0.49 \tag{2.9}$$

where C_{ij} are the elastic constants for the GaAs(ZB) phase [115]. These ratios mean that a tensile strain (ϵ_t) of the GaAs core along [111] direction result in compressive strain (ϵ_c) along the perpendicular directions (*i.e.* [2-20] and [22-4]) as depicted in figure 2.8(c).
The total strain energy (E) in the core-shell system can be estimated by

$$E = E_{core} + E_{shell} = 2At_0G_0\epsilon_{core}^2\frac{1+\nu_0}{1-\nu_0} + 2At_1G_1\epsilon_{shell}^2\frac{1+\nu_1}{1-\nu_1} \qquad (2.10)$$

where A is the interfacial area and ν_0 and ν_1 are the Poisson's ratio of the core and the shell, respectively. According to equation 2.10, the strain accumulates quickly as the shell thickness increases. However, the increase of the strain as function of shell thickness is limited by the elasticity of the core-shell materials.
The excess strain energy would release by a relaxation process at high shell thickness where the shell growth is no more pseudomorphic (figure 2.8(e)). In this case the heteroepitaxial core-shell system stabilize while the overall Gibbs free energy is minimized [85].

The effect of misfit strain on epitaxial growth

As it was discussed in section 2.1.2, the epitaxial growth of the shell is governed by thermodynamical quantities, like, the free energy of the shell surface and shell-core (film-substrate) interface. Also, the morphology of the growing shell is ruled, mainly, by the the kinetic quantities, such as the energy barrier for the nucleus and the diffusivity of the growth materials. However, in heteroepitaxy system the strain is involved, whereas, the lattice mismatch strain alters the thermodynamic properties of the growing shell by introducing strain component into the free energy of the system. Therefore, the activation energy for the nucleation changes accordingly. Additionally, since the growing shell tends to adopt more and more to its bulk lattice constant as it increases in thickness, the strain in the top layer decreases during growth. Therefore, the strain influences the diffusivity of the growth materials and the nucleation kinetics [117, 118]. For isotropically strained shell, the inter-

plane lattice constants vary accordingly which in turn changes the diffusion coefficient D_{III} of the deposited shell materials (equation 2.1) which dictates the surface morphology of the growing shell.

2.3 Experimental Methods

2.3.1 X-ray scattering from nanowires

The crystal structure of the nanowires can be characterized by X-ray diffraction (XRD) technique. In this study, we use a monochromatic X-ray beam with a wavelength in the range of Ångström that is comparable to the interatomic spacing of the irradiated crystals. The interference of the X-ray with the periodic lattice of the nanowire crystal results in Fourier transformation that we consider to picture the crystal structure of the nanowire. When the X-ray hits an atom, the electrons in the atomic shell absorb the energy of the incident X-ray and start to oscillate. Since this energy do not exceed the binding energy of the electrons it is released again in the form of spherical wave (see figure 2.9(a)). For elastic scattering, (*i.e.* $\gamma + e^- \rightarrow \gamma + e^-$), the kinetic approach suggests that the amplitude of the incident beam wave vector $|k_i|$ is conserved and $|k_i| = |k_f| = \frac{2\pi}{\lambda}$ where $|k_f|$ is the amplitude of the scattered X-ray and λ is the wave length. When the X-ray beam hits a finite particle with electron density $\rho(r)$, the scattering amplitude according to [119] is given by

$$A_0(r) \propto \int \rho(r)\, e^{ik_i r}\, dr \tag{2.11}$$

where $q = k_f - k_i$ is the scattering vector. This approximation is proportional to Fourier transformation of the electron density (ρ) in a volume with the radius r which determines the position of the scattering electrons from the scattering center as sketched in figure 2.9(b). At large observation distance R from the scattering center, the scattering amplitude is given by the coherent superposition of all waves scattered by all electrons located at distance r from the scattering center where the classical Thomson formula can be used to give the scattering amplitude by

$$A(r, R) = E_0\, C\, r_{el} \int \frac{e^{iq|R-r|}}{|R-r|}\, \rho(r)\, e^{ik_i r} d^3 r \tag{2.12}$$

Where r_{el} is the Thomson scattering length and C is a polarization factor that depends on the scattering geometry which is assumed constant. However, in

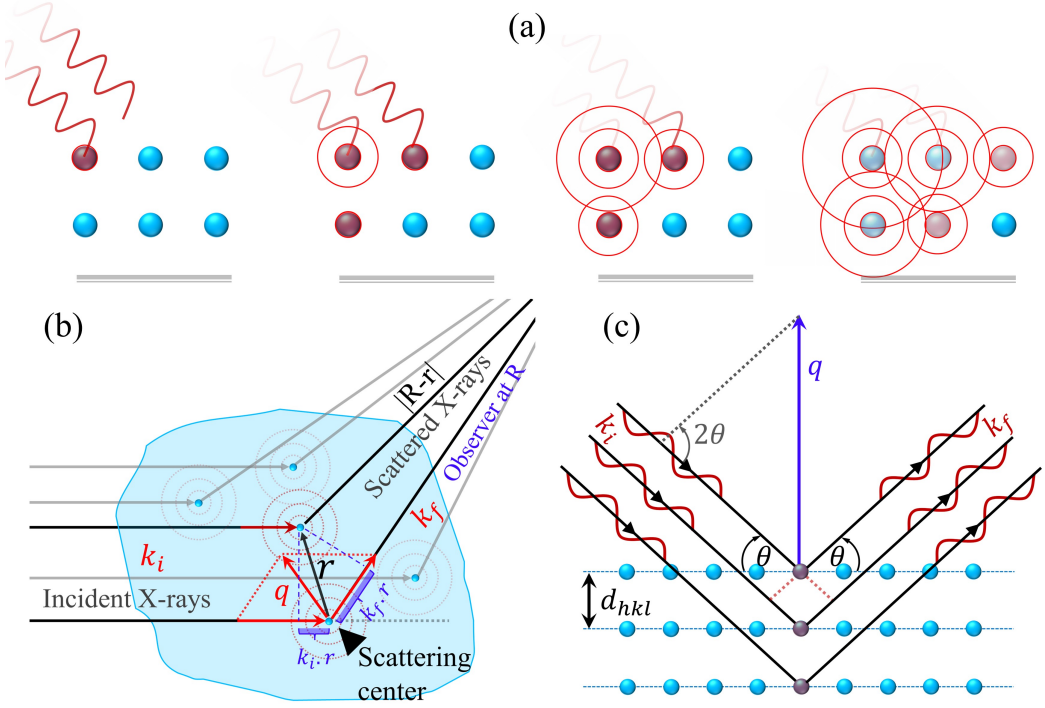

Figure 2.9: X-ray scattering. (a) X-ray scatted at the electrons of the atomic shells and the spherical X-ray waves sent out. (b) The scattering of the incident X-ray beam with wave vector k_i at to a particle with density $\rho(r)$ at different positions r. (c) Sketch of the X-ray diffraction geometry and Bragg condition.

the experimental geometry, the observing detector is tens of centimeters far from the scattering center (*i.e.* $r \ll R$) which means that Fraunhofer approximation is valid. For a beam size that is sufficient to illuminate the crystals of multiple nanowires, the scattering amplitude then becomes a function of the nanowires electron density and the coherent summation over all scattering waves is

$$A(q) = \text{Const.} \frac{e^{ikR}}{R} \int \rho(r) e^{iqr} \, d^3r \tag{2.13}$$

In an infinite and perfect periodic lattice, the integral vanishes whenever q is not equal to a certain value determined by the atomic spacing. At these values, a constructive interference of the scattering X-rays occur and can be described by Bragg's law. However, taking into account that for crystals with finite size, r may be given by the position of the unit cell in the crystal (r_c),

the position of the atom within the unit cell (r_a) and the electron distribution around this atom ($r_a^{'}$), therefore

$$r = r_c + r_a + r_a^{'} \tag{2.14}$$

Hence, the integral in equation 2.13 can be replaced by summation of all unit cells and all atoms included in each cell, and the scattering amplitude is

$$A(q) = \sum_n f_n e^{iqr_n} \sum_{cell} e^{iqr_c} \tag{2.15}$$

where f_n is the atomic form factor which gives the integral of the electron density of the atom n in the unit cell. The first sum is the structure factor and it determines the intensity of Bragg reflection and the second sum defines the possible location of the allowed Bragg reflection in 3D space defined by the wave vector components as will be described later.

Bragg's law is a measure of the inter-planar distances (d_{hkl}) where h,k and l are the Miller indices of the lattice plane given by the intersection of the plane with the crystal base vectors. A constructive interference of the partially reflected X-rays from these planes take place only at a certain angle of the incident beam as rationalized by Bragg's law [120]

$$n\lambda = 2d\ \sin(\theta) \tag{2.16}$$

where n is an integer number and θ is Bragg angle as sketched in figure 2.9(c). The inter-atomic spacing of the ZB and WZ crystal phase is different as explained in section 2.2 of this chapter which leads to different diffraction angle θ and different position in reciprocal space.

Diffraction geometry and reciprocal space mapping

To study and characterize any set of the lattice planes, Bragg condition must be fulfilled for the corresponding inter-planar spacing. In our study we focus on characterizing the structure of the lattice planes along the growth direction, *i.e.* GaAs(111) and GaAs(0001) lattice planes of ZB and WZ as discussed in section 2.2, respectively. For this purpose, we define a diffractometer-related geometry (*i.e.* lab geometry) which represents the alignment of the nanowire lattice with respect to the incident and the diffracted X-rays. In this geometry, z axis is set perpendicular to the substrate normal, thus z is parallel to the nanowire growth axis, x axis is perpendicular to the projection of the incident X-ray beam on the substrate surface and y axis is parallel to this projection as shown in figure 2.10(a). For this geometry the angles of the incident and diffracted beam (α_i and α_f, respectively) are taken with respect to x (*i.e.* with respect to the substrate surface). This geometry is called "*symmetric diffraction geometry*" where the diffraction is at the lattice planes that are parallel to the surface of the crystal. The other geometries called "*asymmetric diffraction geometries*" are of the inclined lattice planes with respect to the surface (more details about these geometries can be found in [121–123]). Once the incident X-ray hits the nanowire which has a hexagonal cross-section, the Fourier transformation that occurs is recorded by using a 2D pixel detector. The size of the detector and its position with respect to the sample in lab geometer can define the azimuthal angle ν of the diffracted X-rays.

The distribution of the X-ray signal can be recorded by rocking the lattice planes in the vicinity of Bragg angle θ_B as demonstrated in figure 2.10(b) that shows the star shape of the signal distribution (Fourier transformation of the hexagonal nanowire cross-section). The collected 3D map that consist out of multiple 2D images of the diffracted signal at different angles α_i and α_f determines the angular distribution of the signal in lab geometry. The angular range that is covered by the detector frame size can be measured by knowing distance between the sample (scattering center) and the detector. Accordingly, each frame taken at each angular step can be given by the

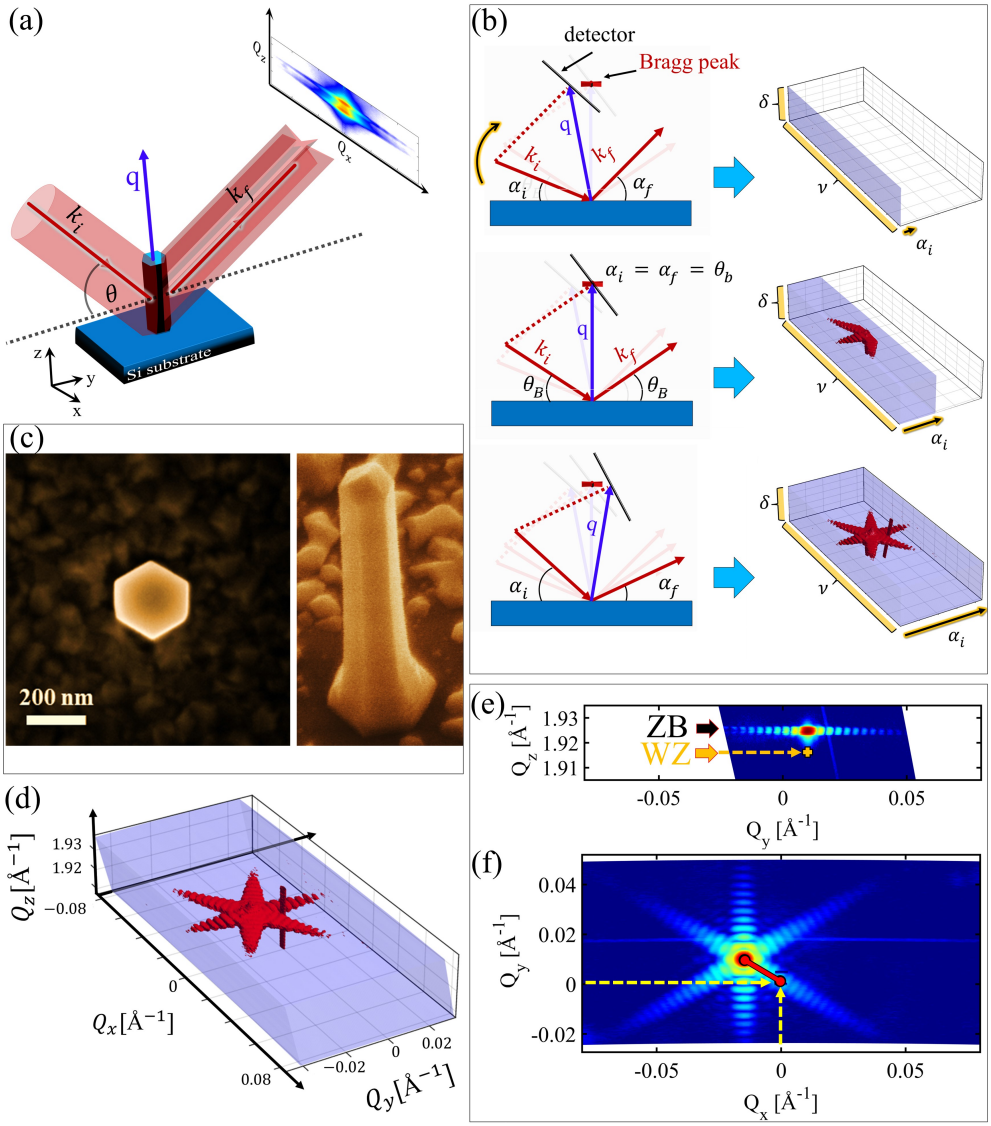

Figure 2.10: X-ray diffraction geometry and reciprocal space mapping. (a) Schematic illustration of XRD lab geometry. (b) Side-view demonstration of the symmetric XRD scans of a single nanowire and the collection of 2D frames at different angular steps. (c) Top and tilt view SEM image of the measured nanowire showing its hexagonal shape. (d) The measured 3D RSM of the XRD signal defined by the wave vector components. (e) 2D slice of the RSM on Q_yQ_z plane showing the position of the XRD peak of ZB and WZ polytypes on Q_z. (f) 2D slice of the RSM on Q_xQ_y plane showing the shifting from the origin of the RSM indicated by the red line.

reciprocal space vectors q that can be decomposed by [119]

$$\begin{aligned} Q_x &= \frac{2\pi}{\lambda}\sin(\nu) \\ Q_y &= \frac{2\pi}{\lambda}\Big(\cos(\alpha_f).\cos(\nu) - \cos(\alpha_i)\Big) \\ Q_z &= \frac{2\pi}{\lambda}\Big(\sin(\alpha_i) + \sin(\alpha_f).\cos(\nu)\Big) \end{aligned} \tag{2.17}$$

The 3D RSM of the XRD signal of the measured single nanowire is shown in figure 2.10(d). In our RSM geometry, the position of the XRD signal of the Si(111) substrate is considered as a reference. However, in RSM, Q_z lays parallel to the normal of the measured lattice planes (it is also parallel to the scattering vector q of the symmetric diffraction) and sensitive to the changes in their lattice spacing. The other vectors Q_x and Q_y are parallel to the measured lattice planes and determine their orientation. Therefore the profile of the XRD signal in RSM indicates the profile of the crystal structure of the measure sample. For instance, since the structure and the lattice spacing of ZB and WZ crystals are different their diffraction signal locate at two different position along Q_z in RSM as shown in figure 2.10(e). Also the orientation of the lattice planes along the growth direction (the alignment of the nanowire on the substrate) is given by the position of the XRD signal on Q_x and Q_y of the RSM. As demonstrated in figure 2.10(f), the signal is shifted from the origin of Q_x and Q_y which implies that this wire is tilted by an angle of 0.3° that can be easily measured. Therefore, Bragg diffraction is a sufficient method to study the nanowire crystal properties such as polytypism and strain as we be show in the following chapters.

2.3.2 Portable MBE for *In-situ* X-ray diffraction

The growth of all nanowire samples in this work has been performed in a special MBE system [124]. This system is designed for *in-situ* characterization and growth experiments. It has a small and compact growth chamber that makes it portable and suitable for heavy-load goniometer setup at the synchrotron radiation facilities in term of weight and dimensions. Beside the compact design, the portable MBE has two circular Beryllium windows which are transparent for X-rays for the *in-situ* XRD experiments. Additionally, this system is equipped by built-in setup for *in-situ* reflection high-energy electron diffraction (RHEED) [125] for *in-situ* characterization of the crystalline materials surface during growth. Figure 2.11(a) shows a photograph of the pMBE loaded on a goniometer at beamline P09 at the German Electron Synchrotron facility (DESY). The layout of the pMBE system with respect to the XRD geometry is sketched in figures 2.11(b) and 2.11(c) from side and bottom-view, respectively. The pMBE chamber is equipped with solid source effusion cells of Ga and In, and valved cracker cell supplying As_4. All cells are inclined to the substrate normal by $\Phi = 28°$. The azimuthal angles (with respect to the substrate surface and the x,y plane of the lab-geometry) are 60° between the Ga and the In cells and 120° between the Ga and the As cells as illustrated in figure 2.11(b). The coordination of the XRD experimental geometry are indicated in figure 2.11 where the sample normal points in the direction of the z-axis which coincides with the GaAs[111] direction in our case. Due to the limitation of the Be windows that open an angular range of ±23° for the incident and diffracted beams, the choice of X-ray energy is limited for the given XRD geometries. In our case, we chose the beam energy of E=15 keV (wavelength 0.8265 Å) where the Bragg angle of the GaAs(111) is 7.2745° and all the required scans around it are covered by the angular range of the Be windows. In the following chapters, we reveal the influence of the geometrical alligment of the pMBE cells on the growth dynamics of the self-assisted GaAs nanowire and the shell deposition of the GaAs-$In_xGa_{1-x}As$ core-shell nanowire.

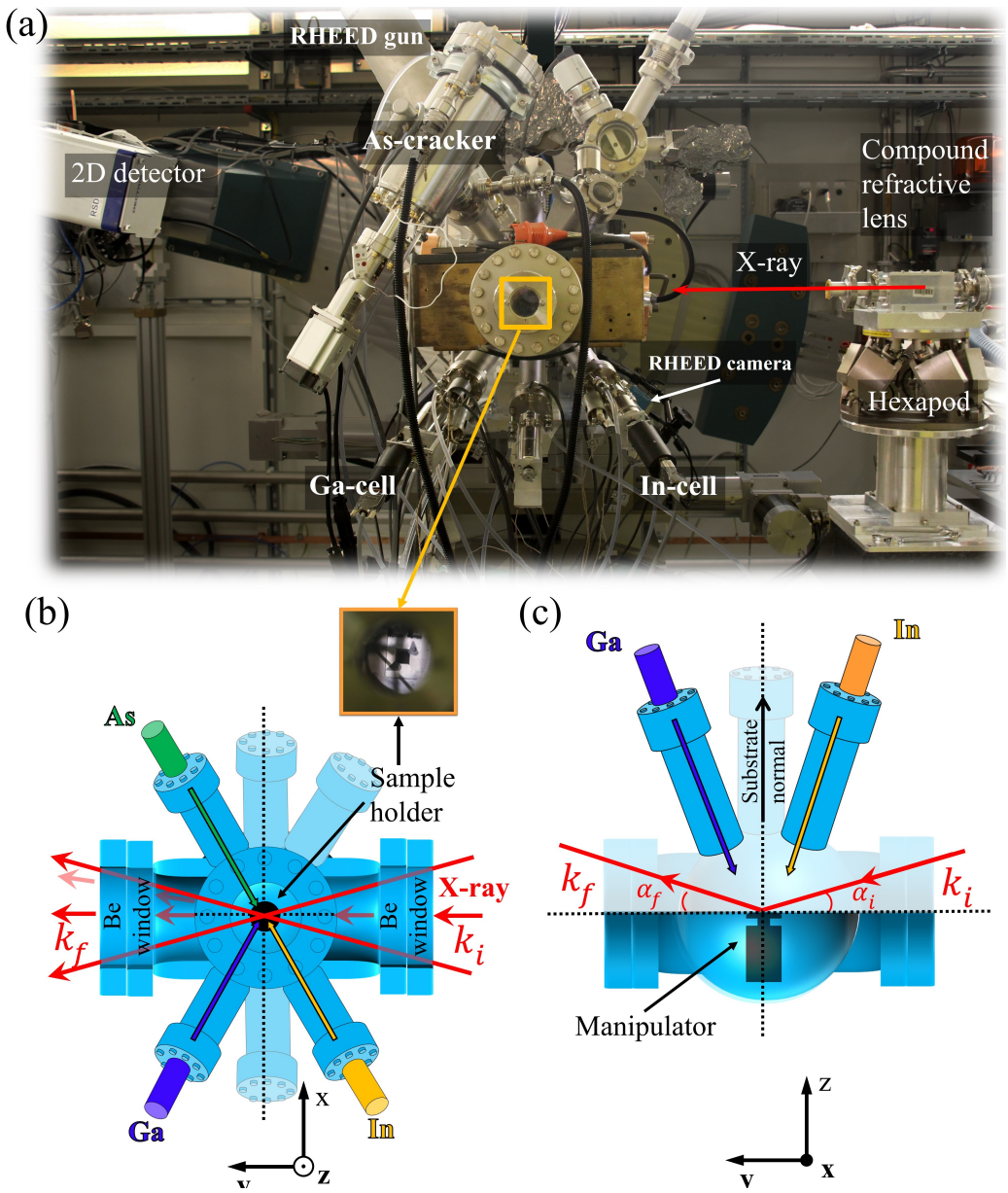

Figure 2.11: The portable MBE system. (a) A photograph of the pMBE setup on a heavy-load goniometer at beam-line P09 at DESY. (b) Side-view sketch of the pMBE cells with respect to the lab-geometry and the incident X-rays. (c) Bottom-view sketch of the pMBE.

2.3.3 MBE Growth of the GaAs-$In_xGa_{1-x}As$ core-shell nanowires

In our study, we use tow types of n-doped Si(111) substrates covered by a naturally grown silicon oxide (referred to as "native oxide" in the text) and

a thicker thermally grown oxide layer (referred to as "thermal oxide" in the text) with patterns of drilled nano-holes. Before the growth procedures, the two types of substrates require different sample treatments. The native oxide substrates pass through regular solvent cleaning by two rounds of dipping into acetone, isopropanol and ultra-pure water baths in ultrasonic cleaner, respectively. The patterned substrates with thermal oxide require hydrofluoric (HF) acid etching following the same regular solvent cleaning used for native oxide substrates. The etching is done using 0.5% HF for 1 minute to reduce the thickness of the naturally grown oxide on the substrate surface within the nano-holes. After oxide etching, the thermal oxide substrates are dipped into boiling ultra-pure water for 10 minutes for surface smoothing, this procedure was reported to improve the vertical yield of the nanowires [126]. Afterwards, the substrates are degassed under the ultra-high vacuum condition at 300°C for 30 min to get rid of solvent residuals before loading them into the MBE growth chamber. Material fluxes of the MBE effusion cells are calibrated via the respective layer-by-layer growth on epi-ready GaAs(001) substrate monitored by RHEED. The readout of the substrate temperature is calibrated to the temperature of the Ga-oxide removal of the same substrate.

Core-shell nanowire growth steps

We apply the growth procedure explained in 2.1.1 and 2.1.2, following the steps depicted in figure 2.11(a) for the patterned thermal oxide substrates.

1. At first, the substrates are annealed at a substrate temperature of approximately $T_{sub} = 800\,°\mathrm{C}$ in the MBE growth chamber for 30 min to get rid of any possible residuals from previous cleaning steps as further preparation step.

2. Within the holes, Ga catalyst droplets are formed at $T^{PD} \approx$ 600-630°C by depositing Ga for time t^{PD} with an equivalent GaAs thickness of 50-55 monolayer (ML).

3. Epitaxial VLS growth of the GaAs nanowire cores are initiated by supplying As and Ga simultaneously at $T^{NWG} \approx 630$°C and using V/III

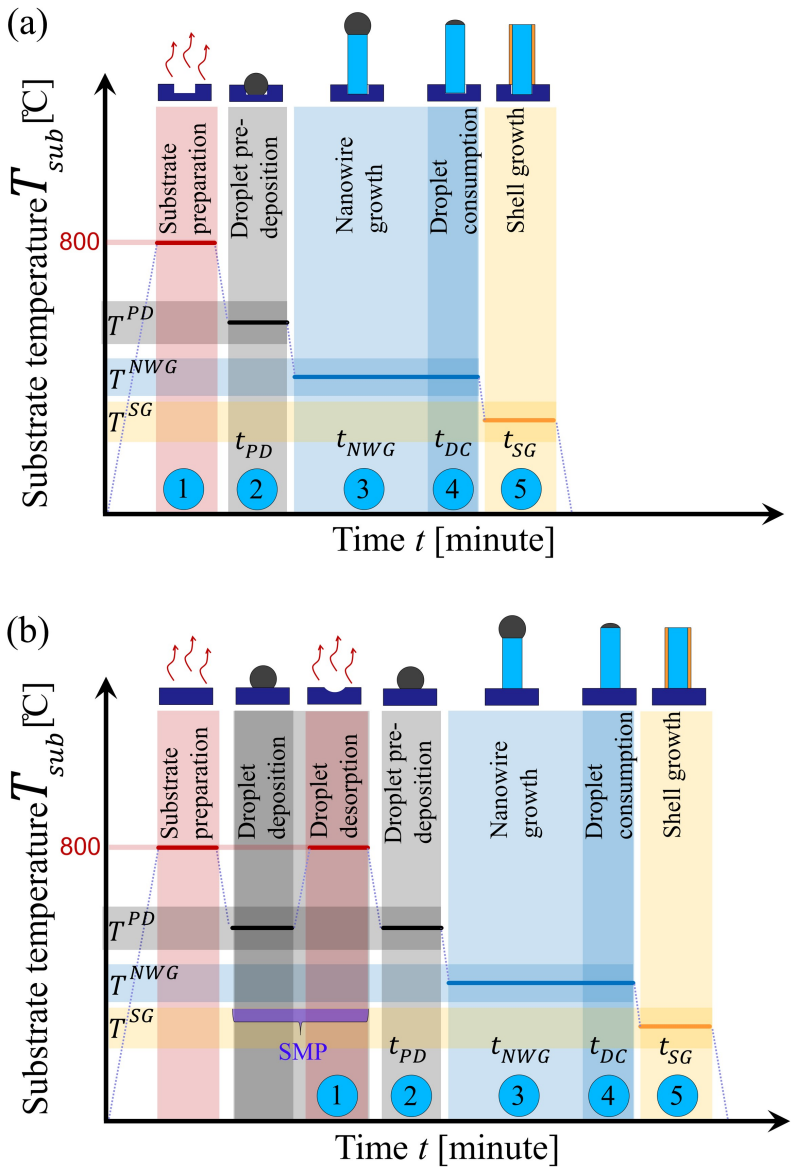

Figure 2.12: Nanowire samples preparation (growth protocol). (a) On silicon substrates coated with thermal oxide (thermal oxide substrate). (b) On silicon substrates coated with native oxide (native oxide substrate)

ratio of 3 and a growth rate of 0.12 ML/s for time $t^{NWG} = 30$, 45 and 60 minutes for the different samples in this study.

4. The droplets are consumed by supplying As while stopping Ga supply at $T^{DC} = T^{NWG}$ for 15 minutes then cooling down to the shell growth temperature T^{SG} for another 15 minutes (*i.e.* the total $t^{DC} = 30$ minutes).

5. For the shell growth, the substrate temperature and the material fluxes were adjusted to the desired parameters. The reduced substrate temperature $T^{SG} = 400°C – 500°C$ and the higher V/III ratio (V/III$\approx$ 4 – 6 reduce the diffusion length of the group III-materials favoring VS growth on the nanowire sidewalls. The shell growth time is $t^{SG} = 11$-30 minutes for the different studies in chapters 4 and 5.

The growth on native oxide substrates are the same listed steps but preceded by the surface modification procedure (SMP) explained in 2.1.1.

Patterned substrate layout

The Si substrates were covered by a 15-20 nm thick thermal oxide layer and patterned with nano-hole arrays defined by electron-beam lithography (EBL). These nano-holes act as nucleation sites for Ga catalyst droplets for the epitaxial nanowire growth. The pattern consists of several equidistant $100 \times 100\ \mu m^2$ large arrays (see figure 2.13(a)) of nano-holes arranged in a hexagonal grid as shown in figure 2.13(b). The separation between neighboring holes (pitch p) differs for each array, ranging from $p = 0.1\ \mu m$ to $p = 10\ \mu m$. These ensembles have different nanowire density and the layout of the substrate and can be navigated using X-ray diffraction microscopy. By setting the incident angle of the X-ray beam at the Bragg condition of GaAs, the substrate layout is defined by biaxial scanning along x and y of the lab geometry and the positions of all arrays can be defined with respect to the goniometer as shown in figure 2.13(b). Apart from the ensemble arrays, single nano-holes with 10 μm separation are drilled along a 1 mm straight line bordered by two etched markers to facilitate the illumination of a single nanowire as shown in figures 2.13(a) and 2.13(d). More details about EBL preparation of these samples can be found in [127]. As mentioned previously,

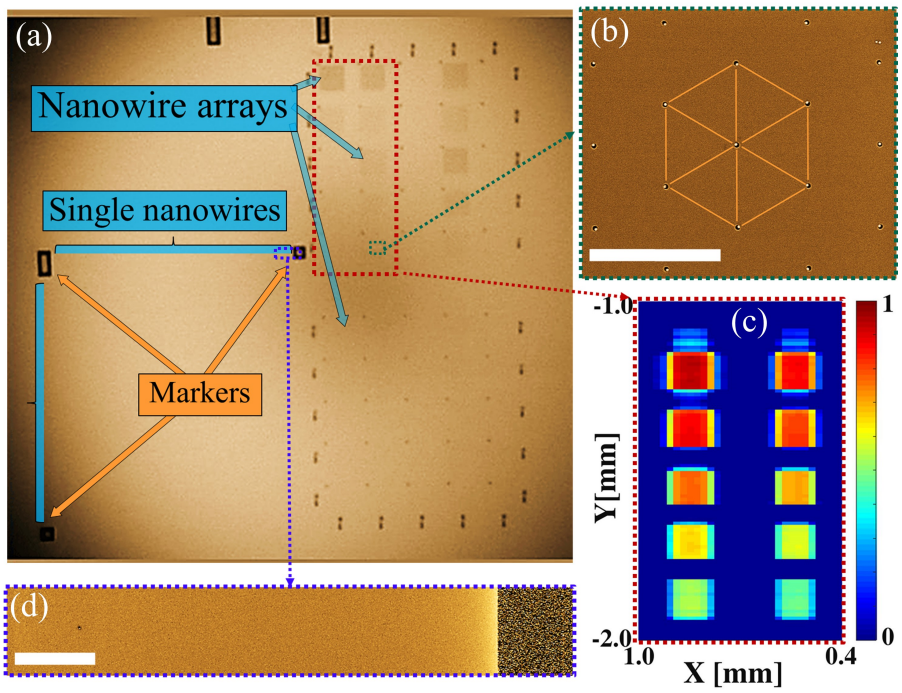

Figure 2.13: Patterned substrate layout (a) Overview SEM image of the substrate layout showing the nanowire arrays and the markers that border the single nanowires. (b) Top-view SEM image of one of the nano-hole arrays (with p =100 nm) and their hexagonal arrangement. (c) Scanning on the substrate surface by X-ray diffraction microscopy showing the nanowire arrays with different densities indicated by the variation of reflected X-rays that is proportional to the total crystalline volume of the grown nanowires. (d) single nano-hole drilled 10 μm away from the edge of an etched marker. Scale bars correspond to 1 μm.

the sample layout enables the navigation on the substrate during the XRD measurements facilitating access to nanowire arrays and single nanowires as we will see in the following chapters of this work. The recipe to find a single nanowire using this substrate layout can be found in [128].

Chapter 3

Flux shadowing and nanowire crystal structure (polytypism)

Abstract

In the following, we reveal the effect of Ga-flux shadowing on the evolution of nanowire crystal structure by means of time-resolved XRD during MBE growth of self-catalyzed GaAs nanowires grown on patterned Si(111). We investigate nanowires grown in arrays with pitches ranging from $p = 100\,\mathrm{nm}$ up to $p = 1000\,\mathrm{nm}$ located on the same wafer, thus ensuring identical global parameters for nanowire growth, and observe strong correlation of nanowire crystal structure and array pitch p. By our time-resolved experiment, we identify a point of time during growth, depending on the respective array pitch p, where the crystal structure suddenly starts to change, which we attribute to the onset of Ga-flux shadowing. We explain our observations by Ga-flux modeling considering specular reflection of Ga atoms and Ga-flux shadowing that causes a deflation of the liquid Ga-droplet, leading to the termination of nanowire axial growth in the extreme case, emphasizing the important role of the secondary reflected Ga-flux for patterned nanowire growth.

3.1 Epitaxial nanowire growth at different densities

The growth studied in this research follows the mentioned steps in 2.3.3 where droplets form at $T^{PD} = 630\,°C$ by depositing Ga with an equivalent GaAs thickness of 55 monolayers (ML) and V/III ratio for the nanowire growth of $F_{V/III} = 3$, 2D growth rate of 0.12 ML/s and $t^{NWG} = 30$, 92.5 and 45 min (sorted according to performed research). In this case we took special care, that the substrate is oriented in such a way, that the incoming Ga-flux is shadowed not by the nearest neighbor nanowire with distance p but by the second nearest neighbor with distance $\sqrt{3}\,p$.

As mentioned in 2.3.3, each array of the patterned substrate has a certain hole diameter d and a pitch size p. The influence of the hole diameter and pitch size on the formed Ga droplets can be seen in figure 3.1. For the nanoholes with diameter $d = 70$ and 90 nm, it can be seen that more than one droplet may nucleate in one hole due to the large collection area of Ga atoms within each hole (as shown in figure 3.1(a)). For the quantitative analysis of the droplet diameter at different arrays, we consider only the nano-holes that contain solo droplet. At different nano-holes densities, the SEM measurement reveal that the droplet size is independent of the pitch size p for consistent hole diameter d as shown in figure 3.1(b). On the other hand, at the same pitch size p, the droplets tend to have larger size at larger nano-hole diameter as shown in figure 3.1(c) for the case of nano-holes with pitch size $p = 400$ nm. This behavior can be attributed to the low sticking coefficient of Ga on the thermal oxide of the silicon substrate, which means that the contribution of Ga diffusion on the substrate surface to the nano-holes is negligible. Therefore, the Ga droplets are formed mainly by the direct impingement and the diffusion within the hole of the incident Ga flux. The functions in figures 3.1(b) and 3.1(b) imply identical conditions for the initial epitaxial growth of the nanowires for the arrays with the same nano-hole diameter. After the growth, the nanowires in arrays with $d = 40$, 70 and 90 nm and $p = 100$, 200, 400, 700, 1000, 1500, 2000, and 3000 nm are characterized by SEM. The number of investigated nanowires varies with the

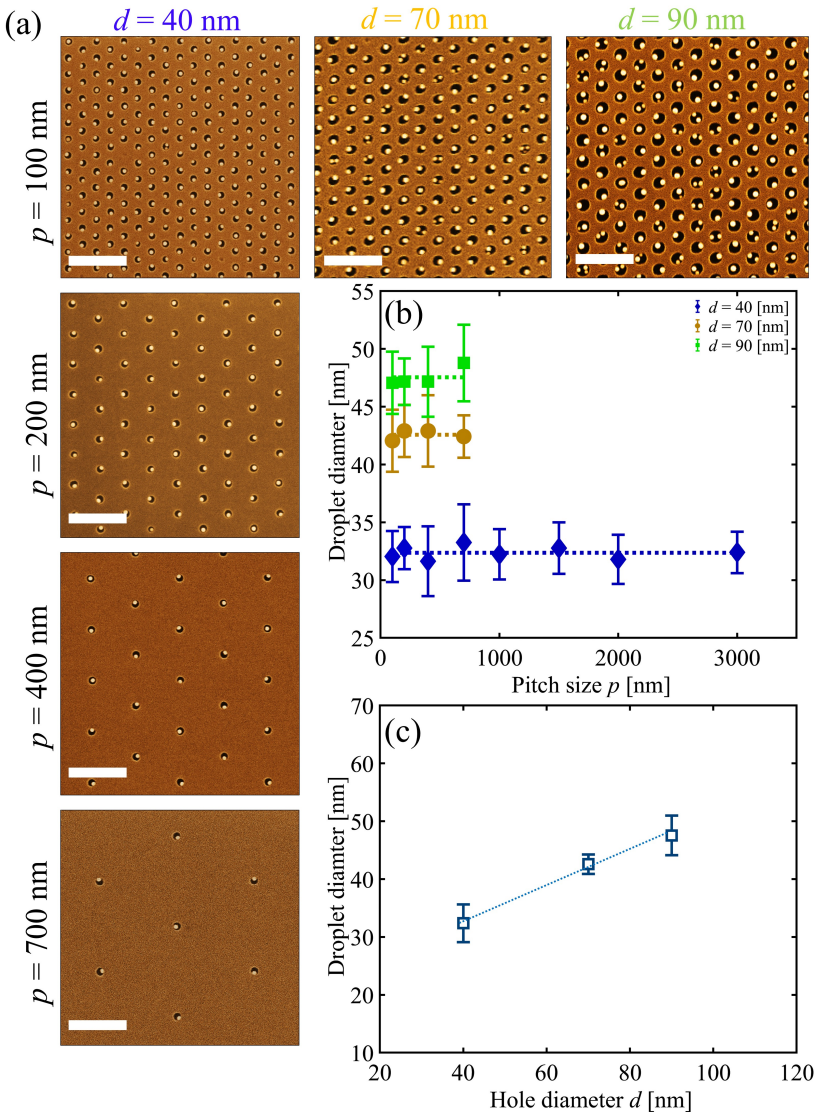

Figure 3.1: Droplet nucleation at different nano-hole arrays. (a) SEM images with top view of droplet nucleation at nano-hole arrays with p = 100, 200, 400 and 700 nm and d = 40, 70 and 90 nm. The scale bar corresponds to 500 nm. (p) The droplet diameter as function of p at different nano-hole diameter d. (c) Droplet diameter as function of nano-hole diameter d at the nanowire arrays with $p = 200$ nm.

pitch from 275 nanowires for p = 100 nm to 35 nanowires for p = 3000 nm. Overall, length and diameter of 845 nanowires are measured. Examplary SEM images of pitches with p = 100, 200, and 700 nm are shown in figure

3.2(a), evidencing the high vertical nanowire yield. The nanowire length l_{NW} as well as nanowire radius r_{NW} are shown in figure 3.2(b) and 3.2(c), respectively, in dependence on the pitch p for different hole diameters d. As mentioned previously, the site-occupancy in case of $d = 40\,\text{nm}$ is one and multiple nanowires in one hole are found for larger hole sizes. Only cases of one nanowire per hole were considered for the above evaluation, thus the large error-bars for $d = 70\,\text{nm}-90\,\text{nm}$. Both l_{NW} and r_{NW} show a significant dependence on p for $p \leq 400\,\text{nm}$. In case of $p \geq 700\,\text{nm}$, l_{NW} and r_{NW} seem to be independent of p. The observed dependency is typically attributed to a material flux shadowing that prominently occurs in dense nanowire arrays [21, 26, 46]. The nanowire shape is also affected by p. Whereas, the nanowires grown at $p = 100\,\text{nm}$ are quasi non-tapered, the nanowires gradually develop a slightly inverse-tapered shape as p increases. In addition, we find a large variety of droplet shapes and droplet wetting angles at $p = 100\,\text{nm}$. The nanowire arrays left of the dotted vertical line in figures 3.2(b) and 3.2(c) have been measured by XRD, whereas only SEM has been recorded for the arrays with $p \geq 1500\,\text{nm}$. Overall, the vertical nanowire yield for $d = 40\,\text{nm}$ is independent of p in our samples.

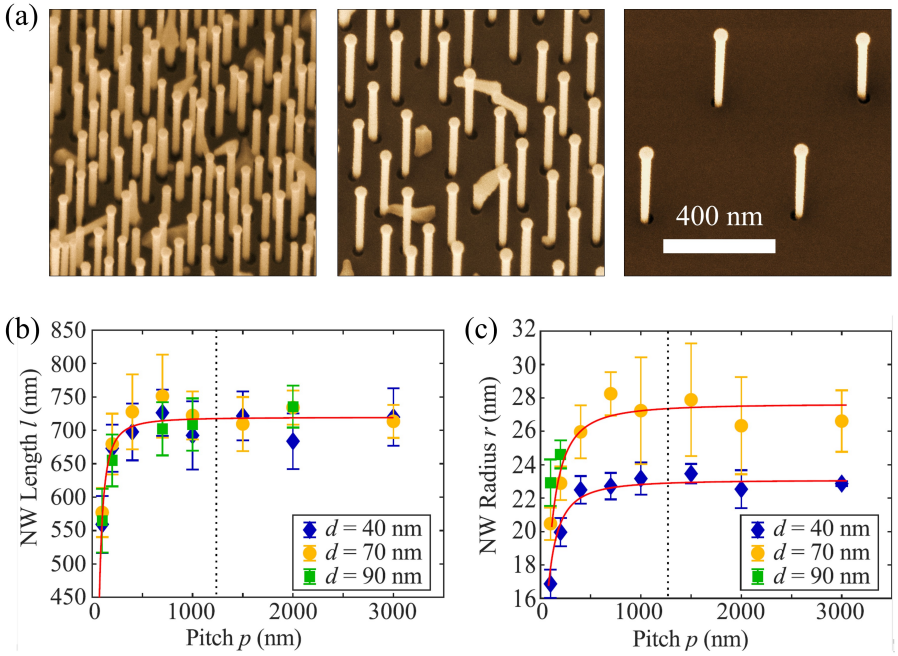

Figure 3.2: (a) SEM images with a viewing angle of 30° of nanowire arrays with $p = 100$, 200, and 700 nm. The scale bar is the same for all images. (b) The average nanowire length l_{NW} for arrays of pitch p as measured by SEM. (c) Average nanowire radius r_{NW} measured in the middle of the nanowire as function of array pitch p. The red lines serve as guide for the eyes.

3.2 Ex-situ XRD measurement of nanowires at different arrays

In order to characterize the crystal structure of the nanowires, we performed X-ray diffraction experiments at the Resonant Scattering and Diffraction beamline P09 [129] at PETRA III. We used a hexapod-mounted compound-refractive lens focusing setup in order to achieve an X-ray beam with a size of 2 µm (v) × 5 µm (h) at $E = 15$ keV photon energy. The X-ray spot-size provided by the focusing setup is small enough to illuminate nanowires of one individual array only, while being large enough to average over a meaningful number of nanowires in the respective array which is particularly important for the statistical significance of our results. In addition to *ex-situ* XRD, time-

resolved *in-situ* XRD is a non-destructive way of structure characterization during nanowire growth [41, 130–134], from which we can infer information on the evolution of crystal structure of the nanowire arrays at the various pitches p during growth, as will be shown later.

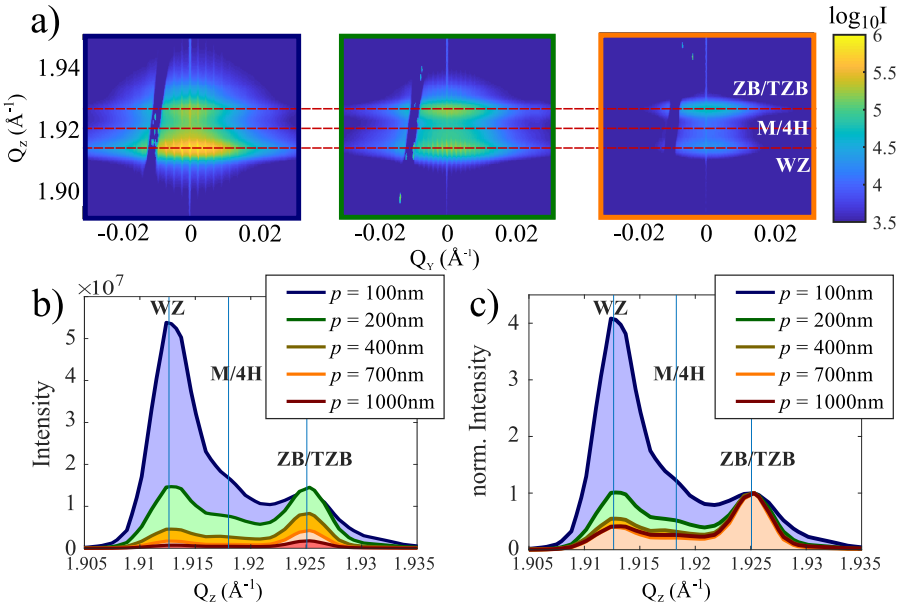

Figure 3.3: a) X-ray RSMs of the GaAs(111) Bragg reflection for nanowire arrays with $p = 100$, 200, and 700 nm. Signals from WZ, ZB, as well as the disordered M-phase (or 4H) are visible. Next to the CTR, SRs are observable for $p = 100$ nm and $p = 200$ nm, indicating high-quality lateral ordering of the GaAs nanowire array. b) q_z-intensity profiles through the GaAs(111) Bragg reflection. The reference positions $q_z(WZ)$, $q_z(M)$, and $q_z(ZB)$ are indicated by the vertical solid lines. c) For giving an impression of the WZ phase-fraction in the nanowires, the intensity profiles were normalized to ZB peak intensity.

For each array, we recorded the 3D distribution of scattered X-ray intensity - *ex-situ* - in vicinity of the symmetric Si(111) and GaAs(111) Bragg reflections, illustrated in reciprocal space maps (RSMs) as described in 2.3.1. Since the (111) lattice-plane spacing of cubic zinc-blende (ZB) GaAs and hexagonal wurtzite (WZ) GaAs differ [135,136], the scattering experiment is sensitive to the average stacking sequence of polytypic segments along the nanowire [111] growth axis [51, 132]. Moreover and due to the coherence properties of the

X-ray beam, next to the Si crystal-truncation rod (CTR) that arises from the truncation of the Si-crystal, the lateral periodicity p of the GaAs nanowires gives rise to so-called superstructure rods (SR) next to the GaAs(111) Bragg reflection. Representative results of these *ex-situ* XRD measurements (corresponding to the SEM images in figure 3.2(a) are illustrated in figure 3.3(a). The theoretical reference scattering values of the (111) Bragg reflection for ZB GaAs is $Q_z(ZB) = 1.9251\text{Å}^{-1}$, whereas WZ with its about 0.65 % larger lattice-plane spacing is located at $Q_z(WZ) = 1.9126\text{Å}^{-1}$. It is worth to note, that the locations of the respective Bragg reflections for WZ and ZB GaAs in experimental profiles strongly depend on actual phase purity and phase fraction [132, 137]. In addition to that, presence of higher-order polytypism (4H, or M-phase [138]) may give rise to additional Bragg peaks located between the ZB and WZ Bragg peaks, corresponding to their respective hexagonality. Intensity profiles along Q_z are shown in figure 3.3(b). It is evident, that the strongest signal arises from the most densely grown array with $p = 100\,\text{nm}$. As the pitch increases, the number of illuminated nanowires decreases and so does the overall intensity of the scattering signal. If we consider the intensity distribution within a single RSM however, an interesting observation can be made. It is obvious, that the strongest feature in the RSM of the array with $p = 100\,\text{nm}$ is actually the WZ (00.2) Bragg reflection, indicating a dominance of WZ over ZB segments in the crystal structure of the GaAs nanowires. This is remarkable, since the crystal structure of self-catalyzed GaAs nanowires is commonly ZB dominated [139, 140] and a result of the pronounced equilibrium wetting angles $\varphi >> 90°$ as explained in 2.2.2. In contrast to that, we evidence here that self-catalyzed GaAs nanowires in predominantly WZ phase can be synthesized as well. As p increases further, the intensity of the WZ signal decreases, until ZB becomes the most intense feature of the RSM. In order to better illustrate this behavior, the integrated intensity was normalized to the ZB peak intensity (figure 3.3(c)). For $p = 100\,\text{nm}$, the WZ peak intensity exceeds the ZB peak intensity by a factor of 4. But already for a nanowire spacing of $p = 200\,\text{nm}$ ZB and WZ signals are equally intense. For $p \geq 400\,\text{nm}$ the ZB GaAs peak is the strongest signal of the scattering profile. Interestingly, the shapes of the normalized

profiles of $p = 700\,\text{nm}$ and $p = 1000\,\text{nm}$ (figure 3.3(c)) are essentially identical, which is indicative for equal average polytype phase fraction and phase purity, and points toward identical growth conditions for these nanowires. This reflects well the saturation of nanowire axial and radial growth rates in figures 3.2(b) and 3.2(c). At the same time, a photoluminiscence study of Rudolph *et al.* [44] of a few individual patterned GaAs nanowires implies a relation of array pitch p and crystal structure as well, where the authors observe a larger number of twin-related defects (*i.e.* ZB/TZB) for larger values of p, although they do not clearly distinguish these from WZ inclusions. However, in a previous ensemble investigations on non-patterned self-catalyzed nanowires on Si(111) a similar trend of the nanowire mean crystal structure with the nanowire mean area density as presented here was observed [51]. Still the question remains, which exact processes during growth are responsible for the evolution of the differences of nanowire crystal structure in the arrays with $p \leq 400\,\text{nm}$. In order to identify the material shadowing effect at different nanowire densities, we performed time-resolved *in-situ* XRD investigation the nanowires during growth.

3.3 In-situ XRD measurement of nanowire arrays during growth

In addition to the above *ex-situ* XRD experiment after nanowire growth, we performed *in-situ* XRD during MBE growth of a second sample using the portable MBE described in 2.3.2. Again, we benefit from the layout of the pattern, that allows for sequential monitoring the nanowire growth in different arrays by moving one array after the other into the micrometer-sized X-ray beam, in an iterative procedure. In contrast to recording full 3D RSM as for the *ex-situ* study, we restrict the *in-situ* measurements to fast 2D cuts of the reciprocal space close to the GaAs(111) Bragg reflection. This way, we achieve an effective time-resolution of 1 min per array. We used similar growth parameters as above for the *in-situ* growth experiment, but extended the growth time to $t^{NWG} = 92\,\text{min}$.

The basic idea behind the *in-situ* experiment is simple: if the material shadowing depends on p, the onset of the material shadowing effect and its consequences for crystal structure evolution should appear for each p at different nanowire lengths l_{NW} and thus at different growth times t^{NWG}. Since we have already observed these consequences for the sample grown for $t^{NWG} = 30\,\text{min}$, and for arrays with $p \leq 400\,\text{nm}$, we should expect the onset of shadowing happening at these arrays first. In addition, the saturation of l_{NW}, r_{NW} (figures 3.2(b) and 3.2(c)), and the identical normalized Q_z-intensity profiles (figure 3.3(c)) after the same pitch value $p \geq 700\,\text{nm}$ imply that shadowing effects did not play a role for the growth of the nanowires in these arrays, at least within $t^{NWG} = 30\,\text{min}$.

However, before we discuss the *in-situ* X-ray results, let us first have a look at the length distribution of the *in-situ* sample as extracted from SEM images. In figure 3.4(a) we observe a non-trivial, quasi bi-modal length-distribution for the nanowires grown in the arrays with $p \leq 400\,\text{nm}$. Based on the axial growth rates extracted from figure 3.2(b), we would expect the nanowires to have pitch-dependent lengths l^{p}_{NW}: $l^{100nm}_{NW} = 1700\,\text{nm}$, $l^{200nm}_{NW} = 2025\,\text{nm}$, $l^{400nm}_{NW} = 2160\,\text{nm}$, $l^{700nm}_{NW} \approx l^{1000nm}_{NW} = 2260\,\text{nm}$ after a growth time of $t^{NWG} = 92\,\text{min}$. These values correspond to the upper group of the nanowire length-distribution indicated by black arrows, present for all pitches. The lower group (indicated by the red arrows) is only present for $p \leq 400\,\text{nm}$. From the SEM images in figure 3.4(b), it is evident that the *in-situ* sample exhibits inhomogenous growth. We explain the length-distribution by shadowing of one group of most likely clustered nanowires which must have stopped the axial elongation at some point during growth, and another group of nanowires that were not shadowed, and continued their axial elongation with the respective axial growth rate resulting in $l^{p}_{NW}(92\,\text{min})$. Moreover, the nanowires of these two groups seem to have differently shaped Ga-droplets at their tip. Whereas the long nanowires show pronounced Ga-droplets, the short nanowires seem to have small crystalline caps, or shallow droplets (if any) at their tip, which supports our assumption, that the axial growth of the short nanowires was terminated at $t^{NWG} < 92\,\text{min}$ during growth. Regarding the *in-situ* X-ray data, we ex-

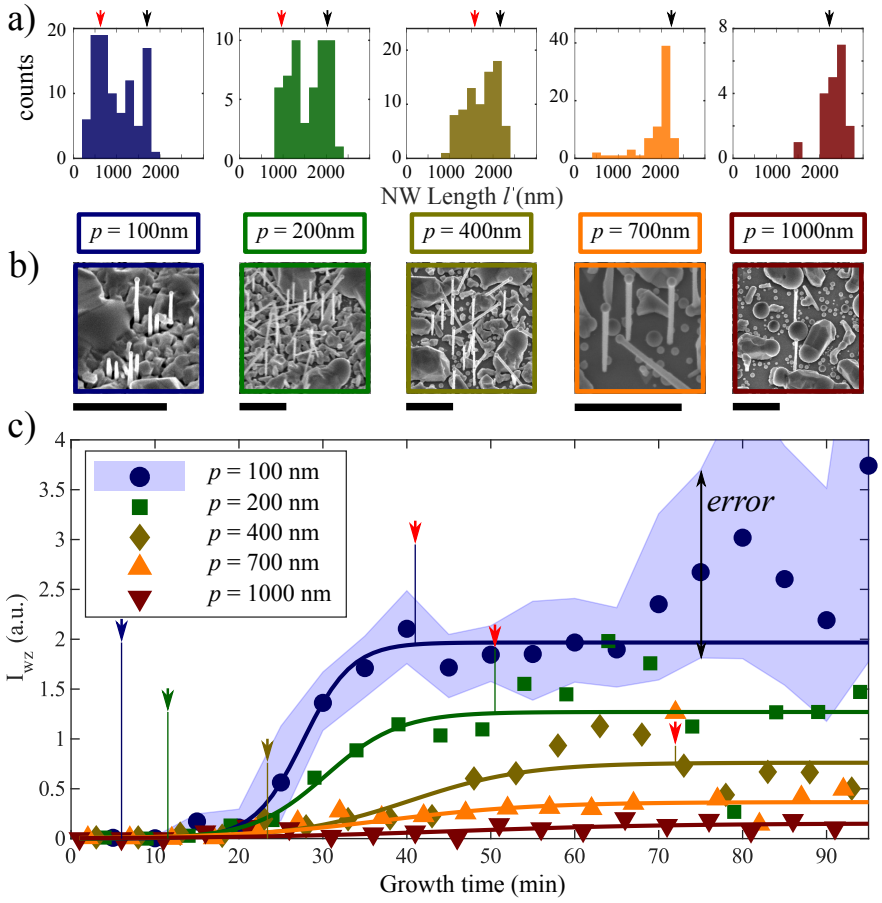

Figure 3.4: (a) nanowire length distribution for the various arrays of the *in-situ* sample after $t^{NWG} = 92\,\text{min}$ of growth. Black arrows indicate expected nanowire length using growth rates derived from figure 3.2(b), red arrows given by fit displayed in figure 3.4(c). (b) Corresponding SEM images, demonstrating the inhomogeneous growth. Scale bar corresponds to $5\mu m$. (c) Time-evolution of the integrated WZ intensity during growth. The solid line represents a fit to the data, the shaded area gives an impression of the error-range. The colored arrows indicate the onset of shadowing at $l_{NW} + h_{drop} > l_c$ according to the model, red arrows indicate $I^p_{WZ}(t^p_f) = 0.99 \cdot A$ as obtained by the fit.

clusively focus on the time-evolution of the (00.2) WZ Bragg reflection. We assume that the considerable parasitic growth on the substrate surface between the nanowires visible in figure 3.4(b) essentially crystallizes in the ZB phase [135]. The WZ phase however, is indicative for nanowire growth at Ga-

droplet wetting angles $\varphi \approx 90°$. Self-catalyzed GaAs nanowires commonly show WZ insets especially at the bottom and the tip (formed during the initial stages and the final stages of growth respectively). The WZ segments below the droplet are commonly formed under residual As background after the Ga-flux supply was stopped, or during intentional droplet consumption, causing a shrinkage of the Ga-droplet and concomitant reduction of φ as discussed in 2.1.1 and 2.2.2. Our results are shown in figure 3.4(c): each datapoint corresponds to the area below the WZ peak (determined by a Gaussian fit to the WZ signal in the Q_z-intensity profiles such as shown in figure 3.3(b) at a certain time of growth t^{NWG}. It is evident, that the overall WZ intensity inversely scales with p. Most interesting however, is the pronounced 'step'-like behavior of the WZ intensity, in particular for the nanowires grown in the three arrays with $p \leq 400\,\mathrm{nm}$, which implies a drastic increase of WZ growth after a certain time t_i^p and then a halt of WZ growth after a certain time t_f^p. We note, that these times seem to differ for the nanowires grown in different arrays. After t_f^p, the WZ intensity I_{WZ}^p seems to be stable, within the error margins. The solid line is a fit to the data using a Fermi-function

$$I_{WZ}^p(t_g) = A \cdot \Big(1 - \frac{1}{e^{(t_g - t_h)/f_w} + 1}\Big). \tag{3.1}$$

where A is the amplitude, t_h is the time where $I_{WZ}^p(t_h) = 0.5 \cdot A$, and f_w is the width or abruptness of the 'step'. The choice of the Fermi-function is not motivated by physical considerations, but seems to be suitable for an empirical description of our results. The red arrows in figure 3.4(c) indicate $I_{WZ}^p(t_f^p) = 0.99 \cdot A$, which we consider to correspond to the end of axial nanowire growth at t_f^p resulting in the group of short nanowires. The corresponding nanowire length $l_{NW}^p(t_f^p)$ determined the actual position of the red arrows in figure 3.4(a). In case of $p = 700\,\mathrm{nm}$, and $p = 1000\,\mathrm{nm}$, the length $l_{NW}^p(t_f^p)$ would exceed $l_{NW}^p(t^NWG)$, and is not shown. For the three arrays $p \leq 400\,\mathrm{nm}$ however, the length deduced from the fit of the time resolved X-ray data $l_{NW}^p(t_f^p)$ is in good agreement with the lengths of the group of short nanowires obtained from SEM. Summarizing, we found evidence for our hypothesis, that the axial growth of the group of shorter nanowires was

terminated during growth. We interpret the increase of WZ intensity as a consequence of WZ growth below the Ga-droplet while the Ga-droplet shrinks and reduces its wetting angle. Obviously, the Ga-droplet disappeared which caused termination of the axial nanowire growth and the saturation of the WZ intensity. Since any volume change of the Ga-droplet is a consequence of an imbalance of the Ga-fluxes in and out of the droplet, we consider a change of the Ga-flux into the droplet as a likely reason for our observations.

3.4 Modeling Ga-flux shadowing

We now propose a model for Ga-flux shadowing based on the following assumptions. As reported by Oehler *et al.* [26], the interaction of Ga adatoms with the thick thermal SiO_x is very weak, therefore their re-evaporation can be approximated by a specular reflection from the surface. This allows dividing the Ga-flux into two contributions: (1) The nanowire can collect Ga via direct impingement from the Ga-source, and (2) via reflection of Ga from the surface. In order to contribute to the nanowire growth, the Ga atoms need to hit either the nanowire side wall or directly the Ga droplet. These two pathways are expressed by an effective collection area for Ga, which consists of the nanowire cross-section $\int_0^{l_c} r_{NW}(x)\mathrm{d}x$ (where the collection length l_c is the length of the nanowire receiving Ga-flux and $r_{NW}(x)$ the radius of the nanowire depending on the distance x from the Ga droplet at the top of the nanowire) and a circular droplet cross-section $\pi\, r_{drop}^2$. As shown schematically in figure 3.5(a),- c, the collection length l_c is affected by shadowing. For Ga-adatoms impinging on the nanowire side wall, their probability to reach the Ga-droplet at the top of the nanowire decreases exponentially as $P_{Ga} = e^{-\frac{x}{\lambda}}$ with a diffusion length of Ga on the nanowire facet $\lambda = 1200\,\mathrm{nm}$ [40]. In our MBE system the Ga-flux impinges under an angle of θ =28° with respect to the sample normal as illustrated in figure 2.11(c). The in-surface-plane angle of $\phi = 30°$ was chosen to promote shadowing of second nearest neighbor nanowires in the hexagonal array spaced by $\sqrt{3}\,p$, as illustrated in figure 3.5(a). The collection length l_c, and the direct as well as reflected Ga-fluxes

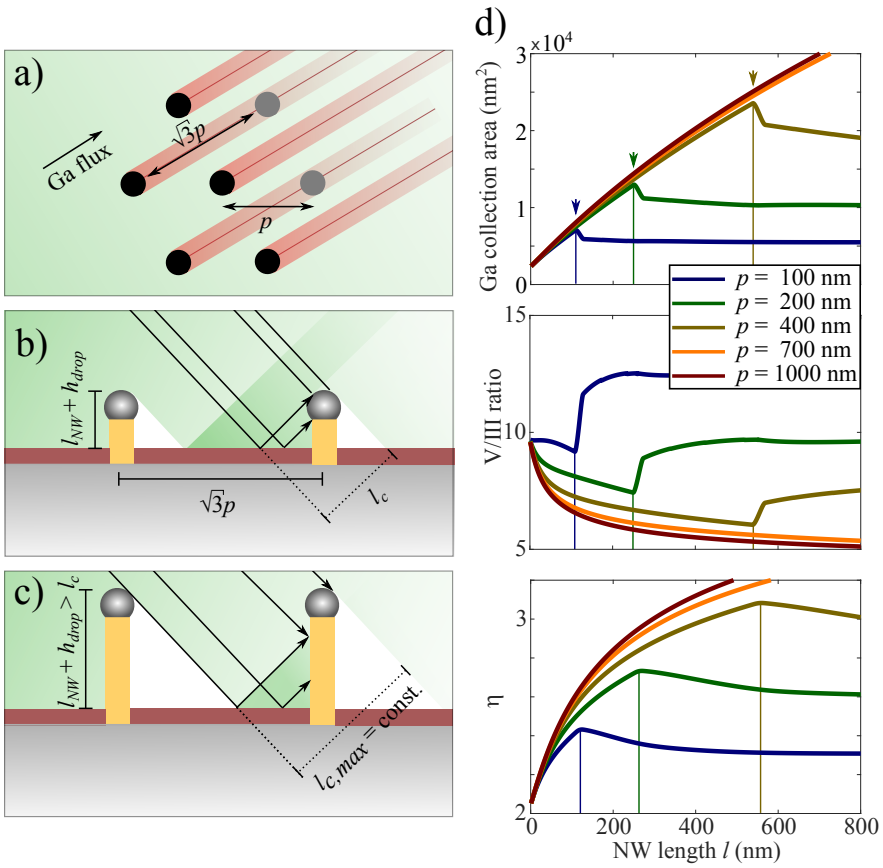

Figure 3.5: Ga-flux shadowing model: (a) Top-view of hexagonal nanowire array. (b) Side-view for early growth stage, no shadowing. The collection length l_c is constituted of a collection length projected on the substrate surface which reflects the Ga-flux onto the nanowire, and the collection length of the nanowire itself. During nanowire growth, l_c increases. (c) The length of the nanowire exceeds the value l_s at which shadowing of the reflected flux begins. It can be seen, that the reflected flux into the Ga droplet is shadowed first. l_c is constant, because the collection length on the nanowire side wall increases with the same rate as the collection length on the surface is shadowed. (d) Ga collection area resulting from all contributions, V/III ratio and droplet shape η in dependence on the nanowire length. Arrows indicate the onset of shadowing for different pitches.

are shown in figure 3.5(b) for the case of small l_{NW} where no shadowing is occurring yet. As the nanowire increases in length, l_c increases by two components: the length at the surface from which reflected Ga atoms can

hit the nanowire, and by the nanowire length itself. In figure 3.5(c), the nanowires have reached such a length that the cast shadow covers more than half the distance to the second nearest neighbor nanowire. In this regime, l_c does not change anymore, since the contribution of reflected Ga-atoms decreases at the same rate, as the contribution of directly impinging material increases (given that both nanowires have the same axial growth rate). As nicely illustrated by this schematic, the reflected Ga-flux into the Ga-droplet is shadowed first. When the surface between the nanowires is completely shadowed, no Ga-flux is reflected anymore and the nanowire can collect Ga only via direct impingement.

At the same time, the volatile As is considered to form a homogeneous background pressure. Therefore the collection area of the droplet is that of a spherical cap with an area $A_{cap} = \pi \left(r_{NW}^2 + h_{drop}^2\right)$, where h_{drop} is the height of the Ga-droplet. Additionally, it has been reported [79] that the As background pressure is increased for the case of nanowire arrays by a factor of $B \approx 2.1$, which is attributed to an As re-evaporation from the nanowire facets. We consider this factor to play a role only at a later stage of nanowire growth, where the nanowire length is in the order of the nanowire pitch. Therefore, we described it as a bounded growth following the relation $B(l) = S - (S - B_0)\, e^{-p \cdot l_{NW}}$, with the factors $S = 2.1$, $B_0 = 1$, the pitch p and the length of the nanowire l_{NW}.

During growth of the nanowire, changes in the droplet shape $\eta = h_{drop}/r_{NW}$ and the nanowire radius at the growth front $r_{NW}(x = 0)$ can be described according to Tersoff *et al.* [141] by

$$\mathrm{d}\eta = \frac{2}{1+\eta^2}\frac{\Omega_L}{\Omega_x}\frac{1}{\rho}\left[\frac{F_3}{F_5}\left(1 + \frac{1}{(1+\eta^2)\rho}\right) - 1\right]\mathrm{d}\xi \tag{3.2}$$

and

$$\mathrm{d}r = \frac{2}{\eta(1+\eta^2)}\frac{\Omega_L}{\Omega_x}\left[\frac{F_3}{F_5}\left(1 + \frac{\lambda}{(1+\eta^2)r_{NW}}\right) - 1\right]\mathrm{d}\xi. \tag{3.3}$$

Here, we use $\Omega_L/\Omega_x \approx 0.42$ with Ω_L the volume per atom in the liquid, Ω_x the volume per two-atom unit of the III-V crystal, F_3 and F_5 the fluxes of the group III and the group V element, $\rho = r_{NW}/\lambda$, and $\xi = x/\lambda$. It can be

seen that both η and r_{NW} will respond according to changes of the fluxes F_3 and F_5.

The resulting collection area for Ga ($d = 40\,\mathrm{nm}$) and its impact on both the V/III ratio and the droplet shape η are displayed in figure 3.5(d). An approximate droplet radius $r_{drop}(0) = 15\,\mathrm{nm}$ as determined by SEM from a dedicated sample (see figure 3.1) was used as a starting value for both droplet and nanowire radius. It becomes apparent, that the Ga collection area shows a sudden drop at a certain nanowire length corresponding to the shadowing of the reflected flux into the Ga-droplet. The sudden drop in Ga-flux for the different pitches (indicated by arrows) is located at $l_{NW} + h_{drop} > l_c$ and represent the theoretical value for the onset of Ga-flux shadowing in the respective array. Since this shadowing does not occur for the As flux, this corresponds to a jump of the V/III ratio to a much higher value. Caused by the relations expressed by equations 3.2 and 3.3, this leads to a shrinkage of the Ga-droplet (η decreases) and during this shrinkage WZ formation is favored. Subsequently to the sudden drop, the Ga collection area further decreases at a lower rate due to shadowing of the reflected Ga-flux onto the nanowire side wall and because of the decreasing size of the Ga-droplet. The times t^{NWG} corresponding to the predicted onset of shadowing during growth of our *in-situ* sample are shown by the arrows (blue, green and gold) in Figure 3.4(c). In agreement with our model, we observe the steep increase in the formation of WZ shortly after the respective theoretical onset of shadowing. Within our model, the effect of the shadowing on the size of the droplet is not as pronounced as it would be expected to achieve the complete consumption of the Ga-droplets as seen by SEM. This could be attributed to additional amplification factors which are not considered by model description: (1) Referring again to Tersoff *et al.* [141], also the growth speed depends on the droplet shape η, following the relation $v = \Omega_x\ (1 + \eta^2)\ F_5$. This means that as soon as a nanowire is shadowed, it will grow slower and will be shadowed even more, leading to a further reduction of l_c and therefore to a much stronger shrinkage of the Ga-droplet. In general, this might occur due to the small fluctuations in the length of different nanowires. For arrays, this will always be the case because the nanowires at the edge of the array

do not experience any shadowing. In case of our *in-situ* sample, this effect is further enhanced due to the inhomogeneous growth of nanowires (as seen from broad length distribution shown in figure3.4(a). (2) Besides that, the contributions to the Ga-flux within our model consists of two equal parts – direct and reflected flux – assuming a fully specular reflection of the Ga-adatoms. However, it is more likely that the re-evaporation does not happen under such idealized conditions. As it was also shown by Oehler *et al.* [26], a more uniform angular distribution of re-evaporated Ga-adatoms will lead to a stronger contribution of the reflected flux stemming from other places on the substrate. Since these contributions are subjected to shadowing effects as well, this will further increase the V/III-ratio and also contribute to a stronger shrinkage of the Ga-droplet. Ast is can be seen in figure 3.6(a) for nanowire grown for 5 minutes and 3.6(a) for nanowires grown for 45 minutes, the side-view SEM images confirm the higher variation of l_{NW} for the arrays with $p < 700$ nm (as well as the droplet size) where the shadowing take place. In this figure we consider the adjacent nanowires within the focal length of the microscope.

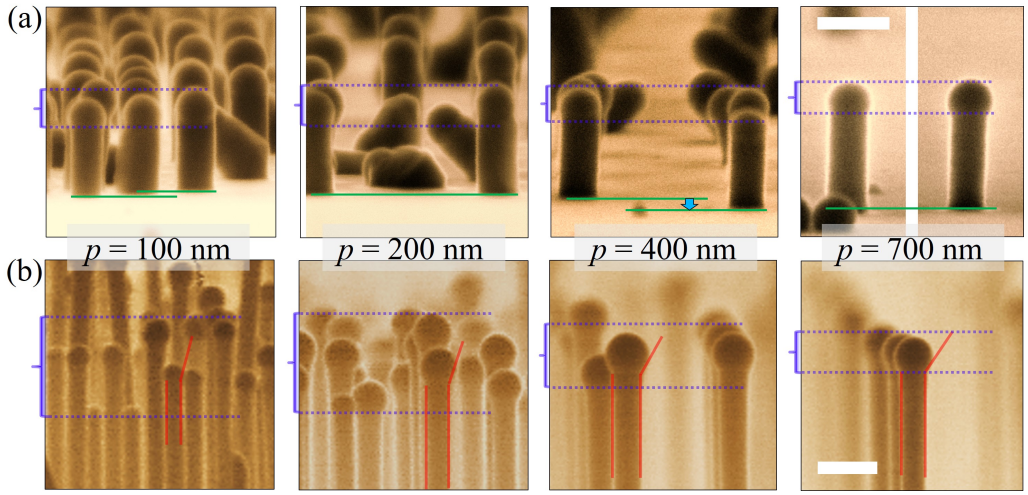

Figure 3.6: Side-view SEM images of the nanowires at (a) $t_{NWG} = 5$ min and (b) $t_{NWG} = 45$ min shows the changes of the variation of nanowire length and droplet size before and after nanowire shadowing at different nanowire arrays.

Finally, the consequences of shadowing in our case may be more pronounced as compared to growth under substrate rotation, as we promote shadowing by our choice of array orientation with respect to the impinging Ga-flux. This choice however, allows us to pinpoint the exact time during growth where shadowing becomes relevant. Our findings support the detailed shadowing model of Oehler *et al.* [26], mainly considering specular reflection of the Ga-flux, and constitute the first direct experimental study revealing the impact of the shadowing effect in self-catalyzed GaAs nanowire arrays on their crystal structure. We observed an extreme case of the shadowing effect manifested in the termination of the nanowire axial growth in our *in-situ* experiment, which emphasizes the importance of the secondary reflected Ga-flux for patterned nanowire growth. If the axial growth could be sustained further, is most likely a question of the optimization of growth conditions *during* the growth in order to remedy shadowing effects. Our study provides an approach how the detrimental effects of Ga-flux shadowing could be compensated, but moreover shows a way towards a targeted use of the shadowing of the group III material flux. Therefore certain arrangements between array and impinging fluxes could be chosen, by stopping substrate rotation during growth. Such arrangements may open up new design capabilities for partial or asymmetric core-shell heterostructures [142], since by an adept choice of array pitch and nanowire length, a heteroepitaxial shell could be deposited only onto the upper part of certain facets of the nanowire as will show later in this work. In addition, by changing the in-plane angle of the substrate, the shadowing-effect could be varied, selecting shadowing caused by nearest neighbor or second nearest neighbor nanowires. Although our observations were made on GaAs nanowire, our findings should as well be valid for VLS grown III-V nanowires in general, such as GaP nanowire for example.

3.5 Summery of chapter 3

We demonstrated that shadowing of the Ga-flux is affecting the evolution of nanowire crystal structure and thus plays a crucial role in the growth of regular GaAs nanowire arrays. In our case we found the WZ crystal structure to be the dominant phase in dense nanowire arrays, whereas for low density arrays ZB is the general crystal phase. Our experimental results and simulations reveal the origin of the pitch dependence of the crystal structure, allow to pinpoint the onset of Ga-flux shadowing, and support the assumption of specular reflection of the Ga-flux. This work moreover emphasizes the importance of the secondary reflected Ga-flux for experimental and theoretical aspects of patterned nanowire growth, and offers approaches to utilize shadowing-effects for the design of novel nanowire hetero-structures.

Chapter 4

In-situ analysis of strain and bending evolution of core-shell nanowires

Abstract

Misfit strain in core-shell nanowires can be elastically released by nanowire bending in case of asymmetric shell growth around the nanowire core. In this work, we investigate the bending of GaAs nanowires during the asymmetric overgrowth by an $In_xGa_{1-x}As$ shell caused by avoiding substrate rotation. We observe that the nanowire bending direction depends on the nature of the substrate's oxide layer, demonstrated by Si substrates covered by native and thermal oxide layers. Further, we follow the bending evolution by time-resolved *in-situ* X-ray diffraction measurements during the deposition of the asymmetric shell. The XRD measurements give insight into the temporal development of the strain as well as the bending evolution in the core-shell nanowire.

4.1 Experimental methods

4.1.1 Samples preparation and properties

The GaAs nanowire (core) templates were grown on n-doped Si(111) substrates covered with thermal and native oxide following the substrate sample preparation and the growth protocol explained in 2.3.3. We investigated five samples in this study as listed in table 4.1 where the mean nanowire length (l_{NW}) obtained by SEM measurements of reference GaAs nanowire samples grown under identical growth conditions of the templates of the studied samples. Additionally, the In concentration listed in table 4.1 were approximated from the calibration method of the MBE effusion cells. (the samples are numbered according to the performed study).

Table 4.1: List of the investigated samples and the main properties required for this research.

Sample	Oxide type	Experimental technique	Nanowire length(nm)	Shell growth time (minute)	In content (%)
Sample 1	Native oxide	SEM	1800	30	30
Sample 2	Thermal oxide	SEM	1800	30	30
Sample 3	Native oxide	XRD+SEM	1200	20	15
Sample 4	Thermal oxide	XRD+SEM	1200	20	15
Sample 5	Thermal oxide	XRD+SEM	1200	11	15

In figure 4.1, SEM images recorded with 30° tilt-view and top-view of the studied nanowire samples listed in table 4.1. In samples 2, 4 and 5 GaAs nanowire templates are prepared on Si substrates with patterned thermal oxide. The substrate properties and the pattern layout were discussed and explained in 2.3.3. We focus in this study on the arrays with pitch size $p =$ 1000 nm to avoid any impact of flux shadowing for samples 2 and 4 (see figures 4.1(c),4.1(d),4.1(g) and 4.1(h)). For sample 5 we focus our study on the single nanowire that is shown in figures 4.1(i)-4.1(l).
The growth of the GaAs nanowires proceeded for $t^{NWG} = 45$ minutes for samples 1 and 2 and 30 minutes for samples 3, 4 and 5 resulting in different mean nanowire lengths (l_{NW})(see table 4.1).

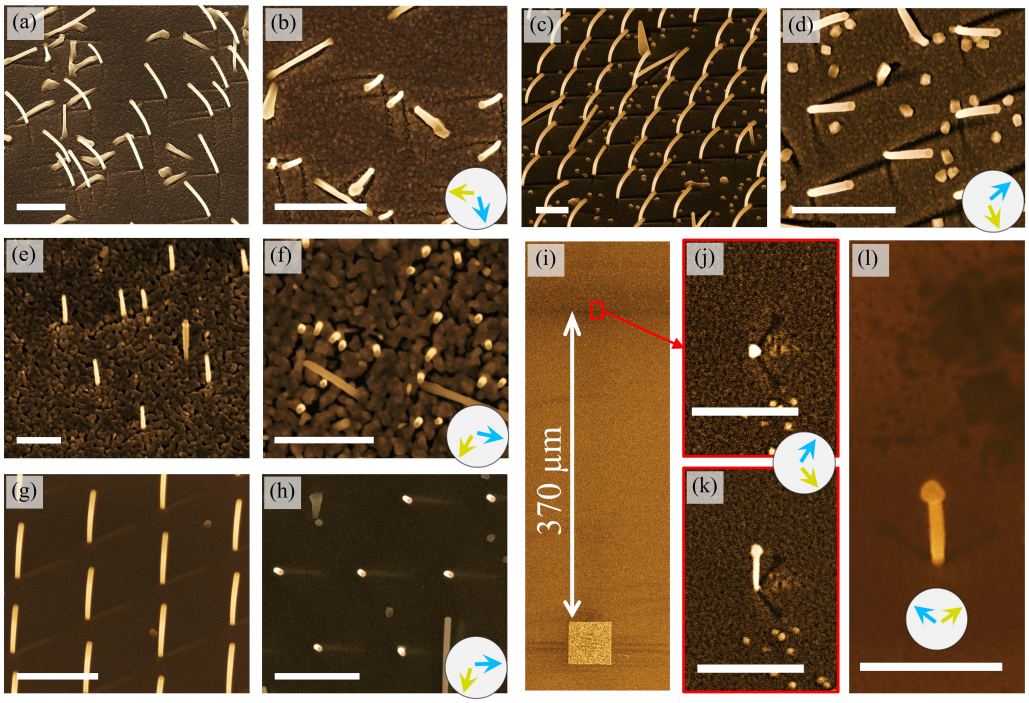

Figure 4.1: (a)-(h) SEM images of the studied samples with top-view and 30° tilt-view. (i) Top-view SEM image of sample 5 shows a reference marker and the position of the measured single nanowire. (j) Top view SEM images of the measured single nanowire. (k) and (l) 30° tilt-view from two different directions of the measured single nanowire. The arrows indicate the direction of Ga flux (blue) and As flux (yellow). All scale bars correspond to 1 μm.

To initiate the VS shell growth for all samples, first the Ga droplets at the nanowire apex were consumed to prevent any further axial VLS-growth. In the case of self-catalyzed GaAs nanowires, this is done by terminating the Ga supply while continuously supplying As at growth temperature. Afterwards, the substrate temperature and the material fluxes were adjusted to the desired parameters. The reduced substrate temperature T^{SG} = 400°C for samples 1-4 and 500°C for sample 5 and the V/III ratio (V/III≈6 (for samples 1-4) - 4 (for sample 5)) was chosen to reduce the diffusion length of the group-III materials favoring VS growth on the nanowire sidewalls.
The shell growth rate was chosen to be 0.04 ML/s which is equivalent to 0.8 nm/min for samples 1-4 and 0.25 ML/s (0.5 nm/min) for sample 5. The

shell growth time was 30 minutes for samples 1 and 2, 20 minutes for sample 3, 25 minutes for sample 4 and 11 minutes for sample 5. The resulting shell thicknesses are approximated by SEM inspection, where the shell thickness was evaluated in addition to the calibration method by comparing the final nanowire diameter with the GaAs nanowire diameter of respective reference samples.

4.1.2 X-ray diffraction from bent nanowires

XRD serves as an ideal technique to investigate nanowire bending due to its high sensitivity to small changes in the crystal structure and orientation whereas these changes are indicated by the changes of the diffraction signal profile. Therefore, *in-situ* XRD measurements were performed on GaAs nanowires during $In_{0.15}Ga_{0.85}As$ shell growth. The experiments were carried out at the German Electron Synchrotron (DESY-Hamburg). The *in-situ* XRD measurements on sample 2 and sample 5 were performed at the Resonant Scattering and Diffraction beamline P09 [143] whereas the XRD measurements on the nanowire arrays of sample 4 were performed at the *In-situ* and Nano-X-ray diffraction beamline P23 [144]. Both beamlines are equipped with a heavy load goniometer which can withstand the weight of the pMBE. The beam was focused to a spot size of few microns (1.5 μm horizontal $\times$ 5 μm vertical) by means of compound refractive lenses which is essential to illuminate only the desired regions on the substrate. During all *in-situ* XRD experiments, 2D pixel detectors were used for recording the diffracted signals. We measured reciprocal space maps (RSMs) in the vicinity of the GaAs(111) Bragg reflection in order to identify the bending direction in addition to measuring the nanowire bending angle (thus nanowire curvature) and the axial strain induced by the lattice-mismatched shell. Choosing a beam energy of 15 keV, the incident and scattering angles of the X-ray beam for the GaAs(111) Bragg reflection are 7.27° and 14.54°, respectively. These values are smaller than the maximum opening angle defined by the size of pMBE beryllium windows.
For samples 2 and 4, the shell growth and the XRD measurements were done

in multiple cycles. At the end of each shell growth run, a RSM of the full 3D GaAs(111) Bragg reflection was recorded to track the evolution of the diffraction peaks caused by nanowire bending. For the single nanowire measurement (sample 5), we considered only few selected 2D cuts through the 3D RSM to improve the time resolution of monitoring the XRD signal during nanowire bending.

The samples measured by XRD were intended to show a smaller bending compared to the samples inspected only by SEM because the diffraction signal could be followed only up to the maximum diffraction angle defined by the size of the pMBE beryllium windows. Therefore, the XRD data refer rather to the early stages of shell growth and nanowire bending.

The axial strain and bending can be distinguished by the changes of Bragg peak profile in the RSMs (see figures 4.2 and 4.5) as follows:

- Nanowire bending results in continuous change in the orientation of the GaAs(111) lattice planes resembled by broadening of the Bragg peak along a sphere in the RSM.
- In case of no axial strain, the RSM sphere has a radius equals to the amplitude of Q_z which gives the inter-planar spacing (d_{111}) of the unstained nanowire crystal.
- When the axial strain is induced, the radius of the RSM sphere changes accordingly. In case of the tensile strain in the nanowire core (*i.e.* increment of d_{111} of GaAs crystal) the XRD signal shifts toward

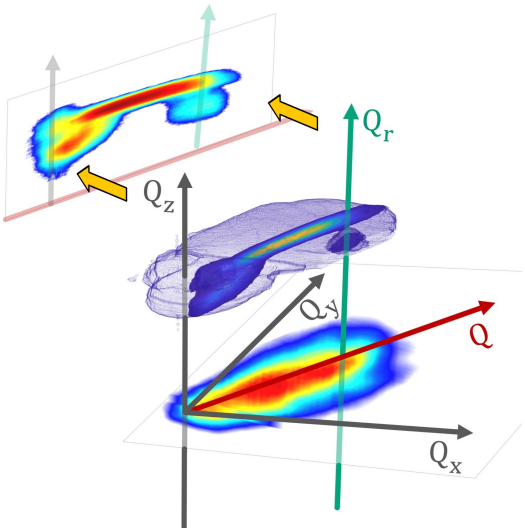

Figure 4.2: A demonstration of the 3D distribution of the XRD signal in RSM and the corresponding RSM vectors, in addition, a 2D cut in RSM of the same signal on QQ_z and a projection on Q_xQ_y.

lower Q_z value (thus smaller radius of the RSM sphere). The broadening of the peak along Q_z as highlighted with gray arcs in figure 4.5(b) results from continues changes of the lattice parameter across the nanowire cross section (*i.e.* gradient strain).

To evaluate the spatial changes of the signal on the RSM sphere, we introduce two new reciprocal space vectors Q and Q_r which share the same origin as Q_x, Q_y and Q_z as demonstrated in figure 4.2. The first vector Q is defined along the elongation of Bragg reflection as indicated by red arrow in figure 4.2. The amplitude of Q follows as $Q = \frac{|Q_y|}{cos(\delta)}$ where $\delta = 56°$ is the angle between the Bragg peak elongation direction (*i.e.* bending direction) and Q_y. The value of δ was extracted from the position of XRD peak center of mass on Q_x and Q_x. The other vector $Q_r = Q_z\ sin(\beta)$ is tilted from Q_z by the bending angle β of the nanowire as indicated by green arrow in figure 4.2. Therefore, to measure the axial strain induced by the shell in the nanowire, the XRD signal must be evaluated along Q_r in the RSMs.

4.2 Nanowire bending direction

Since the substrate within the MBE during the growth is stationary (*i.e.* the alignment of the nanowire templates with respect to the MBE cells is fixed), the $In_xGa_{1-x}As$ shell materials are deposited mainly on the nanowire side walls that face the material fluxes. The lattice parameters of the shell material are larger than that ones of the core, therefore, the induced mismatch axial strain (which is parallel to the nanowire axis $\epsilon_{||}$) causes the nanowire to bend away from the side at which the shell is deposited. The orientation of the material sources with respect to the Si substrate are shown in figure 4.3(a). For sample 1 (native oxide) we aligned the substrate in a way that a defined substrate edge is parallel to the direction of As flux (figure 4.3(a)). This edge is used as a reference for the later cleaving of the substrate (the red line in figure 4.3(a) indicate the cleaving edge). On the other hand, the thermal oxide substrate (sample 2) is aligned such that the cleaving edge

directs to the Ga flux as shown in figure 4.3(b). This alignment enables a

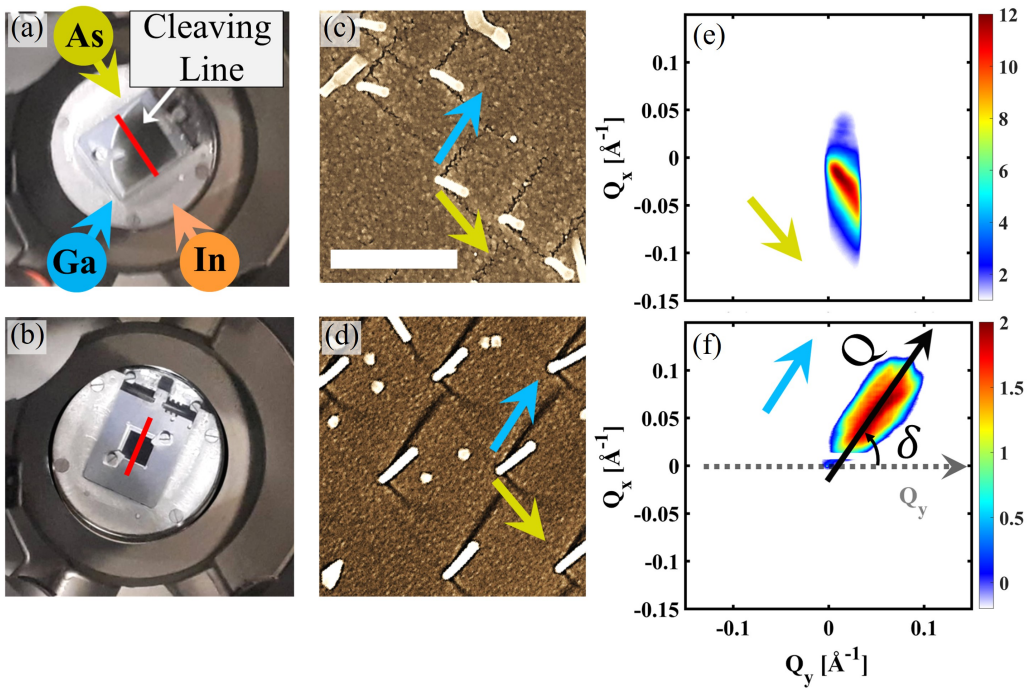

Figure 4.3: Nanowire bending direction. (a) and (b) Photographs of the geometrical arrangement of the growth material cells of the pMBE and the orientation of the quarter-inch substrate with native oxide layer (sample 1) and 1×1 cm patterned substrate with thermal oxide layer (sample 2), respectively. (c) and (d) Top-view SEM images of the bent nanowires of sample 1 and sample 2, respectively (The scale bar corresponds to 1μm). (e) and (f) Projection of GaAs(111) Bragg reflection on the $(Q_x Q_y)$ plane of RSM of the bent nanowires grown on substrate with native oxide layer (sample 3) and substrate with thermal oxide layer (sample 4) recorded after shell growth, respectively.

directional reference for the SEM inspection and side-view SEM evaluation of nanowire curvature. In top-view SEM, the bent nanowires appear as elongated objects and thus allow the extraction the bending direction, thanks to our proper sample alignment in the chamber. As shown in figures 4.3(c) and 4.3(d) the bending direction differ for both samples 1 and 2, respectively. In case of sample 1, the nanowires bend away from the As flux (yellow arrow in figure 4.3(c)), whereas in case of sample 2, the nanowires bend away from

the Ga flux (blue arrow in 4.3.d). This is an indication, that the position of the $In_xGa_{1-x}As$ shell in case of the thermal oxide (sample 2) is given by the position of the Ga-source, whereas it is given by the position of the As-source in case of the native oxide (sample 1).
This behavior was observed in all samples we used in this study as shown in figure 4.1, where the blue arrows indicate the direction of the Ga flux and yellow arrows indicate the direction of the As flux. As it can be seen from top-view SEM images in figures 4.1(b) and 4.1(f), the bending direction is in the direction of the As flux for the nanowires grown on native oxide substrates of sample 1 as well as sample 3. While for the nanowires grown on thermal oxide substrates, it can be seen in figures 4.1(d), 4.1(h) and 4.1(l) that the bending direction is in the same direction of the Ga flux.
Additionally, during the XRD measurements, several hundreds of nanowires were illuminated at the same time giving their mean properties and mean geometrical alignment. Using the same experimental conditions, the relative orientation of the nanowires geometry with respect to the reciprocal space geometry is consistent for all samples. Figures 4.3(e) and 4.3(f) show Q_xQ_y projection of the 3D RSMs of the GaAs(111) reflection for samples 3 and 4. The elongation of the Bragg peak clearly evidences that the bending directions are homogeneous within one substrate, but different for the two oxide types.
The difference in bending direction is surprising and hard to explain as we believe, that we can tell from literatures that for the core-shell nanowires, the VS growth is independent from the substrate characteristics. Since the nanowire side-walls act as substrates for the epitaxial VS growth, there was no report in literatures on the influence of the substrate type on the shell growth, to the extend of our knowledge.

4.3 Nanowire curvature profile

The careful alignment of the samples during growth made it possible to cleave the samples along the marked cleaving edge in figure 4.3 in such a way that side-view SEM investigations could be performed perpendicular to the bending directions. Figures 4.4(a) and 4.4(b) show side-view SEM images of bent core-shell nanowires grown on native oxide (sample 1) and thermal oxide (sample 2), respectively. The side-view images reveal that the curvature of

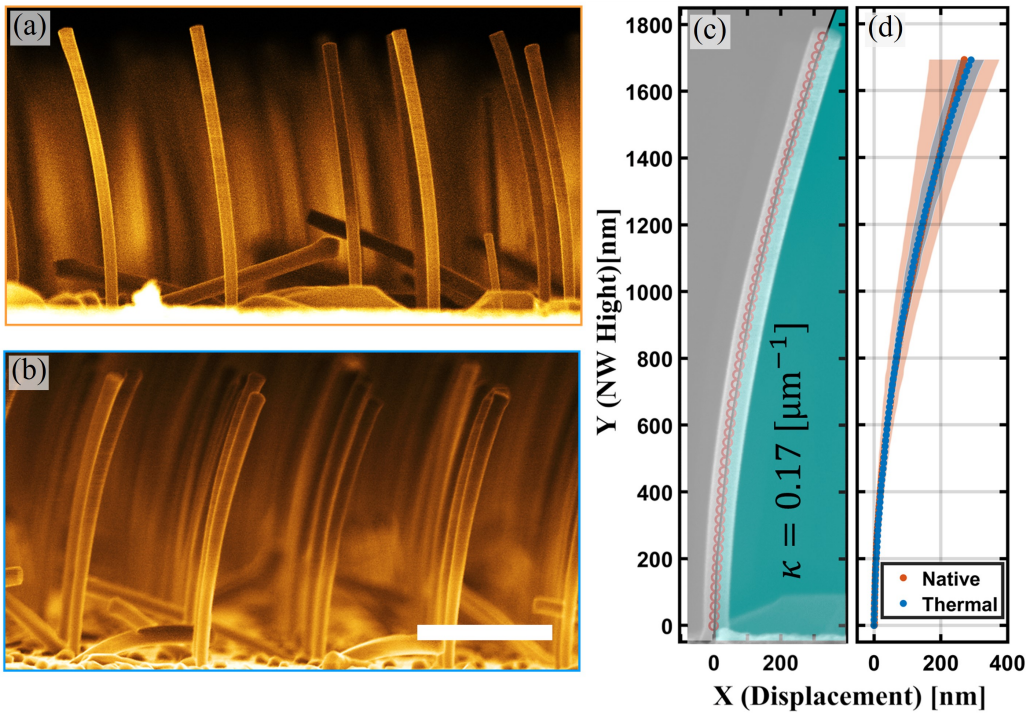

Figure 4.4: (a) and (b) side-view SEM images of bent nanowires grown on Si substrate with native oxide (sample 1) and thermal oxide (sample 2), respectively (The scale bar corresponds to 1μm). (c) Side-view SEM image of a selected bent nanowire with extracted curvature profile and a circle fitting function for exemplary illustration of the SEM evaluation method of nanowires curvature. (d) Comparison of the curvature profile of the nanowires of the mentioned samples, where the shaded areas indicate the curvature variation and the lines are their mean values.

the nanowires in sample 2 is more uniform than that of nanowires in sample 1. For quantitative analysis of the curvature, 47 nanowires from sample 1

and 40 nanowires from sample 2 were analyzed. Several data points were selected along the nanowire axis to obtain the bending profile. An exemplary visualization of this approach is demonstrated in figure 4.4(c). The curvature κ of this nanowire is about 0.17 μm^{-1} which was determined by fitting its profile using a circle function. In figure 4.4(d) the mean nanowire bending profiles of both samples (*i.e.* samples 1 and 2) are plotted. Both samples have the same mean curvature as shown in red and blue lines, respectively. However, the local variation of the nanowire curvature is larger in case of native oxide substrates as shown by red and blue shades in figure 4.4(d). This finding can be explained by the variation of the GaAs nanowire diameters when grown on native oxide substrates comparing to the case of nanowires grown on the patterned substrates. Additionally, the variation in the bending direction of the nanowires grown on native oxide substrates was observed to be higher as well which influence the side-view SEM inspection of these nanowire. However, the overall evaluation proves the homogeneous curvature along the nanowire full length, which implies axial-homogeneity of shell deposition along the nanowire growth axis.

4.4 In-situ XRD measurements of nanowire bending

The analysis of the temporal evolution of the bending process and the axial strain was performed by *in-situ* XRD experiments.
In order to record the whole nanowire bending, one needs to scan a wider range in reciprocal space compared to straight nanowires in order to cover the full elongation of the Bragg peak. The polytypism of GaAs nanowires can be utilized for a more accurate evaluation of the nanowire bending angle. During the first stages of Ga-assisted GaAs nanowire growth, the Ga droplet is unstable and small, resulting in the preferential growth of the WZ phase at the bottom of the nanowire (denoted by WZ_{Bottom}) and the inclusion of stacking faults [145]. During subsequent growth, the ZB phase and its rotational twin (TZB) are formed [75, 146]. To initiate radial VS growth, the

axial VLS growth needs to be terminated by consuming the Ga catalyst as explained in 2.2.2. The consumption of the droplet changes the growth conditions and faulted ZB segments and WZ segments are formed on the top of the nanowire (denoted by WZ_{Top}) [107, 147]. Notably, when measuring the GaAs(111) Bragg reflection, ZB and its twin overlap at the same position in reciprocal space, and therefore cannot be distinguished, whereas the WZ is separated from the ZB signal. Figures 4.5(a) and 4.5(b) show Q_xQ_z projec-

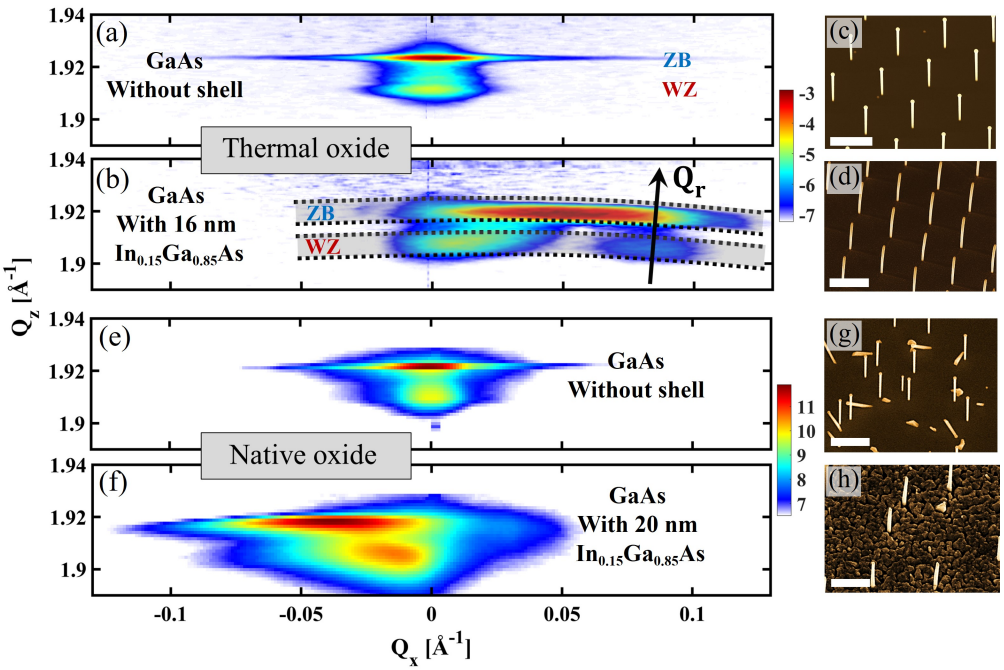

Figure 4.5: (a) and (b) GaAs(111) Bragg's reflection from nanowire ensembles on thermal oxide substrate (sample 4) projected on (Q_xQ_z) plane of RSMs recorded before shell growth and after 20 minute of depositing $In_{0.15}Ga_{0.85}As$ shell (which corresponds to about 16 nm of thickness) , respectively. (c) SEM images with 30^o tilt-view of GaAs nanowire of a reference sample grown under same growth condition. (d) SEM images with 30^o tilt-view of sample 4. (e) and (f) GaAs(111) Bragg's reflection from nanowire ensembles on native oxide substrate (sample 3) projected on (Q_xQ_z) plane. (g) and (h) are the respective 30^o tilt-view SEM images, where (g) is from a reference sample and (h) from sample 3. (All scale bars correspond to $1\mu m$).

tions of the GaAs(111) Bragg reflection of nanowires grown on the thermal oxide substrate (sample 4) before and after shell growth, respectively, indi-

cating nanowire bending. In both figures, the XRD peaks of ZB and WZ are clearly discernible. Comparing figures 4.5(a) and 4.5(b), the WZ and ZB peaks show significant changes, *i.e.* elongation of the ZB peak, and elongation and splitting of the WZ peak. SEM images with 30° tilt-view of the straight and bent nanowires are shown in figures 4.5(c) and 4.5(d), where the straight GaAs nanowires are from a reference sample grown under identical growth conditions of the studied sample. Similar *in-situ* XRD measurement was performed on nanowires grown on native oxide substrate (sample 3). The XRD signals of these wires before and after shell growth are shown in figures 4.5(e) and 4.5(f). The different elongation directions of the (111) Bragg peak for nanowires grown on thermal oxide substrate of sample 4 (figure 4.5(b)) and native oxide substrates of sample 3 (figure 4.5(f)) confirm the dependency of the bending direction on the oxide type. In further XRD study we focus on the nanowires grown on thermal oxide substrates (*i.e.* samples 4 and 5). For nanowire that is straight and vertical to the substrate surface, all ZB lattice planes are flat and parallel in real space, which results in a sharp XRD peak at $Q = 0$ Å^{-1} in RSM as shown in the lowest panel in figure 4.6(a) where the width corresponds to the divergence of the probing X-ray beam. As soon as the nanowire starts to bend, the orientation of the lattice planes becomes a function of their position along the nanowire axis in real space causing broadening of the XRD peak in RSM. Figure 4.6(a) shows the changes of the XRD signal on QQ_z at different stages during shell growth time. By estimating the integrated intensity ratio of the ZB peak to the total signal, it is apparent that the ZB phase represents about 80% of the crystal structure of the nanowire.

Figure 4.6(a) shows that the XRD signals of the WZ phase behave differently from the signal of ZB due to their distribution along the nanowire where WZ phase locates mainly at the bottom and the upper part of the nanowire. In straight nanowires, the XRD peaks of the two WZ segments (*i.e.* WZ_{Bottom} and WZ_{Top}) are located at the same position at $Q = 0$ Å^{-1} in reciprocal space. As soon as the nanowire starts to bend, the WZ_{Top} peak moves accordingly, whereas the WZ_{Bottom} peak changes by negligible amount which leads to peak

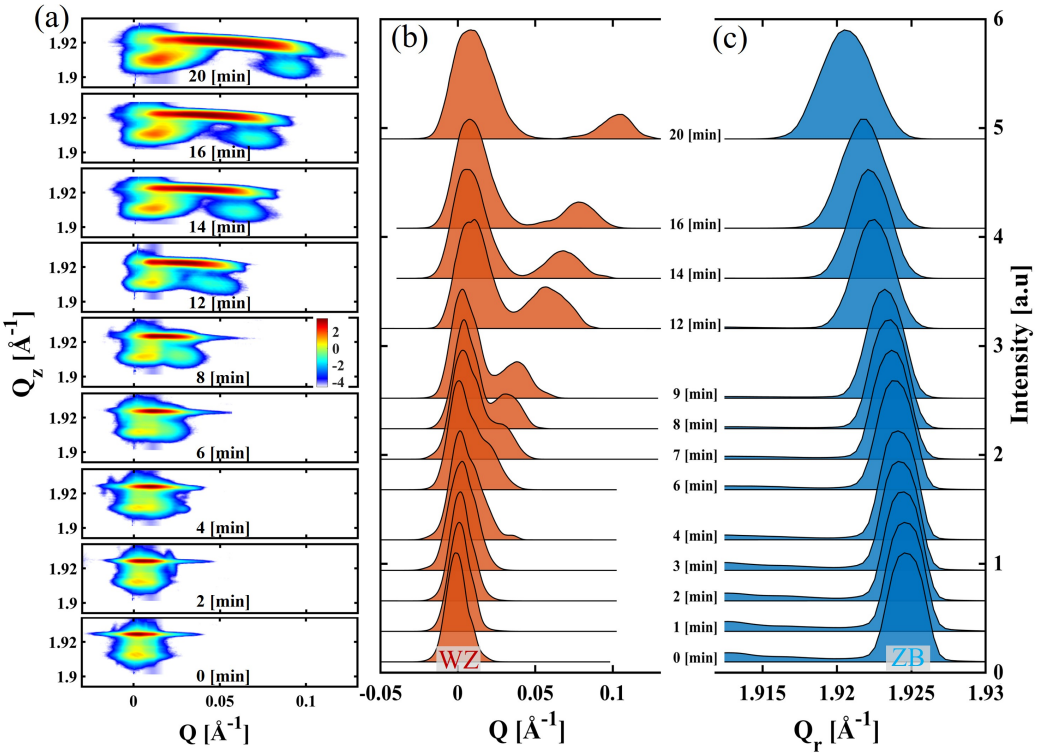

Figure 4.6: (a) 2D cut in RSM along Q of the GaAs(111) XRD signal on QQ_z of the NW arrays (sample 3) at different shell growth times. (b) The integrated line profiles along Q of the WZ peaks, and (c) along Q_r of the ZB peaks.

splitting in reciprocal space as shown in figure 4.6(a) and 4.6(b). Therefore, by knowing the mean length of the nanowires, the complete circular bending of the nanowire can be extracted from the separation of the two WZ peaks where this methods provide high accuracy. The integrated intensities of the WZ and ZB XRD signal along Q and Q_r during shell growth and the resulting line profiles are shown in figures 4.6(b) and 4.6(c), respectively. The center of ZB peak during shell growth is located in between the two WZ peaks confirming the phase distribution along the nanowire.

Nanowire curvature analysis

As the bending is found to be homogeneous, the curvature κ of the bent nanowires can be described by a specific bending radius ($r = \kappa^{-1}$) and the bending angle β with respect to the normal of the substrate.

To evaluate and extract the nanowire curvature values from the XRD signals in RSM, first the WZ signal is integrated on a circle along Q where the radius of this circle is the peak center along Q_r. The integrated line profiles of this signal are plotted in figure 4.6(b) showing that splitting and the slight broadening of the WZ peak is developing as the shell growth time is increasing. However, for the case of nanowire curvature measurement we consider the position of the WZ_{top} signal in RSM where the bending angle of this segment is the bending angle of the nanowire as illustrated in figure 4.7. For the measurement of the nanowire bending angle (β) we use Gaussian function to fit the XRD peak profile of WZ_{top} and determine its position on Q. The peak position on Q at time t ($Q^t(WZ)$) is extracted on the surface of RSM sphere that has a radius $Q_r^t(WZ)$. The broadening of the WZ peak at low Q values (*i.e.* WZ_{Bottom}) as well as its higher intensity comparing to WZ_{Top} signal demonstrate the difference in the length of these segments along the nanowire as shown in figure 4.8(a). This observation confirms (in a reversible argument) that nanowire bending may also be used to estimate the axial distribution of ZB and WZ polytypes along the nanowire by XRD measurement.The extracted peak positions of the respective polytypes are

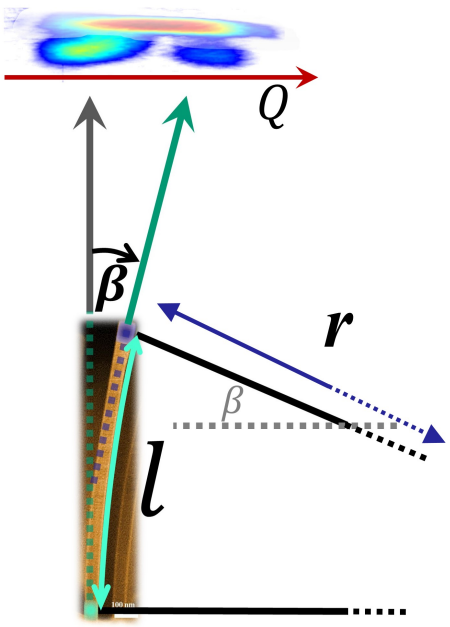

Figure 4.7: Illustration of the parameters used for calculating the nanowire curvature combined with side-view SEM image of a bent nanowire in real space and the XRD signal in RSM.

shown in figure 4.8(b). In this case the bending angle is

$$\beta = \tan^{-1}\left(\frac{Q^t(WZ)}{Q_r^t(WZ)}\right) \tag{4.1}$$

Therefore, the bending angle β of the nanowire and the nanowire curvature κ by can be measured from the tilting angle of WZ_{Top} and the average length of the nanowires l_{NW}

$$\kappa = \frac{\beta}{l_{NW}} \tag{4.2}$$

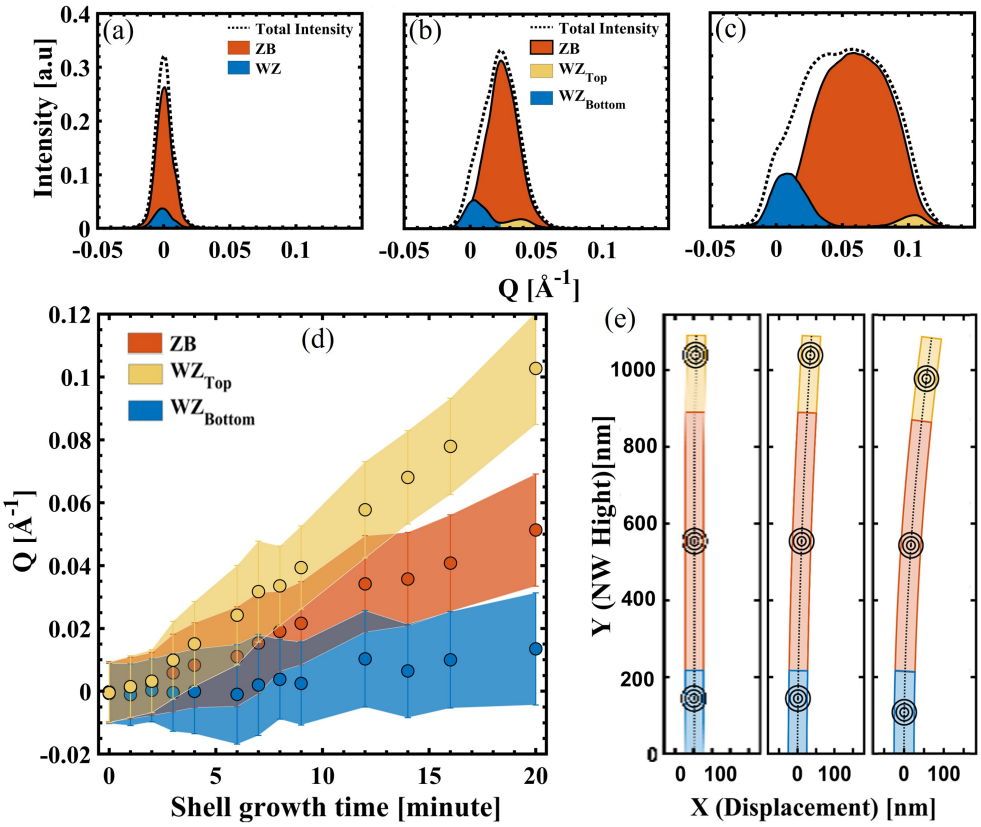

Figure 4.8: Profiling the XRD signals of sample 4. (a), (b) and (c) are intensity profiles of the XRD signals of the respected polytypes at three different growth stages integrated along Q. (d) The peak positions of ZB, WZ_{Top} and WZ_{Bottom} along Q plotted as function of shell growth time. (e) Modeled phase stacking based on circular bending.

The tilt angle of (WZ_{Top}) at the final stage (*i.e.* after 20 min of shell growth which corresponds to 16 nm shell thickness) is $\beta \approx 3°$ considering the measured average length of the nanowires of $l_{NW} = 1100$ nm. In this case the resulting final curvature is $\kappa \approx 0.047\ \mu\text{m}^{-1}$. The distribution of both polytypes along the nanowire as well as the calculated nanowire bending at three selected growth stages by our model of circular bending are visualized in figure 4.8(e). The evolution of nanowire curvature during shell growth is plotted as function of shell growth time in figure 4.9(a). The curvature is determined by considering the mean nanowire length from a reference sample of straight nanowires shown in figure 4.9(b).

Axial strain analysis

For strain analysis, we consider only the strain induced in the GaAs(ZB) phase, since it is the prominent structure along the nanowire.
The variation of the peak position along Q_r was used to measure the average axial strain $\epsilon_{||}$. By considering the position of GaAs(111) Bragg peak of the unstrained nanowire (*i.e.* the GaAs nanowire signal before shell growth) as a reference to measure the changes of inter-planar distance d^t_{111} of GaAs(ZB) at different shell growth times t as following

$$\epsilon^t_{||} = \frac{d^t_{111} - d^0_{111}}{d^0_{111}} \tag{4.3}$$

where d^0_{111} is the inter-planar spacing of GaAs(ZB) before shell growth. These parameters are measured from the values of the peak center on Q_r at time t which we denoted here as Q^t_r

$$d^t_{111} = \frac{2\pi}{Q^t_r} \tag{4.4}$$

Therefore, from equations 4.3 and 4.4, the axial strain is

$$\epsilon^t_{||} = \frac{Q^t_r - Q^0_r}{Q^0_r} \tag{4.5}$$

The evolution of the axial strain as function of shell growth time is plotted

in figure 4.8(c) where the broadening of the peaks along Q_r was considered to measure the strain variation across the nanowire as indicated by bars in figures 4.9(c) and 4.9(d). In this case the standard deviation σ_r^t of the signal along Q_r at time t is used to determine the strain variation as follows

$$\Delta(Q_r^t) = (Q_r^t - \sigma_r^t) \tag{4.6}$$

thus

$$\Delta\epsilon_{||}^t = \frac{\Delta(Q_r^t) - \Delta(Q_r^0)}{\Delta(Q_r^0)} \tag{4.7}$$

In this case the peak broadening of the XRD signal of the unstrained nanowires (*i.e.* $\Delta(Q_r^0)$ is taken as a reference value to distinguish the contribution of the normal distribution of the X-ray signal that results from the beam profile and the vertical variation of the unstrained nanowires.
The evolution of the nanowire curvature and the strain are not linear with the shell growth time as shown figures 4.9(a) and 4.9(c), respectively. During the early shell growth runs of up to around 5 minutes, minor curvature and strain occur. Exceeding the growth time of 5 minutes, the changes in nanowire curvature increases and reaches a value of about $\kappa \approx 0.05\ \mu\text{m}^{-1}$ after 20 minute of shell growth where the axial strain reaches a value of $\epsilon_{||} \approx 0.003$.

Nevertheless, the relation between the curvature and strain is linear as shown in figure 4.9(d) which implies that the linear elasticity of the studied core-shell system is still valid. The non-linearity of relation between the shell growth time and the evolution of the strain and the curvature may be attributed to the changes of the growth dynamics during shell growth.
The axial lattice spacing (d_{111}) of the unstrained ZB can be measured from the diffraction peak on Q_r by $d_{111(GaAs(ZB))} = \frac{2\pi}{Q_{r(GaAs(ZB))}}$. The position of the Bragg peak on Q_r of the unstrained ZB at growth temperature is $Q_{r(GaAs(ZB))} = 1.9239$ Å^{-1} therefore $d_{111(GaAs(ZB))} = 3.2659$ Å and the corresponding lattice parameter $a_{(GaAs(ZB))} = 5.6566$ Å.

Using Vegard's law [148], the lattice parameter of the shell is $a_{(In_{0.15}Ga_{0.85}As)} = 5.7174$ Å and which is the maximum allowed shared lattice parameter between the core and the shell, *i.e.*, $\epsilon_{||}^{max} = \frac{a_{(In_{0.15}Ga_{0.85}As)} - a_{(GaAs)}}{a_{(GaAs)}} = 0.01$.

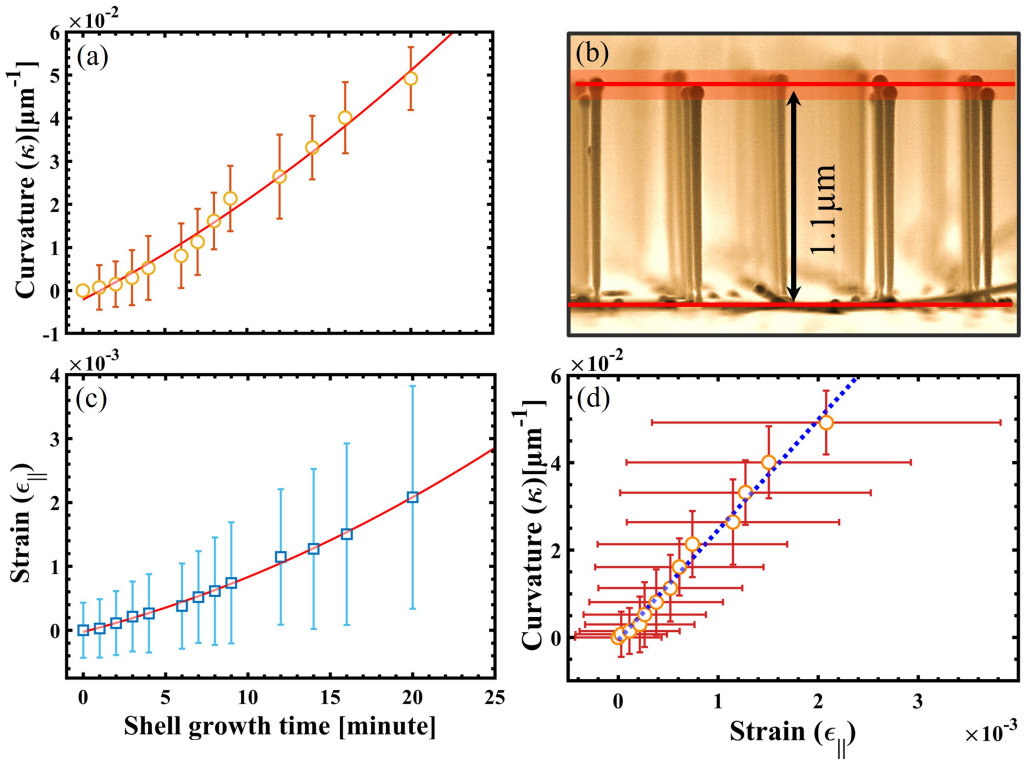

Figure 4.9: (a) Evolution of nanowire curvature as function of shell growth time. The curvature is measured by considering the nanowire length of a reference sample grown under identical growth conditions of the sample shown in (b). (c) Strain evolution in the ZB polytype as function of shell growth time. (d) Evolution of nanowire curvature as function of induced strain extracted from the *in-situ* XRD measurement of sample 4.

Therefore, considering the deduced linear relation between the strain and the curvature (figure 4.9(d)), the maximum predicted curvature that occurs at $\epsilon_{||}^{max}$ will not exceed $\kappa \approx 0.25\,\mu\text{m}^{-1}$. For this prediction the associated maximum effective shell growth time is ≈ 55 minute that generates the axial strain and nanowire bending. However, this prediction holds only for the given core-shell system and it may differ for different parameters such as nanowire core diameter and In concentration as well as the inhomogeneity degree of the shell distribution.

4.4.1 Single nanowire measurement

To extend on our observations and get a deeper insight into the nanowire bending and strain evolution at the early stages of shell growth, we performed *in-situ* XRD measurement on a single nanowire during shell growth. In the case of single nanowire, it was intended to observe the changes of the signal with time resolution of 11 second that is sufficient to obtain enough signal intensity in each frame. Therefore, 2D maps were taken and the data are evaluated on Q_x and Q_z RSM vectors. Few 2D maps taken at different shell growth times are shown in figure 4.10(a) and the extracted intensity profiles along Q_x and Q_z of all maps are shown in figures 4.10(c) and 4.10(d) respectively. After every seven scans, the Si(111) signal were recorded to be used as a reference for the RSM evaluation.

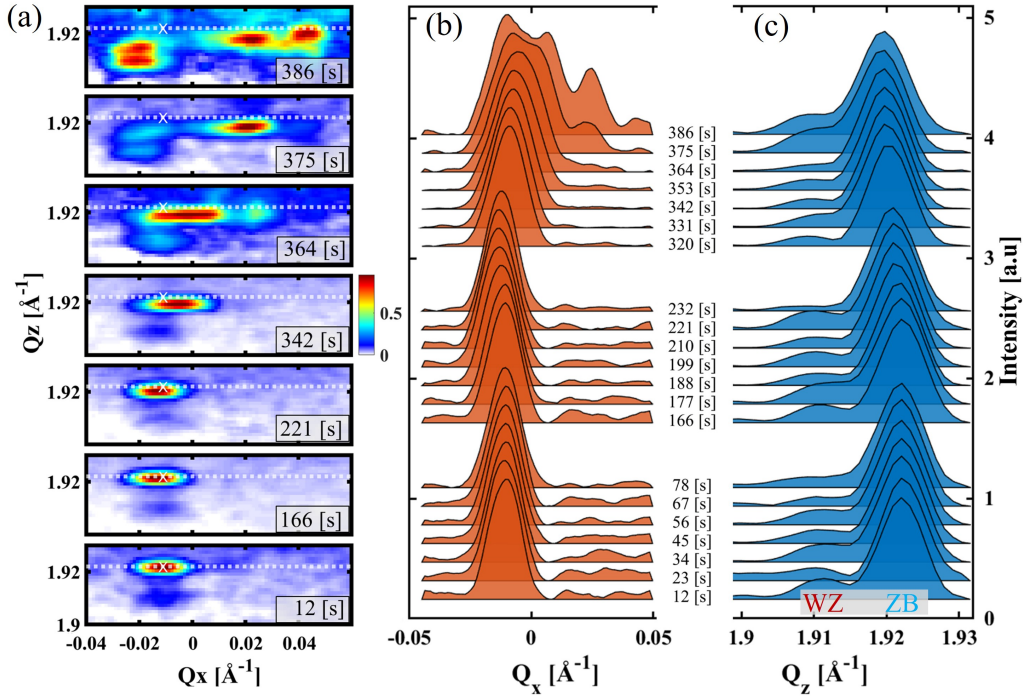

Figure 4.10: (a) 2D cuts in RSM along Q_x of the GaAs(111) XRD signal on Q_xQ_z of the single nanowire (sample 5) at different shell growth times. (b) The integrated line profiles along Q_x of the entire nanowire signal, and (c) along Q_r of the ZB peaks.

It can be seen in figure 4.10(a) that during the growth of the first few shell layers, the ZB peak slightly shifts toward lower Q_z values (a reference horizontal line is plotted in figure 4.10). During further growth, the peak keeps shifting toward lower Q_z values and start to broaden toward higher Q_x values which corresponds to a progressive bending caused by the increasing amount of strain induced by the growing shell.

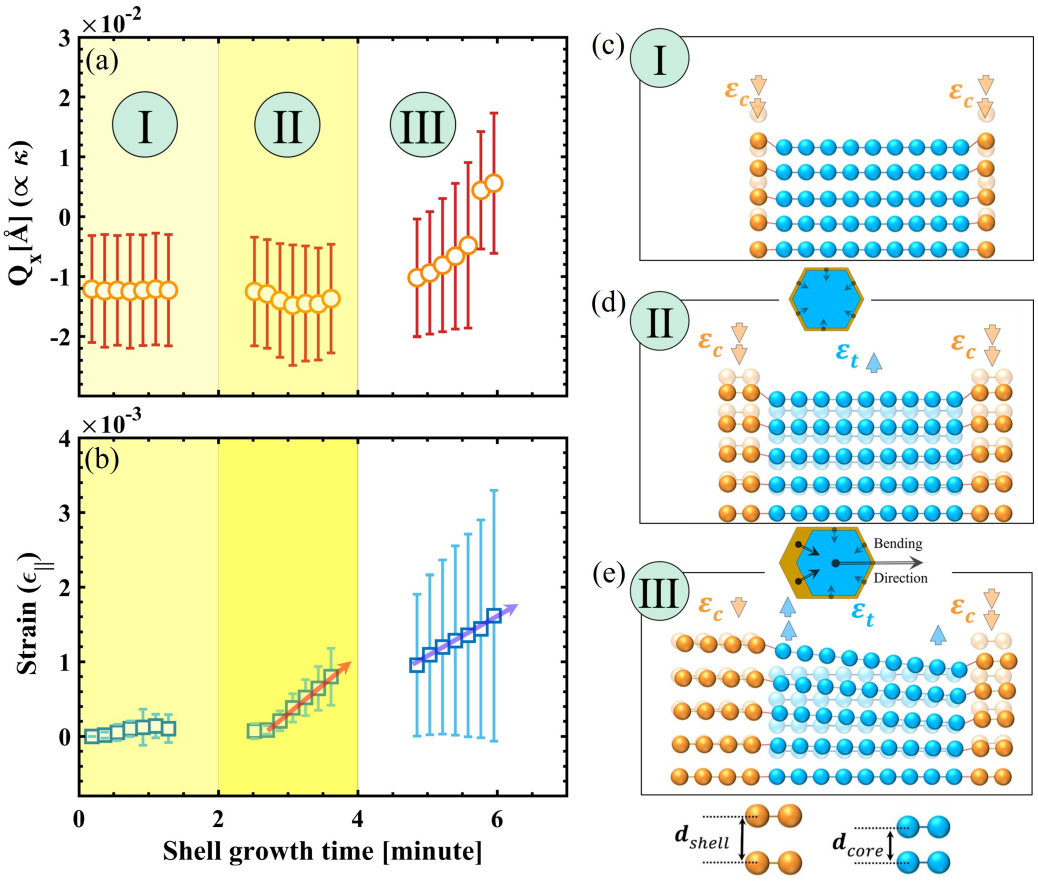

Figure 4.11: (a) Evolution of the bending angle of the single nanowire during shell growth. (b) Strain evolution in the ZB polytype of the single nanowire during shell growth of sample 5. (c) Animation of the three phases of shell growth indicating the axial strain of the core-shell nanowire and the resulting changes of the lattice plane orientation and the nanowire bending.

The growth was terminated after 11 minutes of shell growth corresponding to shell thickness of $\approx$ 5.5 nm. The position of Bragg peak on Q_x which

indicates nanowire bending and the induced strain are plotted as functions of shell growth time in figures 4.11(a) and 4.11(b), respectively. It can be seen in 4.11(a) and 4.11(b) that both quantities pass through three phases during the early stages of shell growth can be explained as follows

- At phase-I, corresponding to about 2 minutes of shell growth time, no clear bending and minor strain is observed. At this stage, the first few monolayers of the growing shell (approximated to be with 1 nm in thickness) are subjected to a compressive strain to match the GaAs lattice and thus, these layers can scarcely influence the lattice parameter of the nanowire core as illustrated in figure 4.11(c).
- At phase-II, up to 4 minutes of shell growth time, a clear increase of the strain can be observed, while the nanowire bending angle slightly fluctuates. This observation can be explained by a quasi-uniform shell growth around the nanowire core facilitated by the smooth and unstrained nanowire side-facets. In this case the nanowire surface allows the shell material to diffuse freely and nucleate uniformly around the nanowire which results in a symmetric axial strain (uniform strain) that causes no nanowire bending as illustrated in figure 4.11(d).
- At phase-III, both bending angle and strain showed simultaneous increase. At this stage, as the strain increases the diffusivity of the shell material decreases accordingly. As a consequence of the decrement of the shell material diffusivity, the growth rate becomes higher on the nanowire facets that face the direct fluxes than the ones on the opposite side. Therefore, a non-uniform shell thickness around the nanowire results in varying strain across the nanowire cross section and thus nanowire bending as illustrated in figure 4.11(e). In this case, because of the induced asymmetric strain, the nanowire side that is subjected to higher tensile strain becomes more favorable for the continues shell growth than the other side of the nanowire which results in further increment of the growth rate on the tensile strained side. The opposite side of the nanowire, is subjected to two competitive sources of strain, where a tensile strain results from the shell material that may grow even with low growth rate and a compressive strain caused by

nanowire bending. This regime may explain the non-linear increment of the nanowire curvature and strain during shell growth as plotted in figure 4.9(a) and 4.9(b), respectively.

These assumptions can be supported by the changes of the strain evolution between phase-II and phase-III. It is clear that the increment of the strain is higher at phase-II (indicated by red arrow in figure 4.11(b)) than phase-III (blue arrow in figure 4.11(b)) where a certain amount of the strain is released by the nanowire bending. The strain variation across the nanowire cross-section is represented by the bars in figure 4.11(b). This variation was estimated from the broadening of the XRD peak along Q_z as it can be seen by the line profile in figure 4.10(a).

4.5 Summery of chapter 4

As demonstrated in this research, uniform nanowire bending with controllable curvature along a definable bending direction can be achieved by avoiding substrate rotation during MBE growth of a lattice-mismatched shell. In this work, using Si substrates covered with native and thermal oxide, we observed different preferable bending directions of GaAs-$In_xGa_{1-x}As$ core-shell nanowires. The bending direction which implies the preferable nanowire side facets for shell growth showed a clear dependency not only on the arrangement of the material sources, but also on the type of the oxide covering the substrates. For the given arrangement of the effusion cells in our MBE system we observed that the nanowires bend away from the direction of the Ga flux in case of using substrates covered with thermal oxide. On the other hand, nanowires grown on substrates covered with native oxide bend away from the direction of the As flux. This difference in the bending behavior requires further investigation and justification. However, by means of sensitive and non-destructive *in-situ* XRD measurements of the axial GaAs(111) Bragg reflection, and benefiting from our previous knowledge of the crystal phase distribution along the nanowire growth axis and the bending direction, we obtained a deep insight into the evolution of the induced axial strain and the resulting nanowire bending.

The evolution of the strain and nanowire bending showed non-linear dependency as function of shell shell growth time. The non-linearity of these functions was attributed to the changes of the growth dynamics during shell deposition due to the changes of the surface properties of the nanowire. The performed *in-situ* XRD investigation on a single nanowire revealed that at the early shell growth stages, first the strain increases while the nanowire stays straight which suggests a uniform strain emerge from a homogeneous distribution of the lattice-mismatches shell around the nanowire core. Afterward, as the shell growth proceed, nanowire bending starts to take place alongside with the increasing strain indicating changes in the homogeneity degree of the shell distribution around the nanowire. The induced asymmetric strain results different growth rate at the opposite nanowire facets which in turn increases as the shell growth proceed.

Chapter 5

Shadowing effect on the strain distribution along the nanowire and the resulting nanowire bending profile

Abstract

Here we report on non-uniform shell growth of $In_xGa_{1-x}As$ onto GaAs core by molecular beam epitaxy (MBE) using pre-patterned silicon substrates with pitch sizes (p) ranging from 0.1 µm to 10 µm as shown in chapter 3. Exploiting the knowledge we obtained in chapter 4 about the preferable bending direction with respect to the MBE cells as well as the layout of the substrate pattern we are able to tune the strain distribution along the nanowire growth axis and the subsequent bending profile. At nanowire arrays with high density, the obtained bending profile of the nanowires composed of straight (barely-strained) and bent (strained) parts with different lengths that depend on the pitch size. A precise control of the bent and straight nanowire segment length provides a method that can be used for nanowire-based devices with novel geometry as well as for strain gradient engineering.

5.1 The fundamental idea and experimental methods

The samples used in this study are samples 2 and 4 as labeled in 4.1.1. The shell growth parameters were chosen in a way to have high nanowire bending in order to demonstrate, using SEM, the effect of shadowing (sample 2) by having a higher In content ($x = 0.3$) and a thicker shell ($\approx$ 24 nm). During shell growth, this sample was aligned in a way that the flux shadowing is done by the neighboring nanowires (*i.e.* the distance between the nanowires on the bending direction is p). Sample 4 was grown to monitor the evolution of the strain and nanowire bending as function of p during shell deposition by $in - situ$ X-ray diffraction (XRD) experiment. Therefore, this sample was grown with lower In content ($x = 0.15$) and less shell thickness ($\approx$ 16 nm) resulting in a lower bending compared to the first sample offering the chance to monitor the nanowires bending over the shell growth time. The shadowing in this sample is done by the next neighboring nanowires (*i.e.* the distance between the nanowires along the bending direction is $\sqrt{3}\,p$). The total shell growth time for sample 4 was 20 minutes and done in several intervals as we deposited a certain shell thickness, followed by an interruption of the growth in which the XRD experiment is performed as explained in 4.1.1. In a previous work, it was observed that the nanowire volume depends on the number density of growing nanowires explained by the differences in the local growth conditions [149]. Considering the substrate area around an individual nanowire is acting as reservoir for nanowire growth, the decrement of p associated with shadowing of the Ga-flux by neighboured nanowires results in the growth of shorter and thinner nanowires compared to the ones with larger p (lower density) [69, 96, 150, 151] as shown in chapter 3.

As explained in the previous chapter of this work, the pMBE chamber is equipped with Ga and In effusion cells and an As_4 valve cracker cell as animated in figure 5.1(a).An observed influence of the cells arrangement on the bending direction of the nanowires was reported in chapter 4 of this work. For nanowires grown on Si substrates with thick oxide layer, shell deposition takes place mainly on the nanowire side walls that are facing the Ga

flux. Therefore, the shell material was deposited inhomogeneously onto the nanowire side walls and caused nanowire bending toward the direction of the Ga flux (i.e [11-2] direction in our case) as illustrated schematically in 5.1(a). According to the previous study [55], the lattice mismatch between the core and the shell results in strain that is parallel to nanowire axis $\epsilon_{\parallel}$ concentrates at the core-shell interface and changes radially across the nanowire diameter (illustrated in figure 4.11(e)).
The predetermination of the bending direction and the geometrical arrangement of the pMBE effusion cells with respect to the nanowire arrays are exploited to control the strain distribution and the bending profile of the nanowires as demonstrated in figure 5.1(b). The nanowire arrays with high number density (*i.e.* $p = 100$ nm) that originate prominent flux shadowing have straight (shadowed) lower part and bent (exposed) upper part of the nanowire (see figures 5.1(b) and 5.1(d)). The length ratio of the exposed ($l_{exposed}$) and the shadowed ($l_{shadowed}$) nanowire segments can be controlled by changing the flux angle (Φ_{flux}), nanowire length (l) and the distance (p) as animated in figure 5.1(b). The length of the exposed nanowire segment ($l_{exposed}$) can be rationalized by

$$l_{exposed} = \frac{p}{\tan(\Phi_{flux})} \tag{5.1}$$

The diffusion of the shell materials on the nanowire surface from the exposed part toward the shadowed part of the nanowire must be considered and the length of the bent segment of the nanowire (l_{bent}) can be calculated by

$$l_{bent} = l_{exposed} + l_D \tag{5.2}$$

where l_D is the length of the nanowire segment at which shell growth takes place only by the diffused material, *i.e.* no direct flux.
The length l_d indicate the effective diffusivity of group-III materials on the nanowire surface that accumulate and causes strain-induced nanowire bending. Figure 5.1(c) shows an exemplary 30° tilt view SEM images of a reference GaAs nanowires in arrays with $p = 100, 200, 400$ and 700 nm, evidencing

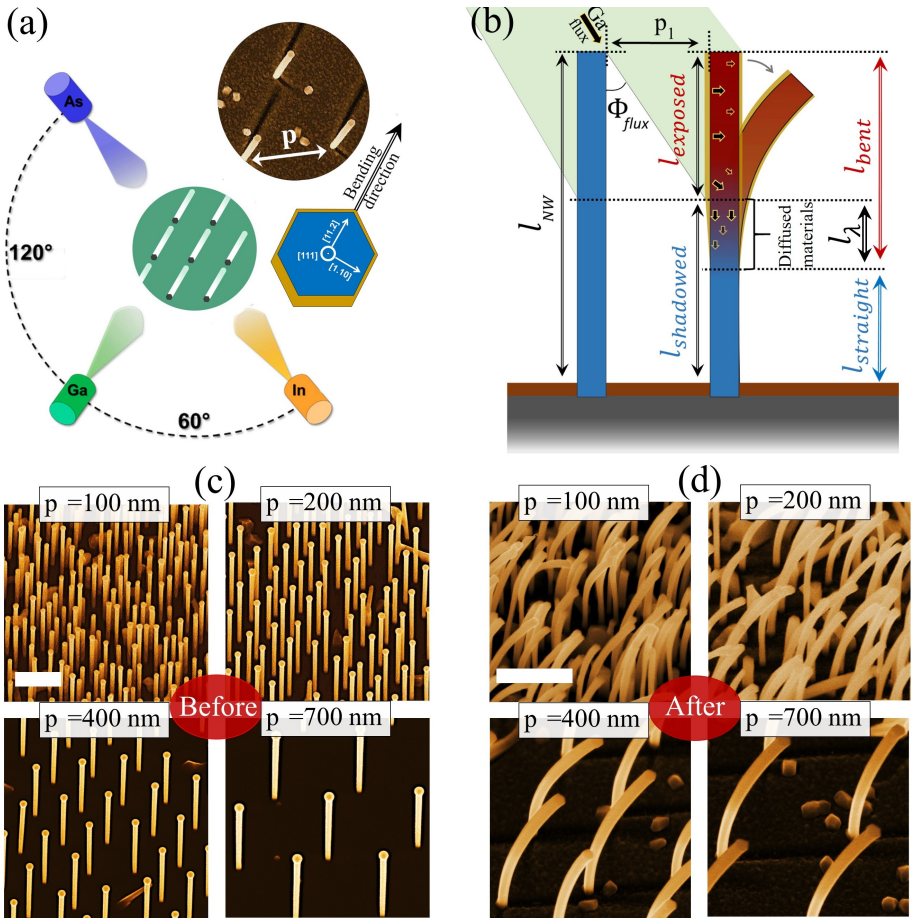

Figure 5.1: (a) Illustration of the azimuthal arrangement of the MBE cells and the pattern of the substrate. (b) An illustration of the materials flux shadowing by neighboring nanowires. (c) 30° tilt view SEM images of reference GaAs nanowire arrays with different pitch size p. (d) 30° tilt view SEM images of bent GaAs - $In_{0.3}Ga_{0.7}As$ core - shell nanowires in arrays with different pitch size p (sample 2). (scale bars correspond to 500 nm)

high nanowire yield. In figure 5.1(d), 30° title view SEM images are taken from four arrays of sample 4 with different p showing significant variation of bending profiles along the nanowires which implies the variation of strain distribution along these nanowires. For the nanowires at the arrays with $p =$ 100 nm and $p = 200$ nm, the bending occurs only at the upper part that appears thicker in diameter compared to the straight lower part due to the shadowing effect on the later.

XRD measurement

For deeper insight into evolution of strain magnitude and distribution along the nanowires and statistically meaningful profiling of the nanowire bending at the different nanowire arrays, we performed $in-situ$ XRD experiment. By scanning the sample across the X-ray beam while fulfilling the GaAs(111) Bragg's reflection, the micro-fields of nanowires were precisely located with respect to the diffractometer geometry as explained in 2.3.3. The resulting 2D map of the micro-fields is displayed in figure 2.13(c) where the diffracted intensity is proportional to the total volume of the illuminated crystals (*i.e.* nanowire volume and density). The recorded 3D RSMs are represented by the reciprocal space vectors explained in 4.1.2 and demonstrated in figure 4.2. As discussed in chapter 4, thicker shell exerts a stronger bending force on the nanowire core where the axial component of the lattice mismatch strain $\epsilon_{||}$ increases. However, for consistent In content we monitored the evolution of nanowire bending as function of $In_{0.15}Ga_{0.85}As$ shell growth time for sample 4. Figure 5.2(a) shows the 3D distribution of the GaAs(111) Bragg reflection in RSM for the nanowire arrays with $p = 100, 200$ and 400 nm recorded after different $In_{0.15}Ga_{0.85}As$ shell growth rounds during the $in-situ$ XRD experiment. Additionally, in figure 5.2(a) highlighted 2D cross-sections of 3D Bragg reflections on QQ_z component of the RSMs where Q is indicated by blue arrow. The lower images in figure 5.2(a) are the Bragg peak of straight and bare GaAs nanowire and the top images are that of GaAs nanowire cores after 20 minutes of shell growth.

5.2 Bending distribution along the nanowire

The recorded signals in 5.2(a) show that for the arrays with $p = 100$ nm and $p = 200$ nm the most intense part of the Bragg's reflection remains around Q=0 $Å^{-1}$ with some broadening toward higher Q values. This diffraction intensity distribution implies that large section of the illuminated nanowires expected to be at the lower section remains straight and perpendicular to the substrate surface, while the upper sections that exhibit bending contributes

to the broadening of Bragg peak. While for the nanowire arrays $p = 400$ nm, the peaks exhibit rather homogeneous broadening toward higher (Q) values indicating that the entire nanowire exhibit bending at this nanowire array.

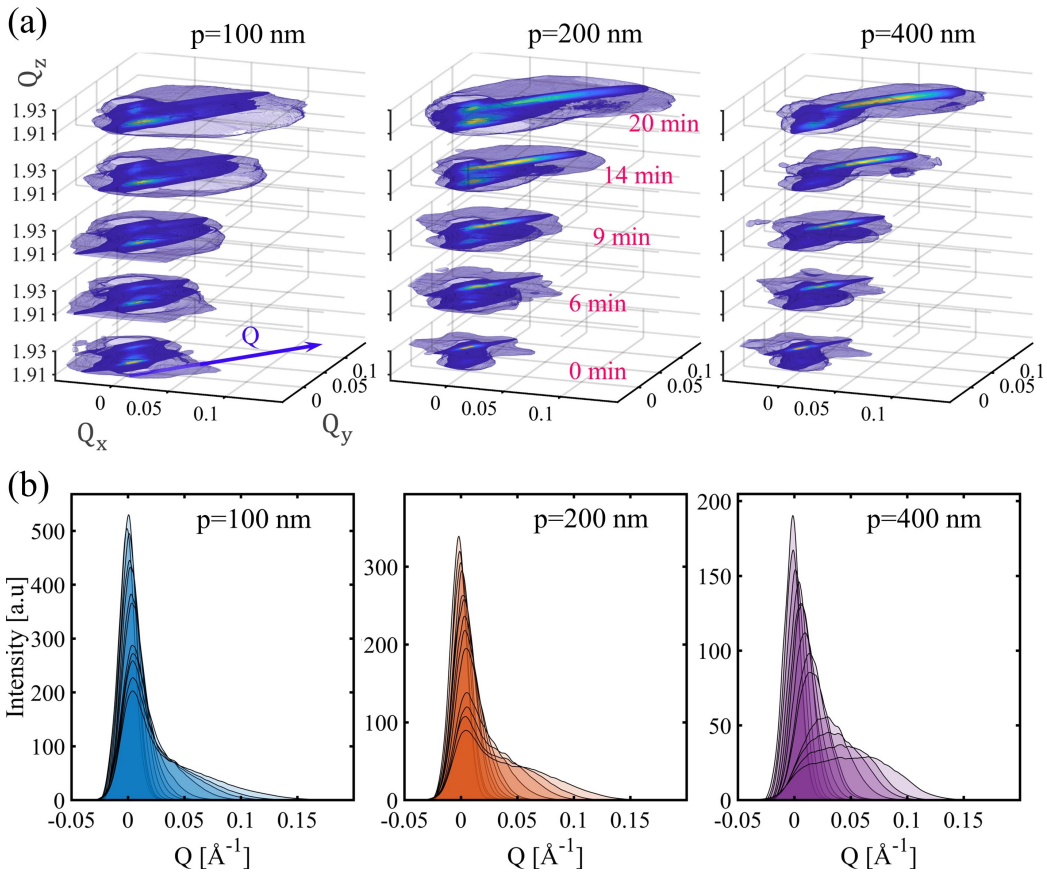

Figure 5.2: (a) 3D RSM of the GaAs(111) Bragg's reflections after different shell growth rounds stacked vertically for nanowire arrays with $p = 100, 200$ and 400 nm. (b) Integrated line profile of the intensity distribution of the XRD signal along Q in RSM.

The integrated intensity profiles of Bragg peaks along Q are plotted in figure 4.5(b). As it can be seen, the intensity of the integrated line profiles depends on the number density of the nanowires at the different arrays. The evolution of the Bragg peak intensity distribution along Q can be clearly seen where the peak maxima decreases and peak shape are changing as the shell growth proceed results in tailing of Bragg peaks of nanowires at the arrays with $p = 100$ nm and $p = 200$ nm . The increasing tailing of these peaks indicate

the developing nanowire curvature.
To evaluate the signal profiles, first we calculate the symmetry factor S (also known as tailing factor) of each Bragg peak along Q by

$$S = \frac{W_{0.05}}{2f_{0.05}} \tag{5.3}$$

where $W_{0.05}$ is the peak width at the 5% peak height and $f_{0.05}$ is the distance from the leading edge of the peak at 5% peak height to the position of the peak maxima on Q. The calculated S values for each Bragg peak of the different nanowire arrays are plotted as function of shell growth time in figure 5.3(a). As it can be seen, the calculated S of the XRD peaks of the arrays with $p = 400$ nm and $p = 700$ nm are close to $S \approx 1$ indicating high peak symmetry. The high peak symmetry in this case evidence that the entire nanowire exhibited curvature. At the high density arrays with $p = 100$ nm and $p = 200$ nm, the high values of S shown in figure 5.3(a) imply higher tailing of Bragg peaks toward higher Q values which in turn results from the varying nanowire curvature at these arrays.
Furthermore, as the nanowire curvature increases, the maximum intensity of Bragg peak $I^p_{max}(t)$ decreases due to the spreading of the diffracted signal distribution along Q. Figure 5.3(b) shows the relative changes of the line profile maxima of Bragg peak at different shell growth times. The maxima of Bragg peak intensity profile of the bare GaAs nanowire arrays $I^p_{max}(0)$ with p =400 nm and $p = 700$ nm before shell growth drops to $I^{400}_{max}(20) = 0.2 \times I^{400}_{max}(0)$ and $I^{700}_{max}(20) \approx 0.2 \times I^{700}_{max}(0)$. The maxima of Bragg peak intensity profile of the nanowire arrays with $p = 100$ nm (which locates around $Q = 0\text{Å}^{-1}$) decreases to $I^{100}_{max}(20) \approx 0.45 \times I^{100}_{max}(0)$ which means that $\approx 45\%$ of the diffracted signals from these nanowire arrays accumulate at the same position in RSM. Therefore, approximately 45% of the nanowire volume remained vertical to the substrate surface. The same approach is applicable for the nanowire arrays with $p = 200$ nm where $\approx 25\%$ of the signal remains at the same position in RSM. To innervate this approach, the Bragg peaks of the bent nanowire at these arrays were deconvoluted by multiple-Gaussian fitting model as shown in figure 5.3(c). By integrating

the area of each Gaussian curve, this model reveals that ≈ 45% and 25% of the XRD signal from the arrays with p =100 nm and p = 200 nm remained around the initial position of the peak $Q = 0\text{Å}^{-1}$ in RSM (shaded with blue in figure 5.3(c)), respectively.

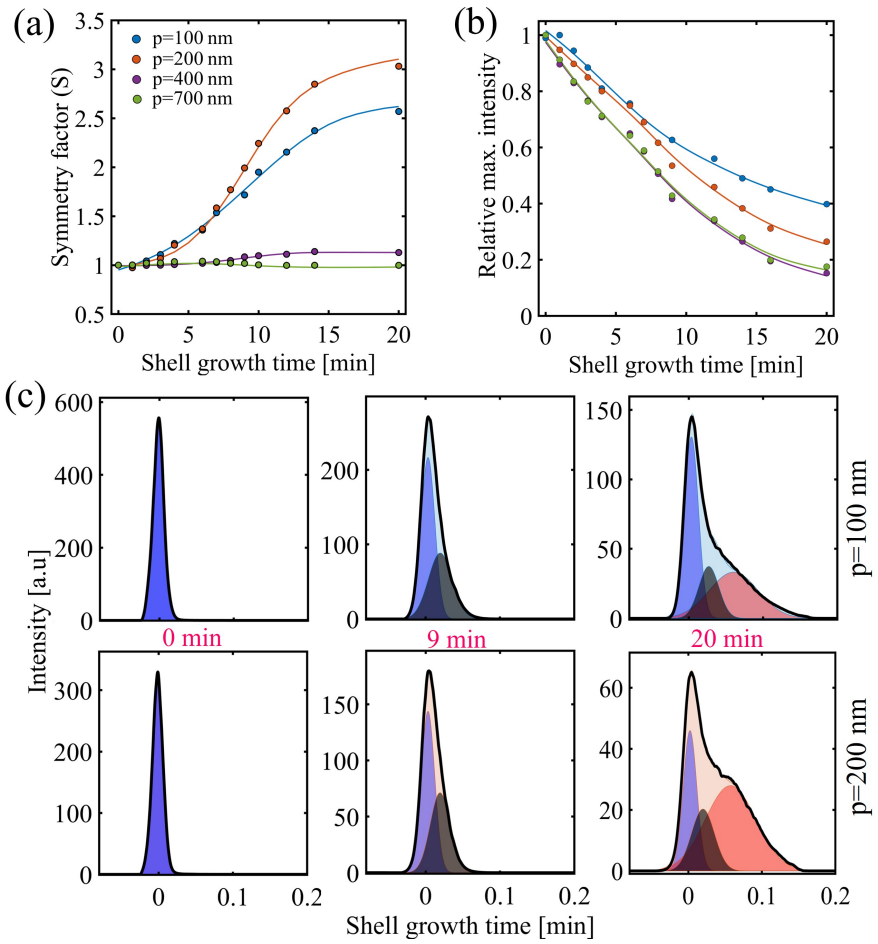

Figure 5.3: (a) The calculated symmetry factor S of the line profiles of the GaAs(111) nanowire Bragg peaks at different nanowire arrays integrated along Q in RSM as function of shell growth time. (b) The relative changes of maximum intensities of Bragg peaks of the nanowires at different arrays as function of shell growth time. (c) Exemplary plots of the multi-Gaussian fitting model used to deconvolute the integrated line profiles of the Bragg peak of the nanowires at the arrays with p = 100 nm and p = 200 nm

These values imply that the average volume of the nanowire part that exhibit

bending forms about 55% of the total volume of the nanowires at the arrays with $p = 100$ nm while 45% remains rather-straight. For the nanowire arrays with $p = 200$ nm, about 75% of the total volume of the nanowires are bent. The average length of the nanowires, $l_{average}$ at the arrays with p =100 nm to p =1000 nm are listed in table 5.1. For $p \leq 700$ nm, $l_{average}$ increases as p increases whereas for $p \geq 700$ nm, $l_{average}$ shows negligible variation. Therefore, in the present research we focus on the nanowire arrays with $p \leq 700$ nm. The length of the exposed segment of the nanowire can be calculated from equation 5.1 as listed in table 5.1 by considering the distance between the nanowires in our case along the bending direction is $\sqrt{3}\,p$.

Table 5.1: Measured average length $l_{average}$ of the nanowires at different arrays and the calculated length of the shell-material exposed segment $l_{exposed}$.

Pitch size (p) [nm]	$l_{average}$ [nm]	$l_{exposed}$ [nm]
100	850 ± 90	300
200	1035 ± 70	600
400	1120 ± 50	1120
700	1150 ± 50	1150
1000	1150 ± 50	1150

By considering $l^{p}_{average}$ of the nanowires for the mentioned arrays, the length of the bent part l^{p}_{bent} of the nanowire can be calculated by $l^{100}_{bent} = 0.55 \times l^{100}_{average} =$ 468 and $l^{200}_{bent} = 0.75 \times l^{200}_{average} = 776$ nm. The values of $l_{average}$, l_{bent} and $l_{exposed}$ are plotted in 5.4(4). From these values, one can estimate the length of the nanowire segment l^{p}_{D} that is covered by the diffused materials by $l^{100}_{D} = l^{100}_{bent} - l^{100}_{exposed} \approx 142$ nm and $l^{200}_{D} = l^{200}_{bent} - l^{200}_{exposed} \approx 124$ therefore $l^{average}_{D} \approx 135$ nm. Therefore equation 5.2 may be given by

$$l_{bent} = \frac{p}{\tan(\Phi_{flux})} + 135 \tag{5.4}$$

The length of l_D segment however depends on the diffusivity of the shell materials which in turn depends on the nanowire surface properties as well as the system temperature and the V-III ratio (*i.e.* As pressure in our case) as explained in 2.2.3. Therefore, the value of l_D is valid for the given properties

of our sample and the MBE growth condition and may be changed by tuning the mentioned parameters.

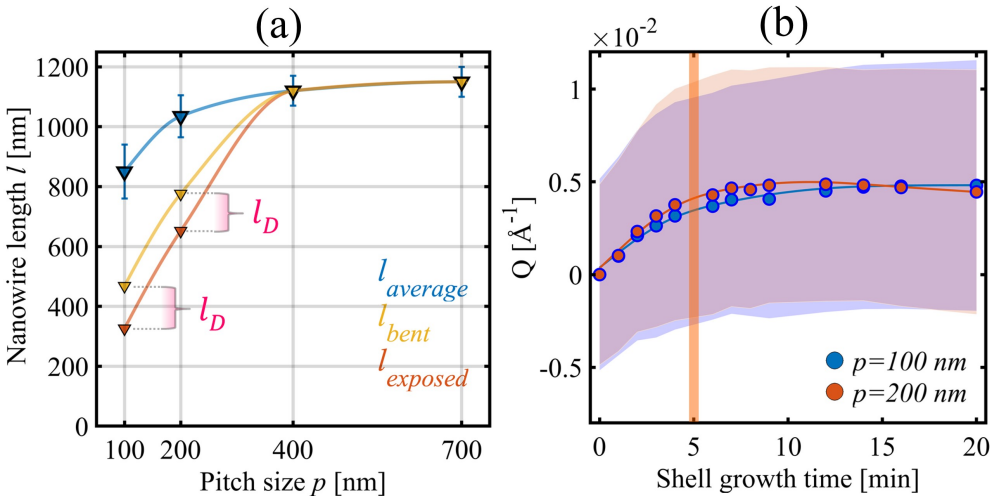

Figure 5.4: (a) The estimated length of the nanowire segments that exhibited bending extracted from the XRD peak profile and compared to the length of the exposed segment indicating the length of the nanowire segment that is covered by the diffused materials (l_D). (b) The peak position of the XRD signal of the lower part of the nanowire at the arrays with $p = 100$ nm and $p = 200$ nm as function os shell growth time.

It is worth to mention that the signal from the shadowed part of the nanowire showed minor shifting toward higher Q values as shown in figure 5.4(b) where the position of the peak maxima of XRD signal of the arrays with $p = 100$ nm and $p = 200$ nm extracted from the fitting model are plotted as function of shell growth time. It can be seen that the peak position exhibited minor changes during the first 5 minutes of shell growth time indicating small nanowire bending ($\approx 0.025°$). The angular resolution of our measurement is 0.01° limited by the XRD goniometer resolution and the normal distribution of the X-ray beam (*i.e.* the cross-sectional profile of the beam) that gives the confidence interval of defining the Bragg peak position of the unstrained nanowires in RSM. However, the minor changes of the peaks position during the first 5 minutes of the shell growth times indicate developing strain in the

entire nanowire and minor nanowire curvature at the early stages of shell growth time which is in a logic consistency with our hypothesis in 4.4.1 by considering the 2D diffusivity, i.e., the diffusion of the shell material along the nanowire axis and around the nanowire perimeter. The diffusivity of the shell material is high at the first during shell growth and may decrease as the shell thickness increase and the strain on the nanowire surface increases.

5.3 Strain distribution along the nanowire

Benefiting from spatial distribution of the XRD signal in reciprocal space of the bent nanowires, we are able to measure the average strain at different parts of the nanowires during the shell growth. By profiling the XRD signal along Q_z and Q_r at the position of Bragg peaks along Q extracted from the multiple-Gaussian fitting model shown in figure 5.3(b) for the arrays with $p =$ 100 nm and $p = 200$ nm. To extract the strain values from the nanowire lower part for the nanowire arrays with $p = 100$ nm and $p = 200$ nm and nanowire bottom for nanowire arrays with $p = 400$ nm and $p = 700$ nm we integrate a line profile along Q_z. These profiles along Q_z are taken at the Bragg peak position on $Q \approx 0\text{Å}^{-1}$ of the straight GaAs(111) nanowires at the different arrays before shell growth (blue lines in figure 5.5(a)). This position in RSM that the signal of the lowest part of the nanowire (i.e. nanowire bottom, we denote it in the text by B) is expected to take place during shell growth. Other line profile along Q_r is taken for each Bragg peak during shell growth at the center of the peak shouldering in case of the arrays with $p = 100$ nm and $p = 200$ nm and at the peak center for the arrays with $p = 400$ nm and $p = 700$ nm. At this position in RSM, the signal from the middle section (denoted by M) of the bent nanowire segment take place as indicated by black lines in figure 5.5(a). For extracting the strain values at the nanowire top part (denoted by T), we integrate a line profile along Q_r at the position of the displaced WZ peak (WZ_{top}) on Q for the signal of the nanowire arrays with $p = 400$ nm and $p = 700$ nm and at the peak tail on Q for the signals of the arrays with $p = 100$ nm and $p = 200$ nm as indicated by red lines in figure 5.5(b).

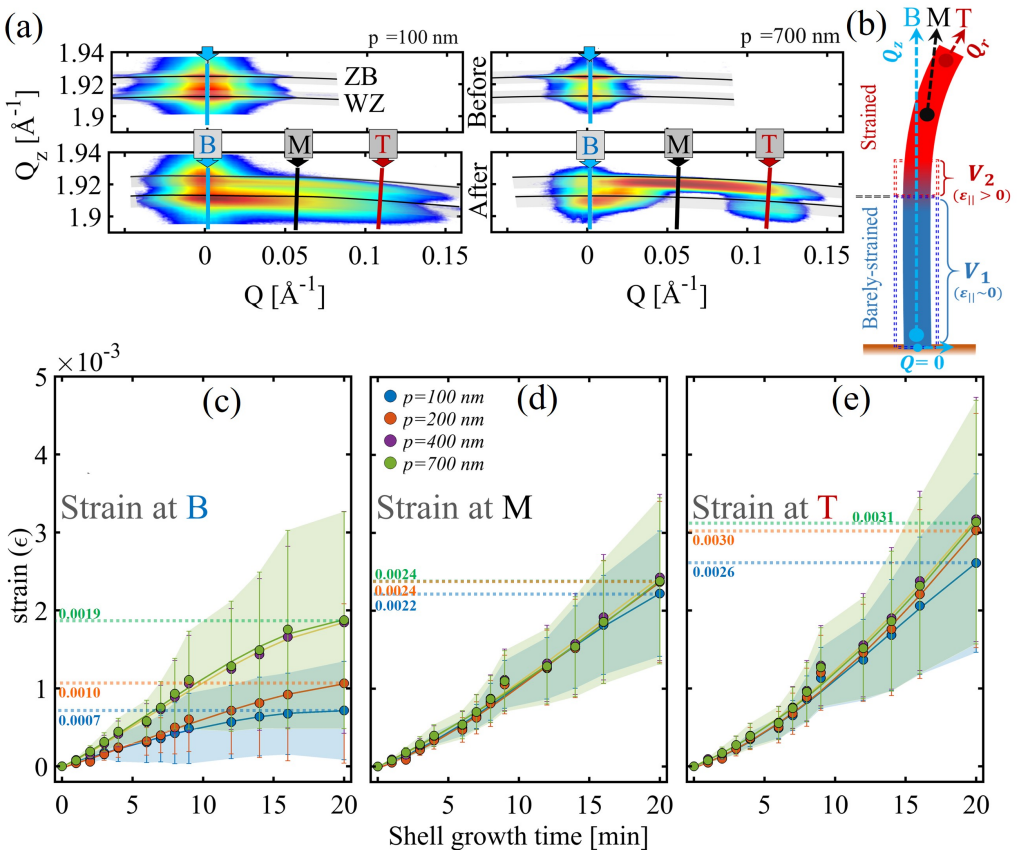

Figure 5.5: (a) 2D section of XRD peak of GaAs(111) in RSM on QQ_z of the arrays with $p = 100$ nm and $p = 700$ nm of the bare nanowires and after 20 minutes of shell growth where the B,M and T labeled arrows indicate the indicate the positions of the lines profiles along Q_r used for strain calculation. (b) The extracted average strain values and the strain variation at different positions along the nanowire plotted as function of shell growth time of the studied nanowire arrays. (c) Illustration of the strain distribution along the nanowire and the corresponding positions of B,M and T as well as the volume of the nanowire lower part and the volume of the segment that may be included in the overlapping of the XRD when integrating a line profile at B.

The obtained average strain values as well as strain variation at mentioned positions B, M and T of the nanowires are plotted for the different arrays as function of shell growth time in figures 5.5(c), (d) and (f). As it can be seen, strain values changes as the shell growth time increases in different manners

for the different parts of the nanowires at the different arrays. The different manners of strain evolution can be sorted as following

- **At the lower part B of the nanowire**, the corresponding XRD signal is close to $Q = 0$ Å^{-1} in RSM. The average strain $\epsilon_{||}^{B,p}$ in the arrays with $p = 100$ nm increases and satiate at $\epsilon_{||}^{B,100}$ =0.0007 after 16 minutes of shell growth while $\epsilon_{||}^{B,200}$ increase in a polynomial fashion and reaches a value $\epsilon_{||}^{B,200}$ =0.001 after 20 minutes of shell growth as shown in figure 5.5(c). This approach indicate the low strain magnitude at the lower parts of the nanowires where the shadowing effect take place. The fact that a slight strain built-up in shadowed part of the nanowires of these arrays is in a logical consistency with the hypothesis we presented in 4.4.1 to explain the strain and bending evolution of the single nanowire case. The entire nanowire at the early stages of shell growth is slightly strained due to the high diffusivity of the shell material on the nanowire surface where this diffusivity decreases as the strain increases. The same approach explains the satiated strain variation (shaded with blue in figure 5.5(b)) and the slight shifting of the peak position at the lower part of the nanowire as shown in figure 5.4(b). Additionally, the overlapping of the signal in RSM of the bent (strained) part of the nanowire with the lower (barely-strained) part must be considered as a contributor to the strain curve plotted in figure 5.5(b). The volume of overlapping segment of the bent part of the nanowire with the lower part is demonstrated by the red box in figure 5.5(c) and denoted by V_2. As the nanowire curvature increases, the signal spreading along Q in RSM increases therefore the overlapping decreases, i.e., the volume V_2 decreases and the ratio $\frac{V_2}{V_1}$ decreases where V_1 is the volume of the lower (barely-strained) part of the nanowire. The ratio $\frac{V_2}{V_1}$ explains the relatively higher strain values at B of the arrays with $p = 200$ nm comparing to the ones of arrays with p=100 nm, where V_1 forms 25% of the nanowire volume at the array with $p =$ 200 nm comparing to 45% for the ones with $p = 100$ nm as shown previously. For the nanowire arrays with $p = 400$ nm and $p = 700$ nm, the average strain increases in the same manner for both nanowire

arrays and reach a value of $\epsilon_{||}^{B,400} = \epsilon_{||}^{B,700} = 0.0019$ after 20 minutes of shell growth. The strain variation of these arrays (shaded with green in figure 5.5(b) for the arrays with p =700 nm) increase as the shell growth proceed implying the progressive strain evolution and the increasing asymmetry degree of shell growth around the nanowire as explained in 4.4.1.

However, it was reported in literatures that the strain magnitude at the nanowire base near the wire-substrate interface is relatively low comparing to the other parts of the nanowire [152, 153]. This feature at the nanowire base explains the curve shape of the strain function of the nanowire arrays at $p = 400$ nm and $p = 700$ nm plotted in 5.5(c) as well as the high strain variation comparing to the other positions M and T of the same nanowire arrays shaded in green in figures 5.5(d) and (f) by the same concept of overlapping signals in RSMs, respectively.

- **At the position M on the nanowire**, that is exposed to the shell material, the average strain magnitude of all nanowire arrays increases to $\epsilon_{||}^{M,200} = \epsilon_{||}^{M,400} = \epsilon_{||}^{M,700} = 0.0024$ while $\epsilon_{||}^{M,100} = 0.0022$ as the shell growth proceed as well as the strain variation.

- **At the position T that is close to the nanowire tip**, the strain at this position increases as a quadratic function to the shell growth time and reaches a higher value comparing to the strain at C where $\epsilon_{||}^{M,100}$ =0.0026, $\epsilon_{||}^{M,200} = 0.003$ and $\epsilon_{||}^{M,400} = \epsilon_{||}^{M,700} = 0.0031$. This increment fashion of strain magnitude may be explained by the changes of the local deposition geometry of the growth material along the nanowire. As the nanowire curves, The angle of the incident flux changes along the nanowire as demonstrated by [Spencer McDermott and Ryan B. Lewis, 2021] which leads to inhomogeneous shell thickness along the exposed segment of the nanowire. However, in our case, we relate to the early stages of nanowire bending and the maximum bending angle doesn't exceed 5° at the nanowire tip, therefore, the variation of the strain magnitude at B, M and T would increase as the nanowire bending increases.

5.4 Summery of chapter 5

In this work we employed the distance between the neighboring nanowires as a parameter for controlling the shell material distribution along the nanowires growth axis, thus the strain distribution and the subsequent bending profile of the nanowire. At the arrays with high nanowire densities, the shell materials are deposited asymmetrically on nanowire part that is exposed to the direct flux. The shell materials may diffuse toward the shadowed part of the nanowire and the whole mechanism results in strained and bent upper part of the nanowire while the lower part remains rather straight and barely strained.

At the nanowire arrays with high nanowire densities where the shadowing effect of the shell material take place, we could estimate the length of the nanowire segment that is strained by the diffused shell materials by means of X-ray diffraction technique. We observed that the shadowed part of the nanowire exhibit low strain magnitude and minor bending during the early stages of shell growth indicating high diffusivity of the shell materials at the beginning. At the nanowire arrays with low densities where the shadowing effect take no place, the shell materials cover the whole length of the nanowire. At these arrays the entire nanowire exhibit bending but the XRD measurement revealed that the strain magnitude is not homogeneous along the nanowire indicating the variation of the local growth geometry along the nanowire. These results provide recipes for controlling the nanowire geometry with novel designs which might be used for nanowires interconnect as well as tuning the strain distribution along the nanowire.

Chapter 6

General summery

We used a specialized and portable MBE system that could be loaded on the heavy-load goniometers of the beamlines at the synchrotron radiation facility PETRA-III at DESY. This setup allowed performing different time-resolved *in-situ* X-ray diffraction characterization of the nanowire crystal properties during the growth of the nanowire core and the shell in GaAs-$In_xGa_{1-x}As$ core-shell system.

By using a special designed Si(111) substrate coated with thermal oxide and pattered by electron beam lithography to have patterns of the nucleation sites of the nanowire growth with different inter-spacing we could realize the influence of the nanowire interspacing (i.e. nanowire density) on the crystal structure of the GaAs nanowire. In our case, we observed that the WZ crystal structure is the dominant phase in dense nanowire arrays, whereas for low density arrays ZB is the prominent crystal phase. However, the experimental results of the time-resolved *in-situ* X-ray diffraction measurements of the GaAs nanowire during the growth at different nanowire densities showed that at a certain nanowire height during growth the intensity of the XRD signal of the WZ phase increase whereas this height vary at the different nanowire densities. Our simulation showed the density dependence of the crystal structure and pinpointed the impact of the shadowing of Ga-flux on the evolution of the nanowire crystal structure.

Further, we studied the evolution of the strain and nanowire bending in

case of depositing lattice-mismatched shell material on the nanowire facets. Uniform nanowire bending could be obtained by avoiding substrate rotation during MBE growth. We used Si(111) substrates with tow different characteristics of the oxide layer on the substrate surface. On one hand, a substrate with a thick oxide layer that was grown thermally and patterned using EBL technique, and on the other hand, a substrate with thin oxide layer that grow naturally. We observed different preferable bending directions of GaAs-$In_xGa_{1-x}As$ core-shell nanowires for the different substrate types. In our MBE system, the nanowires bent away from the direction of the Ga-flux in case of using substrates covered with the thermal oxide while the bending was away from the direction of the As flux in case of using the substrates with the native oxide. This observation implies that the preferable nanowire side facets for shell growth depend not only on the arrangement of the material sources, but also on the type of the oxide covering the substrates.

Following this observation, a study of the strain evolution in the core-shell nanowires was done by means the time-resolved *in-situ* XRD measurements of the axial GaAs(111) Bragg's reflection in case of an ensemble of nanowire arrays as well as single nanowire. This study showed that the strain and nanowire bending have non-linear dependency as function of the shell growth time. The non-linear relation between the strain and nanowire bending on one hand and the shell growth time on the other hand was explained by the changes of the growth dynamics during shell deposition due to the changes of the surface properties of the nanowire. This investigation provide a deep insight into the evolution of the induced axial strain and the resulting nanowire bending.

Finally, the flux-shadowing effect of the shell material was exploited to control the axial distribution of the shell material along the nanowire growth axis thanks to the prior knowledge about the preferred growth site for the shell material on the nanowire facets. We used a patterned substrate in this case and the angle of the incident flux with respect to the nanowire growth axis and the distance between the neighboring nanowires are the parameters for controlling the shell material distribution along the nanowires growth axis. The strain distribution and the subsequent bending profile of the nanowire

varied at the different nanowire arrays with different densities. At the high density nanowire arrays, the shell materials were deposited asymmetrically on the upper part of the nanowire that was exposed to the direct flux. Furthermore, the diffusion of the shell material toward the shadowed part of the nanowire was considered. The obtained nanowires in this case have strained and bent upper parts while the lower parts are rather straight and barely strained. The time-resolved *in-situ* XRD measurement allowed us to estimate the length of the nanowire segment that is covered by the diffused shell material as well as the strain evolution at different parts of the nanowire during shell growth.

The studies and results presented in this work provide methodologies of controlling the nanowire crystal phase and the nanowire geometry with novel designs as well as the strain distribution along and across the nanowire. Having nanowires with tune-able and controllable geometry as well as strain profile can be beneficial for controlling the optical and electronic properties of these wires.

Bibliography

[1] Alexander Berg, Sadegh Yazdi, Ali Nowzari, Kristian Storm, Vishal Jain, Neimantas Vainorius, Lars Samuelson, Jakob B. Wagner, and Magnus T. Borgström. Radial Nanowire Light-Emitting Diodes in the (AlxGa1-x)yIn1-yP Material System. *Nano Letters*, 16(1):656–662, jan 2016.

[2] Qian Gao, Dhruv Saxena, Fan Wang, Lan Fu, Sudha Mokkapati, Yanan Guo, Li Li, Jennifer Wong-Leung, Philippe Caroff, Hark Hoe Tan, and Chennupati Jagadish. Selective-area epitaxy of pure wurtzite InP nanowires: High quantum efficiency and room-temperature lasing. *Nano Letters*, 14(9):5206–5211, sep 2014.

[3] Katsuhiro Tomioka, Masatoshi Yoshimura, and Takashi Fukui. A III-V nanowire channel on silicon for high-performance vertical transistors. *Nature*, 488(7410):189–192, aug 2012.

[4] Prabal Dev Bhuyan, Ashok Kumar, Yogesh Sonvane, P. N. Gajjar, Rita Magri, and Sanjeev K. Gupta. Si and Ge based metallic core/shell nanowires for nano-electronic device applications. *Scientific Reports*, 8(1):1–10, 2018.

[5] C. M. Lieber. Semiconductor nanowires: A platform for nanoscience and nanotechnology. In *2010 3rd International Nanoelectronics Conference (INEC)*, pages 5–6, Jan 2010.

[6] Jonas Johansson and Kimberly A. Dick. Recent advances in semiconductor nanowire heterostructures. *CrystEngComm*, 13:7175–7184, 2011.

[7] Peter Krogstrup, Henrik I Jørgensen, Erik Johnson, Morten Hannibal Madsen, Claus B. Sørensen, Anna Fontcuberta i Morral, Martin Aagesen, Jesper Nygård, and Frank Glas. Advances in the theory of III-V nanowire growth dynamics. *Journal of Physics D: Applied Physics*, 46(31):313001, 2013.

[8] Katsuhiro Tomioka and Takashi Fukui. Recent progress in integration of III-V nanowire transistors on si substrate by selective-area growth. *Journal of Physics D: Applied Physics*, 47(39):394001, 2014.

[9] Neil P. Dasgupta, Jianwei Sun, Chong Liu, Sarah Brittman, Sean C. Andrews, Jongwoo Lim, Hanwei Gao, Ruoxue Yan, and Peidong Yang. 25th anniversary article: Semiconductor nanowires - synthesis, characterization, and applications. *Advanced Materials*, 26(14):2137–2184, 2014.

[10] Sasa Gazibegovic, Diana Car, Hao Zhang, Stijn C. Balk, John A. Logan, Michiel W. A. de Moor, Maja C. Cassidy, Rudi Schmits, Di Xu, Guanzhong Wang, Peter Krogstrup, Roy L. M. Op het Veld, Kun Zuo, Yoram Vos, Jie Shen, DaniÃ?l Bouman, Borzoyeh Shojaei, Daniel Pennachio, Joon Sue Lee, Petrus J. van Veldhoven, Sebastian Koelling, Marcel A. Verheijen, Leo P. Kouwenhoven, Chris J. PalmstrÃ?m, and Erik P. A. M. Bakkers. Epitaxy of advanced nanowire quantum devices. *Nature*, 548:434–438, Aug 2017.

[11] Jun Tatebayashi, Satoshi Kako, Jinfa Ho, Yasutomo Ota, Satoshi Iwamoto, and Yasuhiko Arakawa. Room-temperature lasing in a single nanowire with quantum dots. *Nature Photonics*, 9(8):501–505, jul 2015.

[12] Leila Balaghi, Genziana Bussone, Raphael Grifone, René Hübner, Jörg Grenzer, Mahdi Ghorbani-Asl, Arkady V. Krasheninnikov, Harald

Schneider, Manfred Helm, and Emmanouil Dimakis. Widely tunable GaAs bandgap via strain engineering in core/shell nanowires with large lattice mismatch. *Nature Communications*, 10(1), dec 2019.

[13] Allon I. Hochbaum, Rong Fan, Rongrui He, and Peidong Yang. Controlled growth of si nanowire arrays for device integration. *Nano Letters*, 5(3):457–460, 2005.

[14] K. Tomioka, P. Mohan, J. Noborisaka, S. Hara, J. Motohisa, and T. Fukui. Growth of highly uniform inas nanowire arrays by selective-area movpe. *Journal of Crystal Growth*, 298:644 – 647, 2007.

[15] Martin Heiß, Eva Riedlberger, Dańce Spirkoska, Max Bichler, Gerhard Abstreiter, and Anna Fontcuberta i Morral. Growth mechanisms and optical properties of GaAs-based semiconductor microstructures by selective area epitaxy. *Journal of Crystal Growth*, 310(6):1049–1056, March 2008.

[16] S. Hertenberger, D. Rudolph, M. Bichler, J. J. Finley, G. Abstreiter, and G. Koblmüller. Growth kinetics in position-controlled and catalyst-free inas nanowire arrays on si(111) grown by selective area molecular beam epitaxy. *Journal of Applied Physics*, 108(11):114316, 2010.

[17] Sébastien Plissard, Kimberly A Dick, Guilhem Larrieu, Sylvie Godey, Ahmed Addad, Xavier Wallart, and Philippe Caroff. Gold-free growth of gaas nanowires on silicon: arrays and polytypism. *Nanotechnology*, 21(38):385602, 2010.

[18] Benedikt Bauer, Andreas Rudolph, Marcello Soda, Anna Fontcuberta i Morral, Josef Zweck, Dieter Schuh, and Elisabeth Reiger. Position controlled self-catalyzed growth of gaas nanowires by molecular beam epitaxy. *Nanotechnology*, 21(43):435601, 2010.

[19] Bernhard Mandl, Anil W. Dey, Julian Stangl, Mirco Cantoro, Lars-Erik Wernersson, Günther Bauer, Lars Samuelson, Knut Deppert, and Claes Thelander. Self-seeded, position-controlled inas nanowire growth

on si: A growth parameter study. *Journal of Crystal Growth*, 334(1):51 – 56, 2011.

[20] S Plissard, G Larrieu, X Wallart, and P Caroff. High yield of self-catalyzed gaas nanowire arrays grown on silicon via gallium droplet positioning. *Nanotechnology*, 22(27):275602, 2011.

[21] Sandra Gibson and Ray LaPierre. Study of radial growth in patterned self-catalyzed gaas nanowire arrays by gas source molecular beam epitaxy. *physica status solidi (RRL) - Rapid Research Letters*, 7(10):845–849, 2013.

[22] A. M. Munshi, D. L. Dheeraj, V. T. Fauske, D. C. Kim, J. Huh, J. F. Reinertsen, L. Ahtapodov, K. D. Lee, B. Heidari, A. T. J. van Helvoort, B. O. Fimland, and H. Weman. Position-controlled uniform gaas nanowires on silicon using nanoimprint lithography. *Nano Letters*, 14(2):960–966, 2014.

[23] Fabian Schuster, Martin Hetzl, Saskia Weiszer, Jose A. Garrido, María de la Mata, Cesar Magen, Jordi Arbiol, and Martin Stutzmann. Position-controlled growth of gan nanowires and nanotubes on diamond by molecular beam epitaxy. *Nano Letters*, 15(3):1773–1779, 2015.

[24] Dingding Ren, Junghwan Huh, Dasa L. Dheeraj, Helge Weman, and Bjørn-Ove Fimland. Influence of pitch on the morphology and luminescence properties of self-catalyzed gaassb nanowire arrays. *Applied Physics Letters*, 109(24):243102, 2016.

[25] Jelena Vukajlovic-Plestina, Wonjong Kim, Vladimir G. Dubrovski, Gözde Tütüncüoğlu, Maxime Lagier, Heidi Potts, Martin Friedl, and Anna Fontcuberta i Morral. Engineering the size distributions of ordered gaas nanowires on silicon. *Nano Letters*, 17(7):4101–4108, 2017.

[26] Fabrice Oehler, Andrea Cattoni, Andrea Scaccabarozzi, Gilles Patriarche, Frank Glas, and Jean-Christophe Harmand. Measuring and modeling the growth dynamics of self-catalyzed gap nanowire arrays. *Nano Letters*, 18(2):701–708, 2018.

[27] E D Leshchenko, P Kuyanov, R R LaPierre, and V G Dubrovskii. Tuning the morphology of self-assisted gap nanowires. *Nanotechnology*, 29(22):225603, 2018.

[28] Richard G. Hobbs, Nikolay Petkov, and Justin D. Holmes. Semiconductor nanowire fabrication by bottom-up and top-down paradigms. *Chemistry of Materials*, 24(11):1975–1991, 2012.

[29] Mohanchand Paladugu, Clement Merckling, Roger Loo, Olivier Richard, Hugo Bender, Johan Dekoster, Wilfried Vandervorst, Matty Caymax, and Marc Heyns. Site selective integration of III-V materials on si for nanoscale logic and photonic devices. *Crystal Growth & Design*, 12(10):4696–4702, 2012.

[30] Thomas E. Kazior. Beyond cmos: heterogeneous integration of III-V devices, rf mems and other dissimilar materials/devices with si cmos to create intelligent microsystems. *Philos Trans A Math Phys Eng Sci*, 372(2012):20130105, Mar 2014.

[31] Leila Balaghi, Tina Tauchnitz, René Hübner, Lothar Bischoff, Harald Schneider, Manfred Helm, and Emmanouil Dimakis. Droplet-confined alternate pulsed epitaxy of gaas nanowires on si substrates down to cmos-compatible temperatures. *Nano Letters*, 16(7):4032–4039, 2016.

[32] Song Jin, Dongmok Whang, Michael C. McAlpine, Robin S. Friedman, Yue Wu, and Charles M. Lieber. Scalable interconnection and integration of nanowire devices without registration. *Nano Letters*, 4(5):915–919, 2004.

[33] M Heiß, E Russo-Averchi, A Dalmau-Mallorquí, G Tütüncüoğlu, F Matteini, D Rüffer, S Conesa-Boj, O Demichel, E Alarcon-Lladó, and A Fontcuberta i Morral. III-V nanowire arrays: growth and light interaction. *Nanotechnology*, 25(1):014015, 2014.

[34] Manish Sharma, Md Rezaul Karim, Pavan Kasanaboina, Jia Li, and Shanthi Iyer. Pitch-induced bandgap tuning in self-catalyzed growth

of patterned gaassb axial and gaas/gaassb core-shell nanowires using molecular beam epitaxy. *Crystal Growth & Design*, 17(2):730–737, 2017.

[35] Carlos García Núñez, Fengyuan Liu, William Taube Navaraj, Adamos Christou, Dhayalan Shakthivel, and Ravinder Dahiya. Heterogeneous integration of contact-printed semiconductor nanowires for high-performance devices on large areas. *Microsystems & Nanoengineering*, 4(1):22, 2018.

[36] Thomas Mårtensson, Patrick Carlberg, Magnus Borgström, Lars Montelius, Werner Seifert, and Lars Samuelson. Nanowire arrays defined by nanoimprint lithography. *Nano Letters*, 4(4):699–702, 2004.

[37] V. G. Dubrovskii, T. Xu, A. Díaz Álvarez, S. R. Plissard, P. Caroff, F. Glas, and B. Grandidier. Self-equilibration of the diameter of ga-catalyzed gaas nanowires. *Nano Letters*, 15(8):5580–5584, 2015.

[38] Qian Gao, Vladimir G. Dubrovskii, Philippe Caroff, Jennifer Wong-Leung, Li Li, Yanan Guo, Lan Fu, Hark Hoe Tan, and Chennupati Jagadish. Simultaneous selective-area and vapor-liquid-solid growth of inp nanowire arrays. *Nano Letters*, 16(7):4361–4367, 2016.

[39] Martin Friedl, Kris Cerveny, Pirmin Weigele, Gozde Tütüncüoglu, Sara Martí-Sánchez, Chunyi Huang, Taras Patlatiuk, Heidi Potts, Zhiyuan Sun, Megan O. Hill, Lucas Güniat, Wonjong Kim, Mahdi Zamani, Vladimir G. Dubrovskii, Jordi Arbiol, Lincoln J. Lauhon, Dominik M. Zumbühl, and Anna Fontcuberta i Morral. Template-assisted scalable nanowire networks. *Nano Letters*, 18(4):2666–2671, 2018.

[40] Hanno Küpers, Ryan B. Lewis, Abbes Tahraoui, Mathias Matalla, Olaf Krüger, Faebian Bastiman, Henning Riechert, and Lutz Geelhaar. Diameter evolution of selective area grown ga-assisted gaas nanowires. *Nano Research*, 11(5):2885–2893, May 2018.

[41] Philipp Schroth, Julian Jakob, Ludwig Feigl, Seyed Mohammad Mostafavi Kashani, Jonas Vogel, Jörg Strempfer, Thomas F. Keller,

Ullrich Pietsch, and Tilo Baumbach. Radial growth of self-catalyzed gaas nanowires and the evolution of the liquid ga-droplet studied by time-resolved in situ x-ray diffraction. *Nano Letters*, 18(1):101–108, 2018.

[42] Magnus T. Borgstrom, George Immink, Bas Ketelaars, Rienk Algra, and Erik P. A. M. Bakkers. Synergetic nanowire growth. *Nature Nanotechnology*, 2(9):541–544, SEP 2007.

[43] Nickolay V. Sibirev, Maria Tchernycheva, Maria A. Timofeeva, Jean-Christophe Harmand, George E. Cirlin, and Vladimir G. Dubrovskii. Influence of shadow effect on the growth and shape of inas nanowires. *Journal of Applied Physics*, 111(10):104317, 2012.

[44] D. Rudolph, L. Schweickert, S. Morkötter, B. Loitsch, S. Hertenberger, J. Becker, M. Bichler, G. Abstreiter, J. J. Finley, and G. Koblmüller. Effect of interwire separation on growth kinetics and properties of site-selective gaas nanowires. *Applied Physics Letters*, 105(3):033111, 2014.

[45] A Kelrich, Y Calahorra, Y Greenberg, A Gavrilov, S Cohen, and D Ritter. Shadowing and mask opening effects during selective-area vapor-liquid-solid growth of inp nanowires by metalorganic molecular beam epitaxy. *Nanotechnology*, 24(47):475302, 2013.

[46] Sandra J Gibson and Ray R LaPierre. Model of patterned self-assisted nanowire growth. *Nanotechnology*, 25(41):415304, 2014.

[47] Tina Tauchnitz, Timur Nurmamytov, Rene Hübner, Martin Engler, Stefan Facsko, Harald Schneider, Manfred Helm, and Emmanouil Dimakis. Decoupling the two roles of ga droplets in the self-catalyzed growth of gaas nanowires on siox/si(111) substrates. *Crystal Growth & Design*, 17(10):5276–5282, 2017.

[48] Wonjong Kim, Vladimir G. Dubrovskii, Jelena Vukajlovic-Plestina, Gözde Tütüncüoğlu, Luca Francaviglia, Lucas Güniat, Heidi Potts, Martin Friedl, Jean-Baptiste Leran, and Anna Fontcuberta i Morral.

Bistability of contact angle and its role in achieving quantum-thin self-assisted gaas nanowires. *Nano Letters*, 18(1):49–57, 2018.

[49] Torsten Rieger, Mihail Ion Lepsa, Thomas Schäpers, and Detlev Grützmacher. Controlled wurtzite inclusions in self-catalyzed zinc blende III-V semiconductor nanowires. *Journal of Crystal Growth*, 378:506 – 510, 2013. The 17th International Conference on Molecular Beam Epitaxy.

[50] Daniel Jacobsson, Federico Panciera, Jerry Tersoff, Mark C. Reuter, Sebastian Lehmann, Stephan Hofmann, Kimberly A. Dick, and Frances M. Ross. Interface dynamics and crystal phase switching in GaAs nanowires. *Nature*, 531:317–322, 2016.

[51] Philipp Schroth, Julian Jakob, Ludwig Feigl, Seyed Mohammad Mostafavi Kashani, Ullrich Pietsch, and Tilo Baumbach. Lithography-free variation of the number density of self-catalyzed gaas nanowires and its impact on polytypism. *MRS Communications*, 8:871–877, 2018.

[52] Johan Grönqvist, Niels Søndergaard, Fredrik Boxberg, Thomas Guhr, Sven Åberg, and H. Q. Xu. Strain in semiconductor core-shell nanowires. *Journal of Applied Physics*, 106(5), 2009.

[53] Jonas Johansson and Kimberly A. Dick. Recent advances in semiconductor nanowire heterostructures. *CrystEngComm*, 13(24):7175–7184, dec 2011.

[54] Andreea Costas, Camelia Florica, Nicoleta Preda, Andrei Kuncser, and Ionut Enculescu. Photodetecting properties of single CuO–ZnO core–shell nanowires with p–n radial heterojunction. *Scientific Reports*, 10(1):1–12, 2020.

[55] Ryan B. Lewis, Pierre Corfdir, Hanno Küpers, Timur Flissikowski, Oliver Brandt, and Lutz Geelhaar. Nanowires Bending over Backward from Strain Partitioning in Asymmetric Core-Shell Heterostructures. *Nano Letters*, 18(4):2343–2350, apr 2018.

[56] Ya'akov Greenberg, Alexander Kelrich, Shimon Cohen, Sohini Kar-Narayan, Dan Ritter, and Yonatan Calahorra. Strain-mediated bending of InP nanowires through the growth of an asymmetric InAs shell. *Nanomaterials*, 9(9), sep 2019.

[57] Fredrik Boxberg, Niels Søndergaard, and H. Q. Xu. Photovoltaics with piezoelectric core?shell nanowires. *Nano Letters*, 10(4):1108–1112, apr 2010.

[58] R. S. Wagner and W. C. Ellis. Vapor-liquid-solid mechanism of single crystal growth. *Applied Physics Letters*, 4(5):89–90, 1964.

[59] A. Fontcuberta I Morral, C. Colombo, G. Abstreiter, J. Arbiol, and J. R. Morante. Nucleation mechanism of gallium-assisted molecular beam epitaxy growth of gallium arsenide nanowires. *Applied Physics Letters*, 92(6), 2008.

[60] Emmanouil Dimakis, Uwe Jahn, Manfred Ramsteiner, Abbes Tahraoui, Javier Grandal, Xiang Kong, Oliver Marquardt, Achim Trampert, Henning Riechert, and Lutz Geelhaar. Coaxial Multishell (In,Ga)As/GaAs Nanowires for Near-Infrared Emission on Si Substrates. *Nano Letters*, 14(5):2604–2609, 2014.

[61] Jeremy B. Wright, Sheng Liu, George T. Wang, Qiming Li, Alexander Benz, Daniel D. Koleske, Ping Lu, Huiwen Xu, Luke Lester, Ting S. Luk, Igal Brener, and Ganapathi Subramania. Multi-colour nanowire photonic crystal laser pixels. *Scientific Reports*, 3:16–19, 2013.

[62] Jianye Li, Qi Zhang, Hongying Peng, Henry O. Everitt, Luchang Qin, and Jie Liu. Diameter-controlled vapor-solid epitaxial growth and properties of aligned ZnO nanowire arrays. *Journal of Physical Chemistry C*, 113(10):3950–3954, 2009.

[63] A. Weber M. Volmer. Nucleus formation in supersaturated systems. *Z Phys Chem*, 119:277, 1926.

[64] W. S. Lau, V. Sane, K. S. Pey, and B. Cronquist. Two types of local oxide/substrate defects in very thin silicon dioxide films on silicon. *Applied Physics Letters*, 67(September 1995):2854, 1995.

[65] H. Detz, M. Kriz, D. MacFarland, S. Lancaster, T. Zederbauer, M. Capriotti, A. M. Andrews, W. Schrenk, and G. Strasser. Nucleation of Ga droplets on Si and SiOx surfaces. *Nanotechnology*, 26(31), 2015.

[66] Dao Khac An, Nguyen Xuan Chung, Pham Hong Trang, Hoang Van Vuong, Phan Viet Phong, and Phan Anh Tuan. On growth mechanisms and dynamic simulation of growth process based on the experimental results of nanowire growth by VLS method on semiconductor substrates. *Journal of Physics: Conference Series*, 187, 2009.

[67] Federico Matteini, Vladimir G. Dubrovskii, Daniel Rüffer, Gözde Tütüncüotlu, Yannik Fontana, and Anna Fontcuberta I. Morral. Tailoring the diameter and density of self-catalyzed GaAs nanowires on silicon. *Nanotechnology*, 26(10), 2015.

[68] Tina Tauchnitz, Timur Nurmamytov, René Hübner, Martin Engler, Stefan Facsko, Harald Schneider, Manfred Helm, and Emmanouil Dimakis. Decoupling the two roles of Ga droplets in the self-catalyzed growth of GaAs nanowires on SiOx/Si(111) substrates. *Crystal Growth and Design*, 17(10):5276–5282, 2017.

[69] Sébastien Plissard, Kimberly A. Dick, Guilhem Larrieu, Sylvie Godey, Ahmed Addad, Xavier Wallart, and Philippe Caroff. Gold-free growth of GaAs nanowires on silicon: Arrays and polytypism. *Nanotechnology*, 21(38), sep 2010.

[70] Benedikt Bauer, Andreas Rudolph, Marcello Soda, Anna Fontcuberta I Morral, Josef Zweck, Dieter Schuh, and Elisabeth Reiger. Position controlled self-catalyzed growth of GaAs nanowires by molecular beam epitaxy. *Nanotechnology*, 21(43), oct 2010.

[71] A. M. Munshi, D. L. Dheeraj, V. T. Fauske, D. C. Kim, J. Huh, J. F. Reinertsen, L. Ahtapodov, K. D. Lee, B. Heidari, A. T.J. Van Helvoort, B. O. Fimland, and H. Weman. Position-controlled uniform GaAs nanowires on silicon using nanoimprint lithography. *Nano Letters*, 14(2):960–966, 2014.

[72] Peter Krogstrup, Henrik I J\orgensen, Erik Johnson, Morten Hannibal Madsen, Claus B S\orensen, Anna Fontcuberta i Morral, Martin Aagesen, Jesper Nyg\aard, and Frank Glas. Advances in the theory of III–V nanowire growth dynamics. *Journal of Physics D: Applied Physics*, 46(31):313001, 2013.

[73] C.-Y. Wen, J Tersoff, M C Reuter, E A Stach, and F M Ross. Step-Flow Kinetics in Nanowire Growth. *Phys. Rev. Lett.*, 105(19):195502, nov 2010.

[74] F. Glas, G. Patriarche, and J. C. Harmand. Growth, structure and phase transitions of epitaxial nanowires of III-V semiconductors. *Journal of Physics: Conference Series*, 209, 2010.

[75] Torsten Rieger, Mihail Ion Lepsa, Thomas Schapers, and Detlev Grützmacher. Controlled wurtzite inclusions in self-catalyzed zinc blende III-V semiconductor nanowires. *Journal of Crystal Growth*, 378:506–510, 2013.

[76] C Colombo, D Spirkoska, M Frimmer, G Abstreiter, and A i Morral. Ga-assisted catalyst-free growth mechanism of GaAs nanowires by molecular beam epitaxy. *Phys. Rev. B*, 77(15):155326, apr 2008.

[77] Volker Pankoke, Sung Sakong, and Peter Kratzer. Role of sidewall diffusion in GaAs nanowire growth: A first-principles study. *Physical Review B - Condensed Matter and Materials Physics*, 86(8):1–7, 2012.

[78] J. C. Harmand, G. Patriarche, N. Ṕŕ-Laperne, M. N. Ḿrat-Combes, L. Travers, and F. Glas. Analysis of vapor-liquid-solid mechanism in Au-assisted GaAs nanowire growth. *Applied Physics Letters*, 87(20):1–3, 2005.

[79] Mohammed Reda Ramdani, Jean Christophe Harmand, Frank Glas, Gilles Patriarche, and Laurent Travers. Arsenic Pathways in Self-Catalyzed Growth of GaAs Nanowires. *Crystal Growth & Design*, 13(1):91–96, January 2013.

[80] Martin C. Plante and Ray R. Lapierre. Analytical description of the metal-assisted growth of III-V nanowires: Axial and radial growths. *Journal of Applied Physics*, 105(11), 2009.

[81] Vladimir G. Dubrovskii. *Nucleation Theory and Growth of Nanostructures*. NanoScience and Technology. Springer Berlin Heidelberg, Berlin, Heidelberg, 2014.

[82] K. Oura, M. Katayama, A. V. Zotov, V. G. Lifshits, and A. A. Saranin. Growth of Thin Films. pages 357–387, 2003.

[83] Jacques G. Amar, Fereydoon Family, and Mihail N. Popescu. Kinetics of submonolayer epitaxial growth. *Computer Physics Communications*, 146(1):1–8, 2002.

[84] Tomoya Shitara and Tatau Nishinaga. Surface diffusion length of gallium during mbe growth on the various misoriented gaas(001) substrates. *Japanese Journal of Applied Physics*, 28(7 R):1212–1216, 1989.

[85] H. Brune. Microscopic view of epitaxial metal growth: nucleation and aggregation. *Surface Science Reports*, 31(4-6):125–229, 1998.

[86] J. ANKETELL and R. C. M. LEARNER. Fragmentation of Shell Cases Author (s): N . F . Mott Source : Proceedings of the Royal Society of London . Series A , Mathematical and Published by : Royal Society Stable URL : https://www.jstor.org/stable/97828. *Proc. Roy. Soc. A.*, 301(1413):355–361, 1967.

[87] I. N. Stranski and L. Krastanow. Zur Theorie der orientierten Ausscheidung von Ionenkristallen aufeinander. *Monatshefte für Chemie*, 71(1):351–364, 1937.

[88] Shinsuke Hara, Katsumi Irokawa, Hirofumi Miki, Akira Kawazu, Hitoshi Torii, and Hiroki I. Fujishiro. Behavior of Ga atoms on Si(001) surface at high temperature. *Journal of Applied Physics*, 98(8), 2005.

[89] Christopher F. Schuck, Simon K. Roy, Trent Garrett, Qing Yuan, Ying Wang, Carlos I. Cabrera, Kevin A. Grossklaus, Thomas E. Vandervelde, Baolai Liang, and Paul J. Simmonds. Anomalous Stranski-Krastanov growth of (111)-oriented quantum dots with tunable wetting layer thickness. *Scientific Reports*, 9(1):1–10, 2019.

[90] Y. Ebiko, S. Muto, D. Suzuki, S. Itoh, K. Shiramine, T. Haga, Y. Nakata, and N. Yokoyama. Island size scaling in InAs/GaAs self-assembled quantum dots. *Physical Review Letters*, 80(12):2650–2653, 1998.

[91] S. Guha, A. Madhukar, and K. C. Rajkumar. Onset of incoherency and defect introduction in the initial stages of molecular beam epitaxical growth of highly strained InxGa 1-xAs on GaAs(100). *Applied Physics Letters*, 57(20):2110–2112, 1990.

[92] Y. Nakata, K. Mukai, M. Sugawara, K. Ohtsubo, H. Ishikawa, and N. Yokoyama. Molecular beam epitaxial growth of InAs self-assembled quantum dots with light-emission at 1.3 μm. *Journal of Crystal Growth*, 208(1):93–99, 2000.

[93] David van Treeck, Sergio Fernández-Garrido, and Lutz Geelhaar. Influence of the source arrangement on shell growth around GaN nanowires in molecular beam epitaxy. jul 2019.

[94] Chin Yu Yeh, Z. W. Lu, S. Froyen, and Alex Zunger. Zinc-blendewurtzite polytypism in semiconductors. *Physical Review B*, 46(16):10086–10097, 1992.

[95] M. I. McMahon and R. J. Nelmes. Observation of a wurtzite form of gallium arsenide. *Physical Review Letters*, 95(21):18–21, 2005.

[96] Thomas Mårtensson, Patrick Carlberg, Magnus Borgström, Lars Montelius, Werner Seifert, and Lars Samuelson. Nanowire arrays defined by nanoimprint lithography. *Nano Letters*, 4(4):699–702, 2004.

[97] Claes Thelander, Philippe Caroff, Sébastien Plissard, Anil W. Dey, and Kimberly A. Dick. Effects of crystal phase mixing on the electrical properties of InAs nanowires. *Nano Letters*, 11(6):2424–2429, 2011.

[98] M. D. Stiles and D. R. Hamann. Ballistic electron transmission through interfaces. *Physical Review B*, 38(3):2021–2037, 1988.

[99] M. D. Stiles and D. R. Hamann. Electron transmission through silicon stacking faults. *Physical Review B*, 41(8):5280–5282, 1990.

[100] Toru Akiyama, Kosuke Sano, Kohji Nakamura, and Tomonori Ito. An empirical potential approach to wurtzite-zinc-blende polytypism in group III-V semiconductor nanowires. *Japanese Journal of Applied Physics, Part 2: Letters*, 45(8-11):4–8, 2006.

[101] V G Dubrovskii, N V Sibirev, J C Harmand, and F Glas. Growth kinetics and crystal structure of semiconductor nanowires. *Phys. Rev. B*, 78(23):235301, dec 2008.

[102] Peter Krogstrup, Stefano Curiotto, Erik Johnson, Martin Aagesen, Jesper Nyg\aard, and Dominique Chatain. Impact of the Liquid Phase Shape on the Structure of III-V Nanowires. *Phys. Rev. Lett.*, 106(12):125505, mar 2011.

[103] Frank Glas, Jean Christophe Harmand, and Gilles Patriarche. Why does wurtzite form in nanowires of III-V zinc blende semiconductors? *Physical Review Letters*, 99(14):3–6, 2007.

[104] A. D. Gamalski, C. Ducati, and S. Hofmann. Cyclic supersaturation and triple phase boundary dynamics in germanium nanowire growth. *Journal of Physical Chemistry C*, 115(11):4413–4417, 2011.

[105] Yaron Kauffmann Wayne D. Kaplan Weidong Luo Manfred Rühle Christina Scheu Sang Ho Oh, Matthew F. Chisholm. Oscillatory Mass Transport in Vapor-Liquid-Solid Growth of Sapphire Nanowires. *Science*, 330(October):489–494, 2010.

[106] Marcus Tornberg, Carina B. Maliakkal, Daniel Jacobsson, Kimberly A. Dick, and Jonas Johansson. Limits of III-V nanowire growth based on particle dynamics. *arXiv*, 2019.

[107] Daniel Jacobsson, Federico Panciera, Jerry Tersoff, Mark C. Reuter, Sebastian Lehmann, Stephan Hofmann, Kimberly A. Dick, and Frances M. Ross. Interface dynamics and crystal phase switching in GaAs nanowires. *Nature*, 531(7594):317–322, mar 2016.

[108] Federico Panciera, Zhaslan Baraissov, Gilles Patriarche, Vladimir G. Dubrovskii, Frank Glas, Laurent Travers, Utkur Mirsaidov, and Jean Christophe Harmand. Phase Selection in Self-catalyzed GaAs Nanowires. *Nano Letters*, 20(3):1669–1675, 2020.

[109] J H Van Der Merwe. Crystal Interfaces. Part II. Finite Overgrowths. *Journal of Applied Physics*, 34(1):123–127, 1963.

[110] W A Jesser and D Kuhlmann-Wilsdorf. On the Theory of Interfacial Energy and Elastic Strain of Epitaxial Overgrowths in Parallel Alignment on Single Crystal Substrates. *physica status solidi (b)*, 19(1):95–105, 1967.

[111] Martin Hetzl, Max Kraut, Julia Winnerl, Luca Francaviglia, Markus Döblinger, Sonja Matich, Anna FontcubertaMorral, and Martin Stutzmann. Strain-Induced Band Gap Engineering in Selectively Grown GaN-(Al,Ga)N Core-Shell Nanowire Heterostructures. *Nano Letters*, 16(11):7098–7106, 2016.

[112] Julian Treu, Michael Bormann, Hannes Schmeiduch, Markus Döblinger, Stefanie Morkötter, Sonja Matich, Peter Wiecha, Kai Saller, Benedikt Mayer, Max Bichler, Markus Christian Amann, Jonathan J.

Finley, Gerhard Abstreiter, and Gregor Koblmüller. Enhanced luminescence properties of InAs-InAsP core-shell nanowires. *Nano Letters*, 13(12):6070–6077, 2013.

[113] Jianxiong Zhao, Bing Chen, and Feng Wang. Shedding Light on the Role of Misfit Strain in Controlling Core–Shell Nanocrystals. *Advanced Materials*, 32(46):1–20, 2020.

[114] P. Scardi, A. Leonardi, L. Gelisio, M. R. Suchomel, B. T. Sneed, M. K. Sheehan, and C. K. Tsung. Anisotropic atom displacement in Pd nanocubes resolved by molecular dynamics simulations supported by x-ray diffraction imaging. *Physical Review B - Condensed Matter and Materials Physics*, 91(15):1–8, 2015.

[115] Mechanical properties, elastic constants, lattice vibrations.

[116] Ivan V Markov. *Crystal Growth for Beginners*. WORLD SCIENTIFIC, 2nd edition, 2003.

[117] C. Ratsch and A. Zangwill. Step-flow growth on strained surfaces. *Applied Physics Letters*, 63(17):2348–2350, 1993.

[118] M. Schroeder and D. E. Wolf. Diffusion on strained surfaces. *Surface Science*, 375(1):129–140, 1997.

[119] U. Pietsch T. Baumbach V Holy. *High-Resolution X-Ray Scattering*. Springer, 2004.

[120] W H Bragg and W L Bragg. The reflection of X-rays by crystals. *Royal Society*, 88(605):428–438, 1913.

[121] Ali Al Hassan. X-ray structural characterization of individual as-grown GaAs /(In , Ga) As /(GaAs) based core-multi-shell nanowires. 2020.

[122] Arman Davtyan. Distribution of the phase domains in semiconductor nanowires. (January), 2018.

[123] Andreas Biermanns. X-ray diffraction from single GaAs nanowires. 2012.

[124] T. Slobodskyy, P. Schroth, D. Grigoriev, A. A. Minkevich, D. Z. Hu, D. M. Schaadt, and T. Baumbach. A portable molecular beam epitaxy system for in situ x-ray investigations at synchrotron beamlines. 83(10), oct 2012.

[125] Julian Jakob. Quantitative analysis of time-resolved RHEED during growth of vertical nanowires. *Nanoscale*, 12(9):5471–5482, 2020.

[126] Hanno Kuepers, Abbes Tahraoui, Ryan B. Lewis, Sander Rauwerdink, Mathias Matalla, Olaf Krueger, Faebian Bastiman, Henning Riechert, and Lutz Geelhaar. Surface preparation and patterning by nano imprint lithography for the selective area growth of GaAs nanowires on Si(111). *Semiconductor Science And Technology*, 32(11), NOV 2017.

[127] Hanno Küpers, Ryan B. Lewis, Abbes Tahraoui, Mathias Matalla, Olaf Krüger, Faebian Bastiman, Henning Riechert, and Lutz Geelhaar. Diameter evolution of selective area grown Ga-assisted GaAs nanowires. aug 2017.

[128] Ali Al Hassan, R. B. Lewis, H. Küpers, W. H. Lin, D. Bahrami, T. Krause, D. Salomon, A. Tahraoui, M. Hanke, L. Geelhaar, and U. Pietsch. Determination of indium content of GaAs/(In,Ga)As/(GaAs) core-shell(-shell) nanowires by x-ray diffraction and nano x-ray fluorescence. *Physical Review Materials*, 2(1), jan 2018.

[129] J. Strempfer, S. Francoual, D. Reuther, D. K. Shukla, A. Skaugen, H. Schulte-Schrepping, T. Kracht, and H. Franz. Resonant scattering and diffraction beamline P09 at PETRA III. *Journal of Synchrotron Radiation*, 20(4):541–549, Jul 2013.

[130] Peter Krogstrup, Morten Hannibal Madsen, Wen Hu, Miwa Kozu, Yuka Nakata, Jesper Nygård, Masamitu Takahasi, and Robert Fei-

denhans'l. In-situ x-ray characterization of wurtzite formation in gaas nanowires. *Applied Physics Letters*, 100(9), 2012.

[131] Andreas Biermanns, Emmanouil Dimakis, Anton Davydok, Takuo Sasaki, Lutz Geelhaar, Masamitu Takahasi, and Ullrich Pietsch. Role of liquid indium in the structural purity of wurtzite inas nanowires that grow on si(111). *Nano Letters*, 14(12):6878–6883, 2014.

[132] Philipp Schroth, Martin Köhl, Jean-Wolfgang Hornung, Emmanouil Dimakis, Claudio Somaschini, Lutz Geelhaar, Andreas Biermanns, Sondes Bauer, Sergey Lazarev, Ullrich Pietsch, and Tilo Baumbach. Evolution of polytypism in gaas nanowires during growth revealed by time-resolved *in situ* x-ray diffraction. *Phys. Rev. Lett.*, 114:055504, Feb 2015.

[133] Masamitu Takahasi, Miwa Kozu, Takuo Sasaki, and Wen Hu. Mechanisms determining the structure of gold-catalyzed gaas nanowires studied by in situ x-ray diffraction. *Crystal Growth & Design*, 15(10):4979–4985, 2015.

[134] Masamitu Takahasi. In situ synchrotron x-ray diffraction study on epitaxial-growth dynamics of III-V semiconductors. *Japanese Journal of Applied Physics*, 57(5):050101, 2018.

[135] Martin Köhl, Philipp Schroth, Andrey A. Minkevich, Jean-Wolfgang Hornung, Emmanouil Dimakis, Claudio Somaschini, Lutz Geelhaar, Timo Aschenbrenner, Sergey Lazarev, Daniil Grigoriev, Ullrich Pietsch, and Tilo Baumbach. Polytypism in GaAs nanowires: determination of the interplanar spacing of wurtzite GaAs by X-ray diffraction. *Journal of Synchrotron Radiation*, 22(1):67–75, Jan 2015.

[136] Daniel Jacobsson, Fangfang Yang, Karla Hillerich, Filip Lenrick, Sebastian Lehmann, Dominik Kriegner, Julian Stangl, L. Reine Wallenberg, Kimberly A. Dick, and Jonas Johansson. Phase transformation in radially merged wurtzite gaas nanowires. *Crystal Growth & Design*, 15(10):4795–4803, 2015.

[137] Martin Köhl, Philipp Schroth, and Tilo Baumbach. Perspectives and limitations of symmetric X-ray Bragg reflections for inspecting polytypism in nanowires. *Journal of Synchrotron Radiation*, 23(2):487–500, Mar 2016.

[138] Jonas Johansson, Jessica Bolinsson, Martin Ek, Philippe Caroff, and Kimberly A. Dick. Combinatorial Approaches to Understanding Polytypism in III-V Nanowires. *ACS NANO*, 6(7):6142–6149, JUL 2012.

[139] Andreas Biermanns, Steffen Breuer, Anton Davydok, Lutz Geelhaar, and Ullrich Pietsch. Structural evolution of self-assisted gaas nanowires grown on si(111). *physica status solidi (RRL) - Rapid Research Letters*, 5(4):156–158, 2011.

[140] Young Heon Kim, Dong Woo Park, and Sang Jun Lee. Gallium-droplet behaviors of self-catalyzed gaas nanowires: A transmission electron microscopy study. *Applied Physics Letters*, 100(3):033117, 2012.

[141] J. Tersoff. Stable self-catalyzed growth of III-V nanowires. *Nano Letters*, 15(10):6609–6613, 2015.

[142] Ryan B. Lewis, Pierre Corfdir, Hanno Küpers, Timur Flissikowski, Oliver Brandt, and Lutz Geelhaar. Nanowires bending over backward from strain partitioning in asymmetric core-shell heterostructures. *Nano Letters*, 18(4):2343–2350, 2018.

[143] J. Strempfer, S. Francoual, D. Reuther, D. K. Shukla, A. Skaugen, H. Schulte-Schrepping, T. Kracht, and H. Franz. Resonant scattering and diffraction beamline P09 at PETRA III. *Journal of Synchrotron Radiation*, 20(4):541–549, 2013.

[144] Deutsches Elektronen-Synchrotron DESY. In situ and Nano X-ray diffraction beamline.

[145] Hadas Shtrikman, Ronit Popovitz-Biro, Andrey Kretinin, Lothar Houben, Moty Heiblum, Matgorzata Bukała, Marta Galicka, Ryszard

Buczko, and Perta Kacman. Method for suppression of stacking faults in wurtzite III-V nanowires. *Nano Letters*, 9(4):1506–1510, 2009.

[146] Tomoki Yamashita, Toru Akiyama, Kohji Nakamura, and Tomonori Ito. Effects of facet orientation on relative stability between zinc blende and wurtzite structures in group III-V nanowires. *Japanese Journal of Applied Physics*, 49(5 PART 1):0550031–0550035, 2010.

[147] Philipp Schroth, Julian Jakob, Ludwig Feigl, Seyed Mohammad Mostafavi Kashani, Ullrich Pietsch, and Tilo Baumbach. Lithography-free variation of the number density of self-catalyzed GaAs nanowires and its impact on polytypism. *MRS Communications*, 8(3):871–877, sep 2018.

[148] A R Denton and N W Ashcroft. Vegard's law. Technical Report 6, 1991.

[149] S. Hertenberger, D. Rudolph, M. Bichler, J. J. Finley, G. Abstreiter, and G. Koblmüller. Growth kinetics in position-controlled and catalyst-free InAs nanowire arrays on Si(111) grown by selective area molecular beam epitaxy. *Journal of Applied Physics*, 108(11), 2010.

[150] Nickolay V. Sibirev, Maria Tchernycheva, Maria A. Timofeeva, Jean Christophe Harmand, George E. Cirlin, and Vladimir G. Dubrovskii. Influence of shadow effect on the growth and shape of InAs nanowires. *Journal of Applied Physics*, 111(10), 2012.

[151] Fabrice Oehler, Andrea Cattoni, Andrea Scaccabarozzi, Gilles Patriarche, Frank Glas, and Jean Christophe Harmand. Measuring and Modeling the Growth Dynamics of Self-Catalyzed GaP Nanowire Arrays. *Nano Letters*, 18(2):701–708, 2018.

[152] Johan Grönqvist, Niels Søndergaard, Fredrik Boxberg, Thomas Guhr, Sven Åberg, and H. Q. Xu. Strain in semiconductor core-shell nanowires. *Journal of Applied Physics*, 106(5):053508, 2009.

[153] Arman Davtyan, Dominik Kriegner, Václav Holý, Ali AlHassan, Ryan B. Lewis, Spencer McDermott, Lutz Geelhaar, Danial Bahrami, Taseer Anjum, Zhe Ren, Carsten Richter, Dmitri Novikov, Julian Müller, Benjamin Butz, and Ullrich Pietsch. X-ray diffraction reveals the amount of strain and homogeneity of extremely bent single nanowires. *Journal of Applied Crystallography*, 53(111):1310–1320, 2020.

Acknowledgments

First of all I would like to thank my supervisor Prof. Dr. Ullrich Pietsch, thank you so much for all the support during my master and PhD works. I am grateful for the opportunity to be a member of solid-state-physics group since 2015, all these years taught me, educated me and gave me a nice experiences for the life.

Most of my experimental work was held at the UHV lab at the institute of photon science at KIT-Karlsruhe, as well as the the last 10 months of my PhD work I was honored to be a member of the group of Prof. Dr. Tilo Baumbach. I would like to express my gratitude and say thank you for all this support. I am thankful for the nice team work with the former group members from whom I learned a lot, Dr. Philipp Schroth, Dr. Ludwig Feigl and Dr. Julian Jakob, as well as team I am working with currently, Dr. Svetoslav Stankov, Dr. Jochen Kalt, Dr. Bärbel Krause and Annette Weißhardt.

I would like to thank our collaborators, Dr. Lutz Geehaar, Dr. Hanno Küpers and Dr. Jesús Herranz from Paul-Drude-Institute for the supply of the nicely designed substrates and the valuable scientific feedback and discussions. To the beamline scientists Dr. Sonia Francoual, Dr Dmitri V. Novikov and Dr. Azat Khadiev and all the staff at the beamlines P09 and P23 at PETRA-III for the joint experiments and the nice support during our XRD measurements.

All the SEM images presented in this work were taken by the microscopes at Nanolab (DESY) and the Institute of Nanotechnology (KIT) and therefore I would like to thank Dr. Thomas F. Keller and his team and Simone Dehm for their help.

To my colleagues and friends (I will replace the "Dr." titles here by a "*" to reduce the formality), Amir Tosson*, ALi Alhassan*, Danial Bahrami*, Ali Abboud*, Mohammad Shokor* and Arman Davtyan*. Thank you for the nice times during the whole journey sine my master study till this moment, I am glad to know you all. And to all the friends at the solid state physics group Tasser Anjum*, Nazanin Mosahebfard, Hyeokmin Choe*,

Zahra Molla*, Mona Erfani and Julie Gai* from the chemistry department. Thank you all for being part of this journey.
To our beloved secretary, Kerstin Semma, thank you for all the help with the paper work and for being always patient while dealing with the last-moment documents. To Lisa Randolph* for coffee breaks and the interesting discussions/talks and chatting breaks during the pandemic times. Thank you for these nice breaks that were mentally needed during the harsh times of the PhD study, I am so glad to know you. To my lovely and deeply missed mother and father "Saada and Omar" for all the effort you did to raise a big family and the endless care and love that has been charging me with all energy I needed. Since the very first moment I entered the school till this moment, even after your loss this energy keeps me moving. There are no words can express how I am thankful for everything you did and how I miss you.
To my oldest brother, Mouhammad* for all the helps during the school time and the support to start my master study in Germany, I am thankful for all.
To my brothers and sisters, Ahmad, Kawthar, Hind, Raafat, Abdulmajeed and Khaleel for the amazing childhood times and for your unconditional love and support in every stage of my life.
To my bigger family and all the friends who made my life beyond the study more joyful, to my friends, Darya Mozhayeva*, Mehdi Tazi, Mohammad Elwan, Anna Lange, Ahmad and Ekaterina Mohyeldin, Abdulmaseeh Rofael, Yosab Wagdy, Jessica Chadha, Savneet Saini, Daniya Kiraeva, Alena Matytsina, Lyudmila Lyubchenko, Pirina Beleva, Mohammad Swailam. Thank you for the nice events, travels parties, going out on weekends and for all the good times we spent together, it was, still and will always be a pleasure to know you all.
To all neighbours and friends in my old dorms of 'Bürbach-SWH' and 'Glückaufstr' for all the nice companies and the cool experience.
To my childhood friends, to my teachers (Nabih Ali, Essam Hakki, Mahmoud Humaish...) I am grateful for all the experiences I gained with you.